Stac regulation of L-type Calcium Ion Channels

By

Jacqueline Niu

A dissertation submitted to the Johns Hopkins University
in conformity with the requirements for the degree of
Doctor of Philosophy

Baltimore, Maryland
March, 2018

<u>Thesis Committee</u>
Dr. Takanari Inoue
Dr. Gordon Tomaselli
Dr. Lawrence Schramm
Dr. Manu Ben-Johny
Dr. David T. Yue

ABSTRACT

High voltage-gated calcium (Ca^{2+}) channels (Ca$_V$1 and Ca$_V$2) are essential for many physiological processes including muscle contraction, neurotransmission, and gene transcription. Despite divergent functions, these channel families share a conserved carboxy-tail (CI) element that has been shown to bind calmodulin (CaM) to afford dynamic Ca^{2+} feedback of cellular excitability in neurons and cardiac myocytes. Unfortunately, global inhibition of CaM indiscriminately alters numerous processes provoking unintended consequences. Furthermore, Ca^{2+}-misregulation of channels underlies numerous maladies including cardiac arrhythmias, neurological and neuropsychiatric disorders, and skeletal myotonia. Thus, identifying pathways that individually adjust the gain of Ca^{2+}-feedback is critical. Here, we demonstrate that a recently identified partner of Ca$_V$ channels, SH3 and cysteine rich domain (stac), increases channel trafficking and channel gating independently from CaM. Moreover, stac exhibits remarkable selectivity in suppressing CaM regulation of Ca$_V$1 despite being presented with structurally similar targets. In all, these findings furnish insights into orthogonal control of Ca$_V$ channels as well as pathophysiology of Ca^{2+} signaling networks.

Though the fig tree does not bud
    and there are no grapes on the vines,
though the olive crop fails
    and the fields produce no food,
though there are no sheep in the pen
    and no cattle in the stalls,
yet I will rejoice in the Lord,
    I will be joyful in God my Savior.
The Sovereign Lord is my strength;
    he makes my feet like the feet of a deer,
    he enables me to tread on the heights.

Habakkuk 3:17-19

ACKNOWLEDGEMENTS

First, I would like to thank my thesis committee. Without their support, I would not be where I am today:

Dr. Takanari Inoue, my PhD adviser, who bravely adopted me as his student and a member of his lab even though what I study has very little to do with his field of expertise. I am very thankful for all of the scientific and professional advice I received as well as the kindness he showed me during some of the darkest times of my graduate schooling.

Dr. Manu Ben-Johny, who I consider my unofficial PhD co-adviser as well as my big brother and my friend. He taught me almost all of the techniques I know and always challenges me to think more quantitatively and critically. I am very thankful for all of the patience and care he showed me especially when I was visibly frustrated.

Dr. Gordon Tomaselli, who always helped us gather resources, whether it was monetary, scientific expertise, or materials such as clinical samples. I am also very thankful for all of the time he sacrificed out of his busy schedule to attend journal clubs, meetings, and even social events; his company is truly invaluable.

Dr. Larry Schramm, who is always cheering me on and telling me my work is great. I am very thankful for the time he provided to attend my committee meetings as well as the emotional support he provided and his advocacy for me to graduate.

Dr. David T. Yue, my late PI who always challenged me to love and honor science more. He was the first person to catch and prevent me from getting away with my intellectual laziness and told me to “woman up”. He showed me what it means to pursue being 100% Christian and 100% scientist. It was the first time I believed my worlds could achieve harmony as one.

Second, I would like to thank all the lab friends I have made. Without their expertise as well as emotional support, my work would not be possible:

Dr. Ivy E. Dick, the big sister who always goes out of her way to not only make sure good science is done but also the people behind the science are well. I really admire her love for the people around her and am very grateful her generous support as well as the support she continues to provide.

Wanjun Yang, who faithfully takes care of all the details in the lab and also always worries about my health emotionally and physically. I am really thankful for her assistance as well as her tutelage in Chinese. She always encourages me to worry less and smile more, and her cheerful company brought much joy to the mundaneness in lab every day.

Manning Zhang, a good friend who taught me how to enjoy good food after a hard day in lab. She also taught me Chinese poetry and let me force her into watching bad Chinese dramas and fangirling over different celebrities. We spent a happy year as roommates ruminating on the purpose of our existences as well as telling bad jokes.

Other friends from CSL: Dr. Lingjie Sang, a good friend and older sister who always looks out for me and helps me with my homework and programs. Dr. John Issa, a good friend and older brother who is always a good sport, whether it is telling jokes or giving advice about careers in science. Billy (Po Wei) Kang, a good friend and school partner who I can always count on to check my math. Dr. Shin Rong Lee, a good friend and older brother who is always willing to play fight with me. Boombim (Worawan) Limpitikul, a good friend who always responds very quickly to requests. Dr. Paul J. Adams, a good friend who also shares a love for music, science, and the Lord. Dr. Philemon S. Yang, who is also a church friend but is someone I really respect for his direct yet social personality. Jennifer Babitch, Ho Namkyung, Jane (Jiangyu) Li, who I only knew briefly in lab but with whom I always enjoyed speaking. Also, Dr. Nancy Yue, an honorary member of the lab who always hosted and treated us to meals and celebrated with us.

Friends from other labs: Shiva Razavi, a good friend who I met during recruitment. She welcomed me into her home and treated me to crepes. It is one of my fondest memories at Hopkins. Hideki Nakamura, who always makes time to help me with different microscopy equipment in the Inoue lab and CCD. Robert Derose, Allen Kim, Helen Wu, and Allister Suarez from the Inoue lab, who attended my lab meetings and asked thought provoking questions. Travis Babola, Debborah (Debbie) DeSilvestre and Rebecca Jones, who taught me immunohistochemistry and how to take nice pictures on the microscope. Amanda Edwards, Okhee Jeon, and Jennica Bouquet, who were also my roommates and shared many memories in Apt. 501. My cohort, Kunal Parikh, Jason Lee, Randall Meyer, Steven Tilley, Will Matern, Zinnia Xu, Alyssa Kosmides, Danny Jeck, Griffin Milsap, Mike Batista, Peter Boutros, Thomas Karathanos, Mohit Matthew, Jianan Zhan, Andy Long. I am truly proud to be part of this cohort – not only intelligent but also a very fun gang.

Other science friends: Janaka, Michelle, Kimberly, Maria. Mora, who encouraged me a lot to push for the finish line.

Third, I would like to thank my church family here in Baltimore. They taught me what community is and why it is important. Without them, I would not have finished graduate school:

Alice Huang, who persistently challenges my world views and perception of Christ in my life in a loving and patient manner. Elisa No, who reminds me it is better to be around people than to be by myself by making me go to places with her to do random things. Andrea Kim, my current roommate who is willing to listen to me talk science and nonsense at the same time. Christina Lim, Lindsay Kwong, Kristi Dusek, who are good friends that always listen to my thoughts sincerely.

Mike and Vicki McQuitty, who always encourage me and gave me a lot of confidence and motivation for the last push to finish.

Other GLC members: Ann and PR, Sunny and Robert Kim, Katerina and Scott Tomaszewski, Ann and Seong Kim, Jenny Yang, Andrew Kim, Jason Zhao, Joe Vargas, Aaron and Rachel Chang, Christine Yuri Choi, Joe Choi, Christian, David, Jami Cheng and Sam Trumbo, Stephen.

Some Stepping Stone folks: Lani, Aria, Jenny, Annie, Esther, who randomly provide entertainment in Unit 203 at night. Allie, Peter, Josiah, Matt, who are small group friends. Richard and Allen.

Fourth, I would like to thank members of the Biomedical Engineering administrative department: Joyce Bankert, Lisa Butler, Deon Grant, Hong Lan, for always helping me with paperwork and bureaucratic details. I cannot remember how many times I have approached them with nonsensical questions and they have resolved my problems seamlessly. I would be lost without their patient guidance.

Fifth, I would like to thank my friends/sisters from the east coast. They forced me to leave the comforts of lab but broadened my horizons and kept me sane:

Lim Kim, who is one of the warmest people I know. Her compassion and understanding for all kinds of people never fails to amaze me. Her spontaneity always keeps our friendship vibrant, and she is always taking me to a new tasty restaurant she found. Her cooking is also amazing.

Elfrida Tandar, who is one of the most responsible and organized people I know. I never worry or think about what I am supposed to be doing when I am with her. I can also count on her to be silly with me and accept me when I act oddly.

Grace Lioue, who is one of the most genuine and kind-hearted people I know. She always graciously goes out of her way to help others. I really admire her openness and appreciate all of emotional support she has given me.

Dorothy Wang, who is one of the most easy-going yet has her life together people I know. I really admire her time management skills and her ability keep a healthy work-life balance. I really appreciate all of the practical random life advice she gives me.

Other friends who have consistently made sure I was still alive even when they are far away: Iris Lam, who is always up for a fun time. Yong Wu, who always tells fun stories. Serena Tsang and Upasana Natarajan, my high school friends.

Last but not least, I would like to thank my family. They were a consistent source of support and prayer. Without them, none of my work would have been possible:

Jessie Niu, my mom who is always my go to person for prayer and words of truth. She has taught me a lot about what it looks like to be a praying mom. She is also one of the most progressive people I know, always willing to improve herself and expand her understanding of people and the world around her. My curious nature definitely comes from her. Also, I probably would have starved through graduate school if not for her constant meal deliveries.

Steve Niu, my dad who supports my every endeavor. He always pushes me to think about the future and how I can be more successful in life. His generosity with his resources, his patience, his kindness, and his easy-going personality are things I really admire about him and try to emulate. I definitely inherited my analytical and methodical thinking from him as well as my quirky sense of humor and playfulness.

Brian Niu, my brother who I really admire for his resolution in all he does to pursue God's heart. He has taught me a lot about music as well as the purpose of why we do what we do – for people. Also, Cassie Niu, my sister-in-law who joined the Niu team. I am really thankful for her prayers and support.

TABLE OF CONTENTS

CHAPTER 1

Introduction

In the current age of information and technology, most people, young and old, find it difficult to survive without electricity whether it is for work or for pleasure. Similarly, the human body is unable to maintain life without its own set of electrical signals. In biology, these electrical signals are generated by a careful balance of ions inside and outside the cell regulated by specialized proteins known as ion channels. While there are active and passive ion transporters where the general distinction lies in whether or not ion transport requires energy to be expended, this dissertation focuses on the regulation of a class of passive ion transporters known as high voltage-activated calcium (Ca^{2+}) ion channels.

The ion Ca^{2+} first came to the forefront of science in the 1880s when Sydney Ringer reported it was not important for cardiac muscle contraction then retracted this result and supported the exact opposite sentiment in a series of papers to the *Journal of Physiology* (Ringer, 1882). Despite its misunderstood beginning, Ca^{2+} captured the attention of many scientists and is now known to be involved in many physiological processes including muscle contraction, neurotransmission, gene transcription, inflammation, cell motility, cell growth, and cell death (Berridge et al., 2000; Clapham, 2007; Giorgi et al., 2018; Maier and Bers, 2002). Ca^{2+} influx through the membrane not only causes electrical excitability but also acts as an activator of different Ca^{2+} sensors that initiate downstream processes including calmodulin (CaM), troponin C, S100 proteins, protein kinases, and protease calpains (Carafoli and Krebs, 2016).

Given Ca^{2+}'s powerful and dramatic spectrum of influence in biological processes, meticulous regulation of this precious metallic ion is necessary to ensure life. The past few decades of voltage-gated Ca^{2+} channel research has identified four such important members of the L-type family and three members in the P/Q-, N-, and R-type families (Figure 1.1A). These channels have been found to be expressed in a variety of cell types including skeletal (Ca$_V$1.1) and cardiac muscle (Ca$_V$1.2 and Ca$_V$1.3), inner hair cells (Ca$_V$1.3), retina (Ca$_V$1.4), brain and nervous system (Ca$_V$1.3 and Ca$_V$2), and even in the pancreas (Ca$_V$1.3) (Zamponi et al., 2015).

Physiologically, Ca^{2+}-regulation of Ca$_V$1 is critical for skeletal muscle contraction (Bannister and Beam, 2013; Schneider and Chandler, 1973), cardiac electrical stability (Limpitikul et al., 2014; Mahajan et al., 2008), rhythmicity of oscillatory neurons (Chan et al., 2007; Huang et al., 2012), and vesicle release at ribbon synapses (Joiner and Lee, 2015), while Ca$_V$2 modulation contributes to short-term synaptic plasticity and spatial learning (Adams et al., 2010; Jackman and Regehr, 2017; Nanou et al., 2016). As a result, aberrant channel regulation underlies numerous maladies including cardiac arrhythmias (Venetucci et al., 2012; Zimmer and Surber, 2008), neurological and neuropsychiatric disorders (Adams and Snutch, 2007; Striessnig et al., 2010; Zamponi, 2016), and skeletal myotonia (Cannon, 2015).

Structurally, these channels are very similar. They contain four homologous domains covalently linked to one another by intracellular loops to form a “hole” in the membrane and are typically referred to as the pore-forming α_1-subunit (Figure 1.1B). Each domain contains six transmembrane segments. Transmembrane segment four (S4) is the voltage sensor generally encoded by a combination of four positively charged amino acids (arginines and lysines), and the extracellular loop between S5 and S6 forms the pore domain that distinguishes Ca^{2+} from other ions in solution to selectively allow its passage through the channel. Upon voltage depolarization, the positive charges in S4 moves and changes the conformation of the pore domain to a permissive conformation (Lacinova, 2005).

Remarkably, the biophysical properties of how these ion channels behave under electrical stimulation may be elementarily captured by the following simple equation:

$$I(V) = i(V) * N * P_O(V) \tag{1.1}$$

where V is the voltage stimulus, I is the total current passed through the membrane at V, i is unitary current according to the Goldman-Hodgkin-Katz equation at V, N is total number of channels in the membrane, and P_O is the open probability or likelihood for channel opening at V. Subsequently, proteins that interact with channels modulate one of these properties.

One example of this modulation is with auxiliary subunits. β-subunits are believed to bind to the intracellular loop between domain I and domain II (I-II loop) to increase surface membrane expression thus increasing N (Fang and Colecraft, 2011; Weiss and Zamponi, 2017). On the other hand, γ-subunits are thought to reduce expression and decrease N (Freise et al., 2000; Polster et al., 2016). Similarly, $\alpha_2\delta$ has been reported to increase number of channels on the plasma membrane as well as P_O (Weiss and Zamponi, 2017).

Another example is the Ca^{2+}-binding protein CaM. Though it remains controversial in the skeletal muscle, CaM has emerged as a dynamic regulator of neuronal and cardiac Ca^{2+} channels (Ben-Johny et al., 2015; Halling et al., 2006; Minor and Findeisen, 2010). The binding of CaM to the conserved carboxy-tail element, termed Ca^{2+}-inactivating (CI) module (Figure 1.1C), provides negative or positive feedback to the channel known as Ca^{2+}-dependent inhibition (CDI) and Ca^{2+}-dependent facilitation (CDF) respectively (Ben-Johny et al., 2015; Catterall et al., 2017; Minor and Findeisen, 2010; Saimi and Kung, 2002). Thus, depending on whether the binding occurs with the Ca^{2+}-free CaM (apoCaM) or Ca^{2+}-bound CaM (Ca^{2+}-CaM) the channel will exhibit an upregulation of the baseline open probability or relief of this initial enhancement manifesting as Ca^{2+}-dependent inactivation (CDI) (Adams et al., 2014).

Unfortunately, CaM regulation of Ca_V presents two sets of complications. First, the high sequence homology of the CI region poses a daunting challenge – mechanisms that tune Ca^{2+}/CaM-feedback must distinguish between structurally-similar targets. Second, CaM itself regulates an abundance of proteins performing vastly different functions (Marshall et al., 2015; Saimi and Kung, 2002). Not surprisingly, global inhibition of CaM alters numerous processes provoking unintended consequences (Persechini and Stemmer, 2002). In this regard, identifying pathways that individually adjust the gain of Ca^{2+}-feedback is critical.

Recently, Src homology 3 (SH3) and cysteine-rich domain (C1) proteins (stac) have been presented as attractive candidates for modulating Ca_V trafficking and gating (Polster et al., 2015; Rzhepetskyy et al., 2016; Suzuki et al., 1996). Initially found in various areas of the brain, stac became a protein of interest for Ca_V when it was first identified as a component of the excitation-contraction (EC) coupling machinery in association with debilitating congenital human myopathies (Grzybowski et al., 2017; Horstick et al., 2013; Nelson et al., 2013; Stamm et al., 2008). An autosomal-recessive disease was identified in a culturally-isolated population of Native Americans (Stamm et al., 2008), but has since been observed in Middle Eastern, African, and South American individuals (Grzybowski et al., 2017; Telegrafi et al., 2017). Patients present with symptoms of muscle weakness including short stature, kyphoscoliosis, talipes deformities, and drooping facial features and increased susceptibility to malignant hyperthermia (Grzybowski et al., 2017; Stamm et al., 2008; Telegrafi et al., 2017). Stac3 has been shown to abet plasmalemmal trafficking of $Ca_V1.1$, the voltage-gated Ca^{2+} responsible for EC coupling in skeletal muscle (Horstick et al., 2013; Linsley et al., 2017a; Polster et al., 2015). Functionally, homozygous KO of stac3 in mouse and zebrafish models led to markedly diminished $Ca_V1.1$ surface-membrane trafficking, reduced tetrad formation, loss of retrograde-signaling, and a near-complete loss of EC coupling (Horstick et al., 2013; Linsley et al., 2017a; Linsley et al., 2017b; Nelson et al., 2013; Polster et al., 2016; Polster et al., 2015). However, over-expression of a myopathy-associated mutant stac3 partially rescued channel trafficking though EC coupling remained reduced (Linsley et al., 2017a; Polster et al., 2016). In addition, the structural determinants of $Ca_V1.1$ that mediate stac binding also remain unknown (Campiglio and Flucher, 2017). Thus, stac3 may elicit multiple regulatory functions of $Ca_V1.1$ through direct interactions with the channel or mediated by other proteins (Linsley et al., 2017a; Polster et al., 2016).

Interestingly, co-expression of stac with $Ca_V1.2$ was also shown to suppress CDI (Polster et al., 2015). Even so, the specificity of stac in tuning Ca^{2+}-regulation of the broader Ca_V family, underlying molecular mechanisms, and their physiological functions remain to be fully elucidated (Wong King Yuen et al., 2017). Stac (Stac1-3) isoforms share a common architecture containing a C1 and two SH3 domains fused via a linker (Figure 1.2) and exhibit tissue-specific expression (Nelson et al., 2013; Suzuki et al., 1996). Stac1 and stac2 are expressed in various areas of the brain (Nelson et al., 2013; Suzuki et al., 1996), the peripheral nervous system (Legha et al., 2010), retina (Wilhelm et al., 2014), and hair cells in the inner ear (Cai et al., 2015), while stac3 is limited to the skeletal muscle (Nelson et al., 2013). Genomic and proteomic studies have also implicated stac in a variety of diseases including patent ductus arteriosus (Hsieh et al., 2014), periodontitis (Mizuno et al., 2011), cancer (Hardy et al., 2005; Mitra et al., 2010), erectile dysfunction, celiac disease, learning (Maciukiewicz et al., 2017), fat synthesis (Akiyama et al., 2015), and heart failure (di Salvo et al., 2015). In addition, biochemical studies have shown that stac interacts with other adapter proteins including poly[ADP-ribose] polymerase 2 (Troiani et al., 2011) and 14-3-3 necessary for immune function (Satoh et al., 2006).

Given these complications and discrepancies in understanding, this dissertation goes far to resolve general mechanisms by which stac modulates trafficking and gating Ca_V channels as well as debates surrounding $Ca_V1.1$ CaM-regulation to reveal long-sought physiological insights (Suzuki et al., 1996).

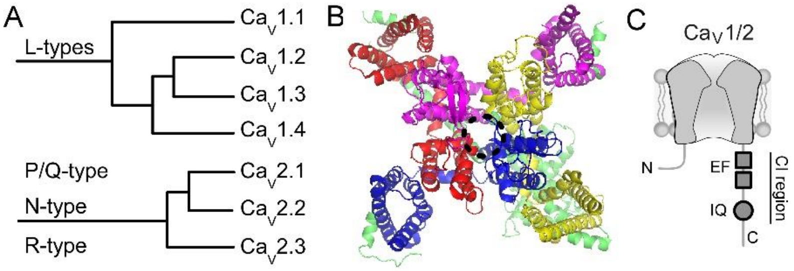

Figure 1.1. Structural homology of voltage-gated Ca^{2+} channels.
(A) Dendogram of the two sub-families of high-voltage activated Ca^{2+} channels.
(B) Crystal structure of $Ca_V1.1$. Domain I through IV highlighted in blue, red, magenta, and yellow respectively. Black dashed circle indicates pore region (pdb: 5GJV).
(C) Cartoon depiction of CaV1 and CaV2 with homologous CI region composed of two vestigial EF hands, pre-IQ segment, and IQ domain.

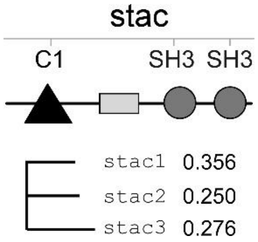

Figure 1.2. Stac isoforms possess conserved domains C1, similar to the cysteine rich domain found in protein kinase C, and SH3 domains. Fraction of homology comparison shown below for the three stac isoforms.

CHAPTER 2

Experimental Procedures

This chapter summarizes the protocols used to interrogate the biophysical and physiological properties of Ca^{2+} and Na^{+} channels in relation to various modulatory proteins.

Molecular biology – Ca$_V$1.1, Ca$_V$1.2, Ca$_V$1.3, Ca$_V$1.4$_{43*}$, Ca$_V$2.1, Ca$_V$2.2, Ca$_V$2.3, and Na$_V$1.4 variants were unmodified from previously published constructs: Ca$_V$1.1 was a gift from Kurt Beam (Colorado), Ca$_V$1.2 (NM001136522) (Wei et al., 1991), Ca$_V$1.2-G12-CaM$_{WT}$ (Mori et al., 2004), Ca$_V$1.3$_\Delta$ (AF370009.1), Ca$_V$1.3$_L$ engineered from Ca$_V$1.3$_\Delta$ and human long distal carboxyl tail (NM000718) (Liu et al., 2010), RNA edited variant Ca$_V$1.3$_{MQDY}$ (Bazzazi et al., 2013; Huang et al., 2012), Ca$_V$1.4$_{43*}$ was gifted from Dr. Soong Tuck Wah (National University of Singapore), Ca$_V$2.1 splice variant 37a(EFa) with 43$^+$/44$^-$/47$^-$ (Soong et al., 2002) was gifted from Dr. Terry Snutch (University of British Columbia), Ca$_V$2.2 (Jones et al., 1999), Ca$_V$2.3 (Mori et al., 2008), Na$_V$1.4 (Trimmer et al., 1990). Stac variants were purchased from Origene: human stac1 mRNA transcript 1 (NP003140.1), mouse stac2 (NP666140.1), and human stac3 isoform 2 (NP659501.1). U-peptide was synthesized by Genscript (KVDPVYETLRYGTSLALMNRSS). Fhf variants were gifted from Dr. Gordon Tomaselli and Dr. Jeremy Nathans (Johns Hopkins University).

RyR1 P2 domain was synthesized by Genscript (sequence in Supplementary Table 2.1). Ca$_V$1.1 CT chimeras were generated by first using PCR amplification with primers P01-P02 (primers listed in Table 2.1) and restriction enzyme cutting sites *XhoI* and *KpnI* to generate a silent mutation to create a unique *XbaI* site ~1-2 amino acids upstream of the EF hand and add an *MssI* restriction enzyme cutting site. Ca$_V$1.3 CI region was added to this construct by PCR amplification

(P03-P04) and inserted via *XbaI* and *MssI* restriction enzyme cutting sites. For the Ca$_V$1.1 variant by PCR amplification (P05-P06) and cutting sites *BglII*/*KpnI* to insert an *XbaI* cutting site in place of the stop codon. Then, glycine-(12)-CaM$_{WT}$ was PCR amplified (P07-P08) and inserted into stop-less Ca$_V$1.1 with *XbaI* and *KpnI*. Ca$_V$1.1$_{\Delta CT}$ was ordered from Genscript with the carboxy-tail truncated after residue 1397 (i.e. SILGPH*) and inserted with *XhoI* and *KpnI*. Ca$_V$1.1 (BBS) was generated by overlap PCR (P09-P12) and restriction enzyme sites *SalI*/*XhoI* to insert BBS. β_{2A}-glycine-(8)-CaM$_{WT}$ was unchanged from previously published rat β_{2A} modifications (Yang et al., 2014b). Using PCR amplification, we cloned CaM$_{1234}$ (P08, P13) into *NotI*/*BsrGI* to generate β_{2A}-glycine-(8)-CaM$_{1234}$. β_{2A}-glycine-(12)-RyR1 P2 was generated from PCR amplification (P14-P15) and inserted into β_{2A}-glycine-(32)-CaM$_{WT}$ from a previously published construct (Sang et al., 2016) with BsrGI and compatible ends NheI/XbaI. C1 of stac3 was PCR amplified (P16-P17) and cloned into pcDNA3 with NheI and BsrGI. NAM mutation was generated by QuikChange mutagenesis (P18-P19). Venus- and Cerulean-tagged constructs were generated by PCR amplification (P20-P23) and inserted via *NotI* and *XbaI* restriction enzyme cutting sites into previously published constructs (Sang et al., 2016). All constructs were verified with DNA sequencing.

Transfection of HEK293 cells – For whole-cell electrophysiology, HEK293 cells were cultured on glass coverslips in 10 cm dish and transfected using a calcium phosphate method (Peterson et al., 1999) with the following DNA combinations: 3 μg of SV40 T antigen to enhance expression, 2-8 μg of α_1-subunit of Ca^{2+} or Na^+ channel depending on expression, 8 μg from rat β_{2A} (Perez-Reyes et al., 1992) (M80545) or β_{1A} from mouse (NP112450.1), 8 μg from rat $\alpha_2\delta$ (Tomlinson et al., 1993) (NM012919.2), and either 8 μg of CaM variants, 8 μg of the stac1, stac2, or stac3 variants indicated, or RyR1 P2 variants as indicated. Similarly, for bungarotoxin-labelling, HEK293 cells were cultured in 60 mm dishes and transfected by calcium phosphate precipitation.

DNA concentration used was half that for electrophysiology conditions. Drugs were purchased from Sigma. Nifedipine and diltiazem were diluted to 1 mM in dimethyl sulfoxide (DMSO) while verapamil, ranolazine, and mexiletine were diluted to 10 mM in DMSO before added to cell culture media. Cells were incubated in the respective concentration of drugs for 24 h before electrophysiology or bungarotoxin-labelling.

For FRET-two hybrid experiments, HEK293 were cultured on glass-bottom dishes and transfected using a standard polyethylenimine protocol (Lambert et al., 1996). Epifluorescence was collected 1-2 days after transfection.

Adult guinea pig ventricular myocyte isolation – Adult guinea pig ventricular myocytes (aGPVMs) were isolated from whole hearts of Hartley strain guinea pigs 3-4 weeks old (250-350g). Guinea pigs were anesthetized via intraperitoneal injection with pentobarbital (35 mg/kg). Hearts were then excised, and single ventricular myocytes were isolated following a previously published protocol (Joshi-Mukherjee et al., 2013). Cells were plated on glass coverslips that were laminin (20 µg/mL) coated overnight at 4ºC.

Immunohistochemistry – Wildtype CD1 mouse brain coronal sections for immunohistochemistry were gifted from Dr. Dwight Bergles lab. Sections were washed in phosphate buffer saline (PBS) and then permeabilized with 0.3% Triton X-100 in PBS at room temperature for 10 min before incubated in blocking buffer containing 0.3% Triton X-100 and 5% normal donkey serum in PBS. Next, sections were incubated with primary antibody anti-STAC (stac1) antibody [EPR12805]-N-terminal diluted in blocking buffer (1:100, ab181157) overnight (16-18 hr) at 4ºC on a shaker and then washed with PBS for 5 min 3x. Sections were incubated with secondary antibody goat anti-rabbit IgG Alexa Fluor 594 (1:1000, ab150080) diluted in blocking solution for 2 hr at room temperature in the dark and then washed in PBS for 5 min 3x.

During the second wash, DAPI (1:10000, D21490) was added. Finally, sections were mounted on charged glass-slides with Aqua Ploy/Mount (18606, Polysciences, Inc.) and covered with a glass coverslip.

aGPVMs plated on glass coverslips were first washed 3x with cold PBS and then fixed in 3.7% paraformaldehyde (15710, Electron Microscopy Sciences) in PBS for 15 min. After washing 3x with PBS, cells were permeabilized in cold 0.5% Triton X-100 in tris buffered saline (TBS) for 20 min and then blocked with 10% goat serum in PBS for 1 hr at room temperature. Cells were incubated in primary antibodies monoclonal anti-α-actinin (sarcomeric) antibody produced in mouse (1:300, A7811) and stac1 (1:100) or anti-STAC2 (stac2) antibody-N-terminal (1:100, ab156080) in antibody diluent solution (IW-1000, IHC World) overnight at 4ºC. Next day, cells were rinsed 3x with 0.05% TWEEN20 (Sigma P9416) in TBS (TBS-T) for 5 min each. In the dark, cells were incubated with secondary antibodies, (1:1000), antibodies used: goat anti-mouse IgG1 Alexa Fluor 488 (1:1000, A21121), goat anti-rabbit IgG Alexa Fluor 594 (1:1000), and DAPI (1:10000) diluted in antibody solution for 45 min at room temperature and then washed 3x with TBS-T for 5 min each. Stained cells were mounted with prolong gold mounting media (Invitrogen) on a microscope slide (Fischer Scientific).

Transfected HEK293 were immunostained following a similar protocol as aGPVM but were not labelled with sarcomeric primary antibody and its respective secondary antibody.

Whole-cell electrophysiology – Whole-cell electrophysiology was performed at room temperature 1-4 days after transfection with Axopatch 200A (Axon Instruments). Glass pipettes were made from borosilicate glass (BF150-86-10, Sutter Instruments) to be 1-3 MΩ resistance with a horizontal puller (P-97; Sutter Instruments Company) and fire polisher (microforge, Narishige, Tokyo, Japan). We low-pass filtered recordings at 2 kHz, sampled at 10 kHz, and used

P/8 leak subtraction with 70% series resistance and capacitance compensation. Internal solution contained (in mM): $CsMeSO_3$, 114; $CsCl_2$, 5; $MgCl_2$, 1; MgATP, 4; HEPES, 10; BAPTA, 10; adjusted to 295 mOsm with $CsMeSO_3$ and pH 7.4 with CsOH. External solution contained (in mM): TEA-$MeSO_3$, 140; HEPES, 10; $CaCl_2$, 40; adjusted to 300 mOsm with TEA-$MeSO_3$ and pH 7.4 with TEA-OH. For measuring charge movements, we added 0.2 mM $LaCl_3$ and 1.0 mM $CdCl_2$ to the external solution. We used a holding potential of -80 mV, family of test pulses from -30 mV to +80 mV in 10 mV increments, and repetition interval of 20 s for all whole-cell recordings. Custom MATLAB (Mathworks) software was used to determine peak current, average peak densities, fraction of peak current remaining after 300 ms depolarization (r_{300}), and Ca^{2+}-CaM dependent inactivation (CDI, $f_{300} = r_{300/\mathrm{Ba}} - r_{300/\mathrm{Ca}} / r_{300/\mathrm{Ba}}$) plotted with SEM.

Peak current density-voltage curves were fit with the following equation:

$$J_{peak} = G_{max}(V - V_{rev})/\left(1 - exp\left[-\left(V - V_{1/2}\right)/k_G\right]\right) \tag{2.1}$$

where J_{peak} is the peak current density at test potential V, G_{max} is maximal channel conductance, V_{rev} is the reversal potential, $V_{1/2}$ is the half-activation voltage, and k_{G} is the slope factor (Table 2.2).

Normalized gating charge-voltage curves were fit with the following equation:

$$Q_{\mathrm{norm}} = Q_{\mathrm{max}} \cdot \left\{ \frac{f}{1 + \exp(-(V - V_{1/2,\,\mathrm{a}}) / SF_{\mathrm{a}})} + \frac{1 - f}{1 + \exp(-(V - V_{1/2,\,\mathrm{b}}) / SF_{\mathrm{b}})} \right\} \tag{2.2}$$

where Q_{norm} is the gating charge movement at voltage V normalized to value at + 80 mV. Gating charge movement is composed a double Boltzmann relation, with Q_{max} as saturating normalized gating charge, $V_{1/2.\mathrm{a}}$ and $V_{1/2.\mathrm{b}}$ are half-activating potentials for the two components, SF_{a} and SF_{b} are slope factors for the two components.

We incubated aGPVMs 24-48 hr after isolation in 5 µM ryanodine for 5-10 min before we collected whole-cell recordings with the same setup and Axopatch 200A or 200B (Axon Instruments). Internal solution was the same as used in HEK293 experiments except with the addition of 5 mM DTT and 5 µM ryanodine. Cells were sealed in Tyrodes solution, which contained (in mM): NaCl, 135; KCl, 5.4; $CaCl_2$, 1.8; $MgCl_2$, 0.33; NaH_2PO_4, 0.33; HEPES, 5; glucose, 5 (pH 7.4). External solutions for voltage-clamp protocol were the same as those used in HEK293. Welch's T-test was used to verify statistical significance between the population data. For CDI recordings, we determined required sample size based on power analysis. Based on historical estimates of normal variation in CDI/CDF measurements, we computed the sample size required such that type I and type II errors are 5% to be 3.5. Thus, we obtained at least 4 independent measurements for all electrophysiological experiments.

Current-clamp recordings of aGPVMs were performed on the same setup and were filtered at 5 kHz and sampled at 25 kHz. Internal solution contained (in mM): K glutamate, 130; KCl, 9; NaCl, 10; $MgCl_2$, 0.5; EGTA, 0.5, MgATP, 4; HEPES, 10; adjusted to pH 7.3 with KOH. External solution contained (in mM): NaCl, 135; KCl, 5.4; $CaCl_2$, 1.8; $MgCl_2$, 0.33; NaH_2PO_4, 0.33; HEPES, 5; glucose, 5 (pH 7.4). The time from upstroke to 80% repolarization (APD_{80}) was measured with custom MATLAB (Mathworks) software and used as a metric for comparing physiological output between peptide treated and untreated. For experiments with U-peptide, peptide was dissolved in ddH_2O to 2 mg/mL and then diluted to 500 nM in the appropriate internal solution.

Single-channel electrophysiology – Single-channel recordings were performed at room temperature using an on-cell configuration previously established in the laboratory (Tay et al., 2012) with same setup as whole-cell electrophysiology. Glass pipettes were pulled and polished from ultra-thick-walled borosilicate glass (BF200-116-10, Sutter Instruments) and coated with sylgard to have 5-10 MΩ resistance. Recordings were filtered at 2-5 kHz. Pipette solution contained (in mM): TEA-$MeSO_3$, 140; HEPES, 10; $BaCl_2$ 40; adjusted to 300 mOsm with TEA-$MeSO_3$ and pH 7.4 with TEA-OH. External solution contained (in mM): K glutamate, 132; KCl, 5; NaCl, 5; $MgCl_2$, 3; EGTA, 2; HEPES, 10; adjusted to 300 mOsm with glucose and pH 7.4 with KOH. Cell-attached single-channel currents were measured during 200 ms voltage ramps between -80 to +70 mV (portions between -50 and 40 mV displayed and analyzed) as previously described. For each patch, we recorded 80-150 sweeps with a repetition interval of 12 s. Patches were analyzed as follows: (1) The leak for each sweep was fit and subtracted from each trace. (2) The unitary current relation, $i(V)$, was fit to the open-channel current level using the following equation:

$$i(V) = -g \cdot (V - V_S) \cdot \exp(-(V - V_S) \cdot z \cdot F/(R \cdot T)) \ / \ (1 - \exp(-(V - V_S) \cdot z \cdot F/(R \cdot T))) \tag{2.3}$$

where g is the single-channel conductance (~0.2 pA/mV), z is the apparent valence of permeation (~2.1), F is Faraday's constant, R is the gas constant, and T is the temperature in degrees Kelvin (assumed room temperature). These parameters were held constant for all patches, except for slight variations in the voltage-shift parameter V_s ~35 mV, as detailed below. (3) All leak-subtracted traces for each patch were averaged (and divided by the number of channels in the patch) to yield an I–V relation for that patch. Since slight variability in V_S was observed among patches, we calculated an average V_S for each construct, $V_{S,AVE}$. The data from each patch was then shifted slightly in voltage by an amount $\Delta V = V_{S,AVE} - V_S$, with ΔV typically about ± 5 mV. This maneuver allowed all patches for a given construct to share a common open-channel GHK relation. Thus shifted, the I–V relations obtained from different patches for each condition/construct were then averaged together. (4) P_O at each voltage was determined by dividing the average I (determined in step 3 above) into the open-channel GHK relation. Channel number was determined by the maximal number of overlapping opening events upon application of the channel agonist Bay

K8644 (5 μM) at the end of each recording. For modal analysis, a dashed line discriminator was chosen to be average single-trial $P_O = 0.075$ such that traces with average single-trial $P_O > 0.075$ was categorized as high P_O while the remaining ones were considered low P_O.

Quantitative calcium photo-uncaging – All Ca^{2+}-uncaging experiments were conducted on a Nikon TE2000 inverted microscope with a Plan Fluor Apo 40× oil objective as previously described (Ben-Johny et al., 2014). Briefly, a classic Cairn UV flash photolysis system was used for Ca^{2+}-uncaging with brief UV pulses of ~1.5 ms in duration powered by a capacitor bank of up to 4000 μF charged to 200-290V. For concurrent Ca^{2+} imaging, Fluo4FF and Alexa568 dyes were dialyzed via patch pipet and imaged using Argon laser excitation (514 nm). Background fluorescence for each cell was measured prior to pipet dialysis of dyes and subtracted subsequently. A field-stop aperture was used to isolate fluorescence from individual cells. Dual-color fluorescence emission was attained using a 545DCLP dichroic mirror, paired with a 545/40BP filter for detecting Fluo4FF, and a 580LP filter for detecting Alexa568. Typically, uncaging experiments were conducted after ~2 minutes of dialysis of internal solution. Welch's T-test was used to verify statistical significance between the population data.

FRET-two hybrid assay – Three-cube FRET fluorescence of transfected HEK293 cells were measured on an inverted fluorescence microscope in 2 mM Ca^{2+} Tyrodes under resting Ca^{2+} intracellular concentrations and 10 mM Ca^{2+} Tyrodes incubated with 4 μM ionomycin (Sigma Aldrich) under Ca^{2+}/CaM conditions. Different concentrations and ratios of DNA were transfected to achieve a range of donor molecule (D_{free}) concentrations. FRET efficiency (E_A) for each individual cell was calculated (Erickson et al., 2001) and effective dissociation constants ($K_{d,\text{EFF}}$) was computed by fitting the binding curve: $E_A = [D_{\text{free}}]/(K_{d,\text{EFF}} + [D_{\text{free}}]) \cdot E_{A,\text{max}}$ iteratively. For stac3 NAM constructs where plateaus of FRET binding curves were not clearly defined by data, we assumed stac3 adopts the same conformation and possess the same $E_{\mathrm{A,max}}$ (Ben Johny et al., 2013).

Bungarotoxin-labelling assay – First, we washed transfected cells twice with DPBS (with Mg^{2+} and Ca^{2+}) (MediaTech). Then, we blocked unspecific binding sites with 3% BSA/DMEM for half an hour at room temperature. We incubated cells with 1 μM α-bungarotoxin-biotin (Invitrogen) in 3% BSA/DMEM for 1 h at room temperature in the dark. On ice and in the dark, cells were washed twice with DPBS, incubated 3 times for 5 min. with DPBS, and incubated for 1 h with 10 nM Qdot655 for flow cytometry or Qdot605 for confocal imaging (Invitrogen) in 3% BSA/DMEM. Finally, cells were washed with DPBS and imaged on the confocal microscope in 2 mM Ca^{2+} Tyrodes or harvested with trypsin, washed with PBS (without Mg^{2+} and Ca^{2+}), and resuspended for flow cytometry.

The total GFP fluorescence is proportional to the number of channels in a cell,

$$S_{\mathrm{G}} = N_{\mathrm{tot}} \cdot \alpha_{\mathrm{G}} \cdot I_0 \tag{2.4}$$

where α_{G} corresponds to the brightness of single GFP given the imaging setup and I_0 is the intensity of the excitation lamp. Similarly, the number of channels at the plasma membrane is given by,

$$S_{\mathrm{R}} = N_{\mathrm{surface}} \cdot (4 \cdot \alpha_{\mathrm{R}}) \cdot I_0 \cdot \varepsilon \tag{2.5}$$

where α_{R} corresponds to the brightness of single QD molecule when assessed through our imaging setup and I_0 is the intensity of the excitation lamp, and 4 corresponds to the stoichiometry for biotin-streptavidin interaction. The factor ε is the efficiency of QD labeling. The ratio of the two equations yields

$$\phi = \frac{S_{\mathrm{R}}}{S_{\mathrm{G}}} = \frac{N_{\mathrm{surface}}}{N_{\mathrm{tot}}} \frac{4 \cdot \alpha_{\mathrm{R}} \cdot \varepsilon}{\alpha_{\mathrm{G}}} = f_{\mathrm{mem}} \cdot \frac{4 \cdot \alpha_{\mathrm{R}} \cdot \varepsilon}{\alpha_{\mathrm{G}}} \tag{2.6}$$

and is proportional to the fraction of surface-membrane channels.

Confocal optical imaging – We captured exemplar images of bungarotoxin-labelled HEK cells with the Olympus Fluoview FV300 confocal laser scanning microscope and Fluoview software (Olympus). Using the Olympus PlanApo 403 or 603 oil objective (NA 1.40, PLAPO60XO3; Olympus), GFP was excited with an Argon Laser (488 nm), and Qdot-605 streptavidin conjugate (Invitrogen) was excited with Helium Neon (HeNe) Green Laser. Olympus optical filters used include 442/515 nm excitation splitter (FV-FCV), 570 nm emission splitter (FV-570CH), BA510 IF and BA530RIF for GFP emission channel, and 605BP filter for Qdot channel. Images were converted and merged on ImageJ.

Images of immunostained tissue slices and cells were captured with an LSM780 (Carl Zeiss, Oberkochen, Germany) confocal microscope. Similar settings were used for the LSM780 setup.

Flow cytometry – Fluorescence of harvested cells were measured with an Attune acoustic focusing flow cytometer (Life Technologies) in the “high-sensitivity” mode with a flow rate of 100 µL/min. We used the blue (488 nm) laser to excite GFP and Qdot to collect green and red fluorescence respectively. Green fluorescence was measured through the 574/26 optical filter. Likewise, red fluorescence was measured through the 640LP optical filter. Flow cytometer was calibrated and maintained as previously published (Lee et al., 2016). Control experiments prepared include un-transfected cells, GFP only cells, cells transfected with Ca$_V$1.1 and stac3 as a negative control, and cells with CaV1.1$_{BBS}$ and stac3 as a positive control. Data was exported as FCS files and analyzed with custom MATLAB (Mathworks) software.

Data processing statistical analysis – Raw data was gated by forward and side scatter signals to filter for single and healthy cells and green signals above 1.5×10^5 units were excluded because of non-linearities in flow cytometer measurements (Lee et al., 2016). Red signals above 2×10^5 units were excluded because of PMT saturation and accounted for <1% of total collected points. To correct for the true green (S_G) and red (S_R) signals, we averaged red signal ($\hat{S}_{R,blank}$) and green signal ($\hat{S}_{G,blank}$) of blank cells. We also calculated the slope for GFP bleed-through into the red channel ($f_{RED,GFP}$) due to the broadness of the GFP emission spectrum to be ~2.65%, yielding two equations: $S_G = \hat{S}_G - \hat{S}_{G,blank}$ and $\hat{S}_R = S_R - \hat{S}_{R,blank} - f_{RED,GFP} \cdot S_G$, where $\hat{S}_G$ is the raw green signal and S_{RED} is the red signal. Welch's t-test was used to statistically compare two trafficking conditions and p-value reports the probability for the null hypothesis that the respective ϕ_{max} for conditions compared are equal. To ensure robustness, we also used a rank-sum test. In all cases, the p-values for rank-sum test was similar to that with Welch's t-test. Number of independent trials and total number of cells analyzed are listed in Table 2.3.

***Langmuir analysis of Ca$_V$1.1 surface membrane trafficking* –** The lifecycle of an ion channel is complex involving the production of new channels, transport between multiple sub-cellular organelles, quality control, and protein degradation. While these events occur in distinct organelles, here we consider a simplified model to quantify changes in the proportion of surface-membrane trafficked channels elicited by the binding of a regulatory protein such as stac3 in single cells. Channels can thus be envisioned to traffic between the two compartments, the surface membrane and an aggregate internal compartment that includes organelles such as the ER, Golgi, and lysosome as schematized below.

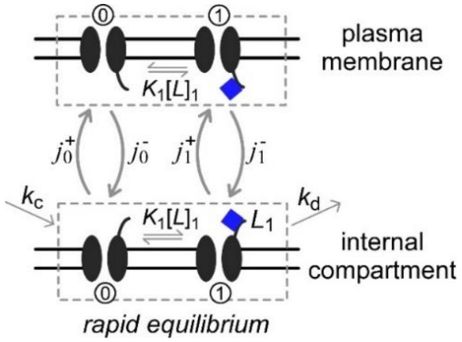

More specifically, channels are assumed to be produced within the internal compartment at a rate of k_c and degraded at a rate k_d. As fully folded channels feature binding sites accessible to cytosolic regulatory proteins, we assume that they may interact with the channel at both the plasmalemmal and internal compartments. Moreover, the transport of proteins between the two compartments is typically slow by comparison to binding and unbinding of regulatory proteins. Consequently, we assume that channel complexes are at 'rapid equilibrium' within each compartment.

The rate of forward trafficking and internalization for channel complexes may be different depending upon what regulatory proteins are bound. For simplicity, here we probe how the binding of a single regulatory molecule (L_1) alters channel surface-membrane trafficking. Thus, in both the internal and plasma-membrane compartments, the binding of regulatory agent interconverts channels between the unbound and bound conformations indexed by 0 and 1 respectively. For channel complexes without the pertinent regulatory protein, the rate of forward trafficking is j_0^+ while the rate of reverse trafficking is j_0^-. For channels bound to the regulatory molecule, the forward trafficking rate is j_1^+ and reverse trafficking rate is j_1^-. The differences in forward and reverse trafficking for the two classes of complexes ultimately lead to changes in the proportion of surface-membrane channels. Given 'rapid-equilibrium,' the dynamics of number of channels in internal (N_i) and plasma-membrane (N_{pm}) compartments are given by the following differential equations,

$$\frac{dN_{\mathrm{pm}}}{dt} = j_{\mathrm{eff}}^{+} \cdot N_{\mathrm{i}} - j_{\mathrm{eff}}^{-} \cdot N_{\mathrm{pm}} \tag{2.7}$$

$$\frac{dN_{\mathrm{i}}}{dt} = k_{\mathrm{c}} + j_{\mathrm{eff}}^{-} \cdot N_{\mathrm{pm}} - j_{\mathrm{eff}}^{+} \cdot N_{\mathrm{i}} - k_{\mathrm{d}} \tag{2.8}$$

where j_{eff}^{+} and j_{eff}^{-} are the effective rates of forward and reverse trafficking respectively. As the total number of channels $N_T = N_i + N_{pm}$, Eq. 2.7 can be simplified further as,

$$\frac{dN_{\mathrm{pm}}}{dt} = j_{\mathrm{eff}}^{+} \cdot (N_{\mathrm{T}} - N_{\mathrm{pm}}) - j_{\mathrm{eff}}^{-} \cdot N_{\mathrm{pm}} = j_{\mathrm{eff}}^{+} \cdot N_{\mathrm{T}} - (j_{\mathrm{eff}}^{+} + j_{\mathrm{eff}}^{-}) \cdot N_{\mathrm{pm}} \tag{2.9}$$

Moreover, the dynamics of the total number of channels is given as the sum of Eqs. 2.7 and 2.8,

$$\frac{dN_{\mathrm{T}}}{dt} = k_{\mathrm{c}} - k_{\mathrm{d}} \tag{2.10}$$

If k_{c} and k_{d} are constant with respect to time and N_{T}, then N_{T} will increase linearly with time post-transient transfection (t), i.e. $N_{\mathrm{T}} = (k_{\mathrm{c}} - k_{\mathrm{d}}) \cdot t$. That said, k_{c} and k_{d} are variable depending upon cellular regulatory factors and cell status, indicating that N_{T} may be non-linear with respect to time post-transfection. Nonetheless, if both k_{c} and k_{d} are slow in comparison to the rates of forward trafficking and reverse trafficking, then the pseudo-steady-state value for the number of plasma membrane channels, N_{pm}, can be obtained by setting Eq. 2.9 to be 0 as follows,

$$N_{\mathrm{pm}} = \frac{j_{\mathrm{eff}}^{+}}{j_{\mathrm{eff}}^{+} + j_{\mathrm{eff}}^{-}} \cdot N_{\mathrm{T}} \tag{2.11}$$

Thus, the fraction of membrane proteins is,

$$f_{\mathrm{mem}} = \frac{N_{\mathrm{pm}}}{N_{\mathrm{T}}} = \frac{j_{\mathrm{eff}}^{+}}{j_{\mathrm{eff}}^{+} + j_{\mathrm{eff}}^{-}} \tag{2.12}$$

Given rapid-equilibrium, the effective rate of forward trafficking is,

$$j_{\mathrm{eff}}^{+} = P_{0,\mathrm{i}} \cdot j_{0}^{+} + P_{1,\mathrm{i}} \cdot j_{1}^{+} \tag{2.13}$$

$P_{0,\mathrm{ic}}$ and $P_{1,\mathrm{ic}}$ corresponds to the probabilities that a channel in the internal compartment is either unbound or bound to regulatory ligand. Of note, these probabilities depend upon the concentration L_1 of the regulatory protein in the intracellular compartment.

$$P_{0,\mathrm{i}} = \frac{1}{1 + K_1 \cdot L_{1,\mathrm{i}}} \text{ and } P_{1,\mathrm{i}} = \frac{K_1 \cdot L_{1,\mathrm{i}}}{1 + K_1 \cdot L_{1,\mathrm{i}}} \tag{2.14}$$

Similarly, the net rate of internal trafficking is,

$$j_{\mathrm{eff}}^{-} = P_{0,\mathrm{pm}} \cdot j_0^{-} + P_{1,\mathrm{pm}} \cdot j_1^{-} \tag{2.15}$$

$P_{0,\mathrm{pm}}$ and $P_{1,\mathrm{pm}}$ corresponds to the probability that a channel in the plasma membrane compartment is either unbound or bound to the trafficking modulator. Akin to Eq. 2.14, these probabilities follow a Langmuir relation with the concentration of the trafficking modulator in the plasma membrane compartment ($L_{1,\mathrm{pm}}$),

$$P_{0,\mathrm{pm}} = \frac{1}{1 + K_1 \cdot L_{1,\mathrm{pm}}} \text{ and } P_{1,\mathrm{pm}} = \frac{K_1 \cdot L_{1,\mathrm{pm}}}{1 + K_1 \cdot L_{1,\mathrm{pm}}} \tag{2.16}$$

In the specific case of Stac3 and CaM that bind to channel cytosolic loops, $L_{1,\mathrm{pm}} = L_{1,\mathrm{i}} = L_1$ the cytosolic concentration of the trafficking modulator of interest. Thus, $P_{0,\mathrm{pm}} = P_{0,\mathrm{i}}$ and $P_{1,\mathrm{pm}} = P_{1,\mathrm{i}}$. Consequently,

$$\begin{aligned} f_{\mathrm{mem}} &= \frac{P_0 \cdot j_0^{+} + P_1 \cdot j_1^{+}}{P_0 \cdot j_0^{+} + P_1 \cdot j_1^{+} + P_0 \cdot j_0^{-} + P_1 \cdot j_1^{-}} \\ &= \frac{j_0^{+} + K_1 \cdot L_1 \cdot j_1^{+}}{j_0^{+} + j_0^{-} + K_1 \cdot L_1 \cdot (j_1^{+} + j_1^{-})} \end{aligned}$$

$$f_{\mathrm{mem}} = \frac{j_0^{+}}{j_0^{+} + j_0^{-}} + \left(\frac{j_1^{+}}{j_1^{+} + j_1^{-}} - \frac{j_0^{+}}{j_0^{+} + j_0^{-}} \right) \cdot \frac{K_1}{1/L_1 + K_1} \tag{2.17}$$

Recall that the surface-membrane trafficking ratio φ is given by,

$$\phi = \frac{S_{\mathrm{R}}}{S_{\mathrm{G}}} = \frac{4 \cdot \alpha_{\mathrm{R}} \cdot \varepsilon}{\alpha_G} \cdot f_{\mathrm{mem}} = \frac{4 \cdot \alpha_{\mathrm{R}} \cdot \varepsilon}{\alpha_G} \cdot \frac{j_0^{+}}{j_0^{+} + j_0^{-}} + \frac{4 \cdot \alpha_{\mathrm{R}} \cdot \varepsilon}{\alpha_G} \cdot \left(\frac{j_1^{+}}{j_1^{+} + j_1^{-}} - \frac{j_0^{+}}{j_0^{+} + j_0^{-}} \right) \cdot \frac{K_1}{1/L_1 + K_1} \tag{2.18}$$

where the constants α_{R}, α_{G}, and ε are as defined in the main text. Thus, if mutations were to specifically perturb the binding of the trafficking modulator L_1 to its effector interface on the channel, then then net fraction of surface-membrane channels will follow a Langmuir relation with the association constant (K_{a}) for the mutant. A specific relationship for stac3 is described as follows,

$$\phi_{\max}^{\text{stac3}} = \phi_{\max}^{\text{baseline}} + \varphi_{stac3} \cdot \frac{K_a}{K_a + \Lambda} \tag{2.19}$$

Based on our formulation (i.e. Eq. 2.18),

$\phi_{\max}^{\text{baseline}} = \frac{4 \cdot \alpha_{\text{R}} \cdot \varepsilon}{\alpha_G} \cdot \frac{j_0^+}{j_0^+ + j_0^-}$, $\varphi_{stac3} = \frac{4 \cdot \alpha_{\text{R}} \cdot \varepsilon}{\alpha_G} \cdot \left(\frac{j_{stac3}^+}{j_{stac3}^+ + j_{stac3}^-} - \frac{j_0^+}{j_0^+ + j_0^-} \right)$, and $\Lambda = 1/[\text{stac3}]$.

Primer	Sequence (5' to 3')
P01	cttctcctcgagTCCAGCACCATCTCCG
P02	tcagaatggtaccGTTTAAACTTAGTCTAGATGGTGAGGGCCCAGGATG
P03	cttctccatctagaCGAATTCAAAAGAATATGGTCTGAATATGA
P04	tcagaatgtttaaacCTAGAGCATCCGTTCAAGC
P05	cttctcgcggccgcTATCATGGACAACTTTGACTACC
P06	tcagaatggtaccgCCTCTAGACGGCCTGGGAGGAATAAG
P07	cttctctctagaGCGATCTCTAGAGGAGGTG
P08	tcagaatggtaccTCACTTCGCTGTCATCATTTG
P09	cttctcgtcgacAATGGAGCCATCCTCACC
P10	CCAGGCTGCTCTCGTAGTACCGCCACTGGTCCTCGAAGTCGTACCG
P11	CTACGAGAGCAGCCTGGAGCCCTACCCCGACACGGAAGTGCGACGC
P12	tcagaatctcgagACCCATGGAGATGAGAGAC
P13	cttctcgcggccgcTGGCGGTGGAGGCGGTGGAGGTGGCGCTGACCAACTGACTGAAG
P14	GAGGTCGCAGCCACA
P15	tcagaattgtacaTTAGCTAGCTCTGGTGACC
P16	cttctcgctagcGCCACCATGGAACTTCCCCCAGAG
P17	tcagaattgtacaCTAAGGTGGGATCTTGCCG
P18	TCCCCCGCCACGATTCTTCATTGGAGTCATCA
P19	TGATGACTCCAATGAAGAATCGTGGCGGGGGA
P20	cttctcgcggccgcTCACCTGGACGAGTTCAAGG
P21	tcagaattctagaTTACCCATAATATTCCTCCTGGCG
P22	cttctcgcggccgcTATGGAACTTCCCCCAGAG
P23	tcagaatgctagcCTAAATTTCCTCTAGAAAGTCGGT
RyR1 P2 domain	NFDPRPVETLNVIIPEKLDSFINKFAEYTHEKWAFDKIQNNWSYGENVDEELKTHPMLRPYKTFSEKDKEIYRWPIKESLKAMIAWEWTIEKAREGEEERTEKKKTRKISQTAQTYDPREGYNPQPPDLSGVTLSRELQAMAEQLAENYHNTWGRKKKQELEAKGGGTHPLLVPYDTLTAKEKARDREKAQELLKFLQMNGYAVTRAS

Table 2.1. List of primers and sequences.

Condition	Gmax (nS/nF)	Vrev (mV)	Vhalf (mV)	kG (mV)
Ca$_V$1.3, $\alpha_2\delta$, β_{2a}	1239.2.0±237.7	82.2±1.1	0.8±1.4	7.3±0.5
Ca$_V$1.1 (1 day), $\alpha_2\delta$, β_{2a}		N.D.		
Ca$_V$1.1-Ca$_V$1.3 CT, $\alpha_2\delta$, β_{2a}	460.0±82.0	96.7±2.2	42.5±1.9	10.8±0.5
Ca$_V$1.1, $\alpha_2\delta$, β_{2a}, CaM	763.3±205.4	86.7±2.1	39.7±1.6	10.8±0.4
Ca$_V$1.1, $\alpha_2\delta$, β_{2a}-CaM	624.3±113.9	88.8±2.0	37.3±2.1	10.2±0.3
Ca$_V$1.1, $\alpha_2\delta$, β_{2a}, stac3	978.0±177.7	81.7±3.3	29.9±1.8	10.1±0.3
Ca$_V$1.1-G-CaM, α2δ, β2a	266.7±92.8	101.7±6.0	40.0±5.0	11.8±0.2
Ca$_V$1.1(BBS), $\alpha_2\delta$, β_{2a}-CaM	790.0±3011.2	85.0±6.0	36.8±1.4	10.1±0.3
Ca$_V$1.1 (4 days), $\alpha_2\delta$, β_{2a}	189.2±23.1	73.8±5.2	36.3±2.5	9.5±0.3
Ca$_V$1.1, $\alpha_2\delta$, β_{2a}, stac3$_{W284S}$ + 0.5µM verapamil	1708.3±447.3	81.5±5.2	33.0±2.1	9.7±0.8

Table 2.2. Current-voltage parameters for whole-cell electrophysiology experiments and fit equation detailed in *Methods*. Values reported as average ± SEM.

Condition	# trials	# cells
$Ca_V1.1$, no β	2	18008
$Ca_V1.1$, no β, stac3	2	19925
$Ca_V1.1_{\Delta CT}$, β_{1a}	3	629
$Ca_V1.1_{\Delta CT}$, β_{2a}-CaM_{WT}	3	304
$Ca_V1.1_{\Delta CT}$, β_{1a}, stac3	3	548
$Ca_V1.1$, β_{2a}-CaM_{WT}	4	39972
$Ca_V1.1$, β_{2a}-$CaM_{WT,}$ CaM_{WT}	2	22459
$Ca_V1.1$, β_{2a}-CaM_{WT}, stac3	3	20055
$Ca_V1.1$, β_{2a}, stac3	5	64747
$Ca_V1.1$, β_{1a}, stac3, CaM_{WT}	5	71312
$Ca_V1.1$, β_{1a}, stac3 L[111]Δ	5	81648
$Ca_V1.1$, β_{1a}, stac3 L[111]Δ, CaM_{WT}	3	33545
$Ca_V1.1$, β_{1a}, stac3 K[288]*	5	58437
$Ca_V1.1$, β_{1a}, stac3 K[288]*, CaM_{WT}	4	11185
$Ca_V1.1$, β_{1a}, stac3W[284]S, CaM_{WT}	3	41228
$Ca_V1.1$, β_{1a}, stac3 W[284]S	9	107065
+no drug (24hr) + no wash (24 h)	3	20593
+2 µM ranolazine (24 h)	2	34094
+6 µM ranolazine (24 h)	2	32330
+3 µM mexiletine (24 h)	2	29616
+10 µM mexiletine (24 h)	2	22357
+0.15 µM nifedipine (24 h)	2	38387
+0.3 µM nifedipine (24 h)	2	33858
+0.25 µM diltiazem (24 h)	4	59120
+0.5 µM diltiazem (24 h)	3	45466
+wash day 1 (24 h)	3	18956
+0.5 µM verapamil (24 h)	4	66809
+1.0 µM verapamil (24 h)	3	36545
+1.0 µM verapamil (24 h) + wash (24 h)	3	18405
+1.0 µM verapamil (24 h) + no wash (24 h)	3	23608
$Ca_V1.1$, β_{1a}	4	23021
+1.0 µM verapamil (24 h)	2	18114
$Ca_V1.1$, β_{2a}	5	36106
+48 h	2	7694
+72 h	2	6227
+96 h	2	6073
$Ca_V1.1$, β_{2a}-CaM_{1234}	4	35731
$Ca_V1.1$, β_{2a}-RyR1(P2)	2	12474
$Ca_V1.1$, β_{1a}, stac3(C1)	3	9946
$Ca_V1.2$, β_{2a}	4	23476
$Ca_V1.2$, $\beta_{2a,}$ stac3	5	12018
$Ca_V1.1$, β_{1a}, CaM_{WT}	6	57821
+1.0 µM verapamil (24 h)	3	50551
+0.5 µM diltiazem (24 h)	3	49569
$Ca_V1.1$, β_{1a}, stac3	38	306786
+1.0 µM verapamil (24 h)	1	18210
+0.5 µM diltiazem (24 h)	1	19769

Table 2.3. Number of trials and cells analyzed for each trafficking experiment.

CHAPTER 3

Duplex signaling by CaM and stac3 enhances Ca$_V$1.1 function and unveils pharmacological insights for congenital myopathy

Central to excitation-contraction (EC) coupling in skeletal muscle, Ca$_V$1.1 is an L-type voltage-gated calcium (Ca^{2+}) channel that senses transmembrane depolarization to initiate Ca^{2+} release from the sarcoplasmic reticulum (SR) via the ryanodine receptor (RyR1) (Bannister and Beam, 2013; Schneider and Chandler, 1973). While its cardiac counterpart, Ca$_V$1.2, communicates with RyR2 via freely diffusing Ca^{2+} ions, Ca$_V$1.1 is conformationally coupled to RyR1 obviating the intermediary second messenger (Armstrong et al., 1972; Rios et al., 1992; Tanabe et al., 1990a). This intimate physical linkage warrants a precise geometric arrangement of the two partners in the skeletal myotube – four Ca$_V$1.1, termed tetrads, are disposed in ordered arrays that parallel RyR1 arrays at the surface-membrane/SR (peripheral-couplings) or tubular-membrane/SR (triad) interfaces (Franzini-Armstrong and Jorgensen, 1994; Lamb, 2000).

Fitting with this physiology, a cohort of auxiliary subunits such as β_{1A} (Schredelseker et al., 2009), $\alpha_2\delta$ (Obermair et al., 2005), γ_1 (Freise et al., 2000) and various SR proteins including RyR1 (Avila and Dirksen, 2000; Bannister et al., 2016; Nakai et al., 1996), junctional protein 45 (JP45) (Anderson et al., 2006), and junctophilin (Golini et al., 2011) tune Ca$_V$1.1 function. To identify essential signaling partners, a 'top-down' approach using primary cultures of skeletal myotubes obtained from gene knock-out (KO) models (Obermair et al., 2008) and cell-lines derived from dysgenic and normal myotubes have been insightful (Powell et al., 1996). However, such analyses have often reveal overlapping functions, whereby loss of a single protein dramatically alters Ca$_V$1.1 localization and/or gating to ultimately disrupt EC coupling. These effects may either be direct or indirect depending on other proteins present in the complex. Thus, quantifying the role of a given modulator on $\mathrm{Ca_V}1.1$ and the underlying regulatory mechanism is challenging. Intriguingly, recent studies have revealed that both calmodulin (CaM) (Ohrtman et al., 2008; Stroffekova, 2008) and stac3 regulate $\mathrm{Ca_V}1.1$ though underlying mechanisms remain to be fully elucidated (Horstick et al., 2013; Linsley et al., 2017a; Polster et al., 2015).

To resolve these complex channel regulatory mechanisms, a 'bottom-up' approach whereby the effects of individual signaling molecules on $\mathrm{Ca_V}1.1$ gating and trafficking are probed in a simplified system without an elaborate SR or t-tubules would be greatly beneficial (Dascal et al., 1992; Perni et al., 2017; Polster et al., 2015). However, functional analysis of $\mathrm{Ca_V}1.1$ and its modulation by various signaling molecules in non-muscle cell systems remain challenging (Dascal et al., 1992; Johnson et al., 1997; Perez-Reyes et al., 1989; Polster et al., 2015). While homologous $\mathrm{Ca_V}1.2$, $\mathrm{Ca_V}1.3$ and $\mathrm{Ca_V}1.4$ all exhibit reliable surface-membrane trafficking in heterologous systems in the presence of $\alpha_2\delta$ and β auxiliary subunits (Catterall, 2000; McRory et al., 2004; Mikami et al., 1989; Xu and Lipscombe, 2001), $\mathrm{Ca_V}1.1$ is thought to be retained in internal organelles (Linsley et al., 2017b; Polster et al., 2015). Countering this classical purview, however, a recent functional study demonstrated that the cytosolic adaptor protein stac3 with the $\alpha_2\delta$/β-subunits, enabled $\mathrm{Ca_V}1.1$ expression in human derived tsA201 cells (Polster et al., 2015). Further analysis suggested that additional factors including the transmembrane γ_1 subunit may also permit $\mathrm{Ca_V}1.1$ expression in tsA201 cells (Polster et al., 2016). The contrasting molecular requirements that permit $\mathrm{Ca_V}1.1$ expression in heterologous systems obfuscate general principles that underlie channel trafficking and precludes systematic analysis of channel gating.

In this chapter, we demonstrate that $\mathrm{Ca_V}1.1$, in fact, traffics to the plasma membrane of recombinant cell systems in the presence of auxiliary $\alpha_2\delta$ and β-subunits alone. However, this baseline expression is lower than that for homologous L-type channels. Moreover, electrophysiological analysis reveals tiny ionic currents suggesting that $Ca_V1.1$ has a low baseline P_O. Both CaM and stac3 enhance both surface-membrane trafficking and baseline P_O of $Ca_V1.1$. Moreover, we demonstrate that stac3 binds to the CT of $Ca_V1.1$, and stac3 mutations associated with congenital myopathy weaken this interaction resulting in reduced channel surface-membrane trafficking. Delivery of CaM to the channel complex can strikingly reverse this trafficking defect. Interestingly, long-term application of small-molecule Ca_V modulators diltiazem and verapamil yields a partial rescue of channel trafficking.

RESULTS

The carboxy-terminus is a structural determinant for functional expression of $Ca_V1.1$ **–** In comparison to other L-type Ca channels, $Ca_V1.1$ expresses poorly in heterologous cell systems (Perez-Reyes et al., 1989; Polster et al., 2015). Figure 3.1A shows exemplar inward Ca^{2+} current elicited in response to a voltage-step depolarization from a HEK293 cell transiently expressing $Ca_V1.3$ pore-forming α_1 subunit with auxiliary β_{2A} and $\alpha_2\delta$ subunits. Population data of average peak current densities elicited in response to a family of step-depolarizations further illustrate robust expression of $Ca_V1.3$ in HEK293 cells (Figure 3.1A). In contrast, when $Ca_V1.1$ α_1 subunit is coexpressed with both β_{2A} and $\alpha_2\delta$ auxiliary subunits, we observe minimal ionic currents (Figure 3.1B). Given the functional difference between $Ca_V1.1$ and $Ca_V1.3$ despite their overall structural similarity, we undertook a chimeric approach by exchanging the carboxy-terminus (CT) of $Ca_V1.1$ α_1 subunit with that of $Ca_V1.3$ to identify motifs that enable channel function. Electrophysiological analysis revealed robust currents for the chimeric channels (Figure 3.1C) suggesting that the CT is a key determinant for functional expression.

One possibility is that $\mathrm{Ca_V}$ channel function may be enabled by modulatory partners that interact with the CT interface. For nearly all $\mathrm{Ca_V}$1/2 channels, CaM is one such well-established partner known to modulate channel function (Lee et al., 2000; Liang et al., 2003; Peterson et al., 1999; Pitt et al., 2001; Qin et al., 1999; Singh et al., 2006; Yang et al., 2006; Zuhlke et al., 1999). Consequently, we explored differences in CaM binding to $\mathrm{Ca_V}$1.3 versus $\mathrm{Ca_V}$1.1 using FRET (Forster Resonance Energy Transfer) two-hybrid binding assay (Erickson et al., 2001) in live cells. We co-expressed cerulean-tagged CaM (Cer-$\mathrm{CaM_{WT}}$) with venus-tagged $\mathrm{Ca_V}$1.3 CT including the dual vestigial EF hands, the preIQ and IQ domains (Ven-$\mathrm{Ca_V}$1.3 CI) and measured FRET efficiency (E_A) between the donor-acceptor pair (Figure 3.1G). As cells transfected with these constructs variably express the fluorophore-tagged partners, E_A measured from single cells follow a Langmuir binding relation with the free concentration of the donor. The $\mathrm{Ca_V}$1.3 CI exhibited strong binding to Cer-$\mathrm{CaM_{WT}}$ under both basal and elevated $\mathrm{Ca^{2+}}$-conditions (Figure 3.1H and Figure 3.1G respectively) consistent with prior studies (Ben Johny et al., 2013). In contrast, FRET two-hybrid analysis of Venus-tagged $\mathrm{Ca_V}$1.1 CI (Ven-$\mathrm{Ca_V}$1.1 CI) and Cer-$\mathrm{CaM_{WT}}$ showed weaker binding under both basal and elevated $\mathrm{Ca^{2+}}$-conditions (Figure 3.1J and Figure 3.1I respectively). Thus, the lack of functional expression of $\mathrm{Ca_V}$1.1 versus $\mathrm{Ca_V}$1.3 in heterologous systems may be the consequence of weak or absent CaM binding. If so, then reinstatement of CaM to $\mathrm{Ca_V}$1.1 should rescue channel function. Consequently, we overexpressed CaM with $\mathrm{Ca_V}$1.1 and its auxiliary subunits and demonstrated partial rescue of functional $\mathrm{Ca^{2+}}$ currents (Figure 3.1D). Furthermore, to ensure robust CaM binding, we localized CaM to the $\mathrm{Ca_V}$1.1 complex by fusion to the β_{2A} auxiliary subunit. This manipulation also enabled functional expression of $\mathrm{Ca_V}$1.1 in HEK293 cells (Figure 3.1E). Thus, CaM binding to $\mathrm{Ca_V}$1.1 permits its functional expression in heterologous systems.

Next, we explored whether other modulatory partners also enable channel function via binding to the $Ca_V1.1$ CT. Recent studies have reported that $Ca_V1.1$ currents can be re-established in HEK293 cell systems by co-expression of stac3 (Polster et al., 2015), an adaptor protein essential for skeletal muscle function. While stac is structurally unrelated to CaM, we considered whether stac might mimic CaM action in the context of skeletal muscle, and rescue channel function by binding to channel CT. Exemplar current trace and population data (Figure 3.1F) confirm robust $Ca_V1.1$ functional expression in HEK293 cells following co-expression of stac3. FRET two-hybrid analysis of Cer-tagged stac3 with Ven-$Ca_V1.1$ CI revealed strong binding (Figure 3.1K) with $K_{d,EFF} \sim 12000$ D_{free} units ~ 400 nM. Thus, the occupancy of $Ca_V1.1$ CT appears to be closely linked to proper channel function and an emerging repertoire of CT-binding proteins may modify Ca_V function in heterologous and native cells via redundant mechanisms (Flynn and Altier, 2013; Hall et al., 2013; Marshall et al., 2011; Park et al., 2010; Wang et al., 2010).

CaM and stac enhance $Ca_V1.1$ surface membrane trafficking – As both CaM and stac partially rescue $Ca_V1.1$ function, we sought to discern underlying molecular mechanisms. The functional expression of ion channels may be enhanced from changes in three vital parameters: 1) the number of channels at the surface membrane dictated by protein trafficking, 2) ion permeation, and 3) channel gating.

To quantify the relative fraction of channels at the cell surface membrane, we used a dual labeling approach (Yang et al., 2010) whereby the α_1 subunit is tagged with both a GFP on the cytoplasmic amino-terminus and an external epitope composed of a 13 amino-acid α-bungarotoxin-binding site (BBS) inserted into the extracellular loop (Figure 3.2B, $Ca_V1.1_{BBS}$). To label surface membrane channels, we incubate cells with cell-impermeable biotin-conjugated α-bungarotoxin and visualize using streptavidin covalently attached to a red quantum dot (QD) while the total expression of $\mathrm{Ca_V1.1}$ in a cell is determined by monitoring the GFP fluorescence (Sekine-Aizawa and Huganir, 2004). The high affinity and specificity of bungarotoxin for the BBS site facilitates reliable detection of surface-membrane $\mathrm{Ca_V1.1}$ with minimal background fluorescence (Sekine-Aizawa and Huganir, 2004). We first verified the functionality of $\mathrm{Ca_V1.1_{BBS}}$ by co-transfecting β_{2a}-$\mathrm{CaM_{WT}}$ into HEK cells. The resultant $\mathrm{Ca^{2+}}$ currents exhibited comparable properties as the unmodified $\mathrm{Ca_V1.1}$ (Figure 3.2A). We probed baseline plasmalemmal expression for $\mathrm{Ca_V1.1_{BBS}}$ in the presence of β_{2A} and $\alpha_2\delta$ subunits using confocal imaging (Figure 3.2B). The left subpanel shows the transmitted light image of an exemplar cell, the middle subpanels show green (S_G) and red (S_R) fluorescence images indicating GFP from total channels and QD emissions from plasmalemmal channels respectively. The far-right merged image showcases the difference in intracellular and extracellular labeling of $\mathrm{Ca_V1.1_{BBS}}$. While strong GFP fluorescence is evident, external QD labeling is sparse indicating poor surface-membrane expression of $\mathrm{Ca_V1.1}$ (Figure 3.2B). That said, we did observe some surface-membrane labeling in a few cells suggesting that $\mathrm{Ca_V1.1}$ with just $\alpha_2\delta$ and β subunits might be sufficient for surface-membrane trafficking, albeit with a poor efficacy. Analysis of external epitope labeling from a multitude of individual cells would help resolve such ambiguities.

Accordingly, we used flow cytometric analysis to quantify surface-membrane trafficking at a population level by determining the total GFP (S_G) and QD (S_R) fluorescence from individual cells. For a given cell, the ratio of red to green fluorescence ($\phi = S_R/S_G$) is proportional to the fraction of surface-membrane channels (f_{mem}) and serves as a quantifiable metric for trafficking efficacy (as described in Chapter 2),

$$\phi = \frac{S_{\mathrm{R}}}{S_{\mathrm{G}}} = \frac{N_{\mathrm{surface}}}{N_{\mathrm{tot}}}\frac{4\cdot\alpha_{\mathrm{R}}\cdot\varepsilon}{\alpha_{\mathrm{G}}} = f_{\mathrm{mem}}\cdot\frac{4\cdot\alpha_{\mathrm{R}}\cdot\varepsilon}{\alpha_{\mathrm{G}}} \tag{2.6}$$

The factors α_R and α_G are brightness of single QD and GFP fluorophores respectively and ε is the efficiency of labeling. Given this framework, we plotted S_R versus S_G obtained from individual cells expressing $Ca_V1.1_{BBS}$ with β_{2A} and $\alpha_2\delta$ subunits after one day of transfection (Figure 3.2C). Consistent with confocal imaging data, flow-cytometric analysis showed a mixed population of cells – a small fraction exhibits minimal surface-membrane labeling ($S_R = 0$), while another demonstrates reliable QD labeling ($S_R > 0$). Binned data reveal a saturating relationship for S_R as S_G increases, with a maximal value of ~ 1923 ± 51 (fluorescence units). We estimated the saturating surface-membrane trafficking limit (ϕ_{max}) as the mean ratio ϕ for individual cells exhibiting high GFP fluorescence (i.e. $5.4\times10^4 \leq S_G \leq 1.4\times10^5$) to be 0.0225 ± 0.0006. Here, we exclude values above 1.4×10^5 GFP fluorescence units because of previously identified non-linearities in fluorescence measurements from our flow cytometer above this value (Lee et al., 2016). In comparison, the ϕ_{max} for $Ca_V1.2_{BBS}$ is approximately 0.0276 ± 0.0004 (Figure 3.2J). Of note, culturing transfected HEK293 cells for multiple days at 30ºC, to reduce channel endocytosis, further enhances $Ca_V1.1$ surface-membrane trafficking (Figure 3.2I). This surprising finding furnishes a convenient strategy to study baseline properties of $Ca_V1.1$ in the absence of various regulatory proteins and sets the stage for mechanistic studies that assess effects on channel gating.

With surface-membrane expression of $Ca_V1.1$ confirmed, we next sought to identify core-requirements for channel plasmalemmal trafficking. For other L-type channels, the auxiliary β subunits are necessary for efficient surface-membrane trafficking (Buraei and Yang, 2010; Dolphin, 2003; Fang and Colecraft, 2011; Perez-Reyes et al., 1992). Indeed, $Ca_V1.1_{BBS}$ exhibits no QD labeling in the absence of β subunits (Figure 3.2J), suggesting that the β subunit is obligatory for plasma-membrane expression echoing findings in skeletal myotubes based on KO mouse models (Schredelseker et al., 2005). Consequently, we explored $Ca_V1.1$ plasmalemmal trafficking in the presence of β_{1A} subunits that are endogenous to skeletal myotube. Much as with β_{2A} co-expression, confocal imaging (Figure 3.2H) and population analysis (Figure 3.2I) revealed weak but detectible QD labeling of $Ca_V1.1_{BBS}$ in the presence of β_{1A} subunits.

With baseline requirements for plasmalemmal expression of $Ca_V1.1$ firmly established, we probed the effect of CaM and stac3 on overall channel trafficking. When CaM is delivered locally to $Ca_V1.1_{BBS}$ via β_{2A}-CaM, QD labeling is markedly enhanced hinting at improved plasmalemmal localization (Figure 3.2D). Flow cytometric analysis of $Ca_V1.1$ co-expressed with β_{2A}-CaM revealed an overall enhancement in the QD labeling in comparison to levels with the β_{2A} subunit alone ($p < 1E\text{-}5$) (Figure 3.2E; Figure 3.2J) or with β_{2A} fused to a sham payload, the P2 domain of RyR1 ($p < 1E\text{-}5$) (Figure 3.2J). Interestingly, this increase in surface membrane expression with CaM seemed largely Ca^{2+}-dependent. Co-expression of a mutant CaM (β_{2A}-CaM_{1234}), which possesses low Ca^{2+} binding due to alanine substitution of Ca^{2+}-coordinating residues, with $Ca_V1.1_{BBS}$ only marginally enhanced QD labeling ($p = 0.048$) in comparison to coexpression with β_{2A} alone (Figure 3.2J). Likewise, the surface membrane expression of $Ca_V1.1$ bound to the skeletal muscle β_{1A} subunit is also enhanced significantly with co-expression of CaM as a separate molecule ($p < 1E\text{-}5$) (Figure 3.2J). We next explored whether stac3 also enhances the surface-membrane trafficking of $Ca_V1.1$. Confocal imaging (Figure 3.2F) and flow cytometric analysis (Figure 3.2G) revealed a substantial enhancement in QD labeling for $Ca_V1.1_{BBS}$ with stac3 in the presence of both β_{2A} ($p < 1E\text{-}5$) and β_{1A} ($p < 1E\text{-}5$) subunits (Figure 3.2J). Moreover, co-expression of the C1 domain of stac3 alone also increased surface-membrane trafficking though partially ($p < 1E\text{-}5$) (Figure 3.2J), fitting with prior analyses showing that this domain is critical for channel localization at the skeletal muscle triad (Campiglio and Flucher, 2017). Even so, in the absence of a β-subunit, $\mathrm{Ca_V1.1_{BBS}}$ exhibited minimal surface-membrane expression even with co-expression of stac3 (Figure 3.2J).

As stac3 and CaM both interact with the CT, we sought to directly probe whether this binding is functionally critical for $\mathrm{Ca_V}1.1$ trafficking. Accordingly, we reasoned that the deletion of the CT, $\mathrm{Ca_V1.1(\Delta CT)_{BBS}}$, would abrogate stac3- and CaM-mediated enhancement in $\mathrm{Ca_V}1.1$ trafficking. Remarkably, coexpression of $\mathrm{Ca_V1.1(\Delta CT)_{BBS}}$ with β_{1A} and $\alpha_2\delta$ shows significant enhancement in trafficking in comparison to the wildtype channel (p < 1E-5) (Figure 3.2J). However, co-expression of either β_{2A}-CaM ($p = 0.4$) or stac3 ($p = 0.11$) does not further enhance surface-membrane trafficking of $\mathrm{Ca_V}1.1$ (Figure 3.2J). Thus, both CaM and stac3 can individually enhance the surface-membrane expression of $\mathrm{Ca_V}1.1$ via interaction with the CT; however, this enhancement appears to be conditional on the presence of a bound β subunit.

Distinct binding sites on the CT allow CaM and stac3 to act independently **–** Given that both CaM and stac3 bind to the channel carboxy-tail to enhance surface-membrane expression, we examined whether these agents act independently or through a shared endpoint. Consequently, to further delineate the CT binding interface for stac3 and CaM, we parsed the CT into three distinct segments: dual vestigial EF hands, pre-IQ, and IQ domains. Using FRET 2-hybrid assay, we probed binding between Venus-tagged channel segments and Cerulean-tagged CaM or stac3. $\mathrm{Ca^{2+}}$/CaM exhibits a markedly higher affinity to the pre-IQ and IQ domains in comparison to the dual vestigial EF hand segments (Figure 3.3A-B). By contrast, stac3 preferentially binds to the dual vestigial EF hand segments in comparison to the preIQ and IQ domains (Figure 3.3C-D). These findings demonstrate that stac3 and CaM prefer distinct CT interfaces.

Thus, we probed surface-membrane labeling of $\mathrm{Ca_V1.1_{BBS}}$ in the presence of both β_{2A}-CaM and stac3. If the two agents act through a shared endpoint, then their combination will not further increase trafficking. However, flow cytometric analysis revealed that the two agents combinatorically enhance the trafficking of $Ca_V1.1_{BBS}$ nearly 6-fold suggesting that they act independently through distinct sites on the CT (p < 1E-5) (Figure 3.3E-G). Analogously, $Ca_V1.1_{BBS}$ expressed with β_{1A}, CaM, and stac3 yields an 8-fold increase in trafficking. By contrast, co-expression of freely-diffusing CaM with $Ca_V1.1_{BBS}$ and β_{2A}-CaM did not further enhance trafficking (p = 0.13) (Figure 3.3G) suggesting that the additive effect here did not result from incomplete saturation of channel CT by CaM. Together, these findings suggest that $Ca_V1.1$ plasmalemmal trafficking is enriched by a duplex signaling mechanism.

CaM and stac3 enhance the open probability of $Ca_V1.1$ – With the role of CaM and stac3 on $Ca_V1.1$ trafficking established, we probed their effects on channel gating. However, as the activation of $Ca_V1.1$ is right-shifted to near its reversal potential (Table 2.2), detecting single-channel openings reliably in an 'on cell' configuration is challenging as the unitary currents at these voltages are small. Thus, to estimate changes in the maximal open probability, we analyzed macroscopic I_{tail} and overall gating charge movement. More specifically, the peak I_{tail} is linearly proportional to both the steady-state P_O of the channel at the activating pre-pulse potential and the number of surface-membrane channels. However, the total gating charge moved at the reversal potential (q_{rev}) is proportional to the number of surface-membrane channels. Gating charges can be isolated by blocking ion currents with heavy metals Cd^{2+}/La^{3+}. Thus, the ratio, I_{tail} / q_{rev}, is linearly proportional to P_O and serves as a convenient proxy to estimate changes in $P_{O,max}$ under various conditions.

While our initial functional studies failed to detect appreciable $Ca_V1.1$ currents with auxiliary β_{2A} and $\alpha_2\delta$ subunits co-expressed (Figure 3.1B), these experiments were conducted one day following transient transfection. Our trafficking studies instead showed that $Ca_V1.1$ surface-membrane expression with the same subunits is substantially enhanced ($p < 1E-5$) several days following transient transfection (Figure 3.2I). As such, we conducted whole-cell patch clamp experiments of $Ca_V1.1$ with auxiliary β_{2A} and $\alpha_2\delta$ subunits four days following transfection. Scrutiny of current recordings revealed substantial gating currents in response to a 100-ms activating pulse to +80 mV indicating the presence of surface membrane channels (Figure 3.4A; labeled Q). The duration of the activating pulse was chosen to accommodate the ultra-slow activation of $Ca_V1.1$, but the tail currents (I_{tail}) elicited at 0 mV following this activation pulse was comparatively small. Moreover, blockade of ionic currents revealed both 'ON' gating current, in response to a depolarizing pulse, and 'OFF' gating current during repolarization (Figure 3.4B). Computing I_{tail} / q_{rev} demonstrated low saturating values consistent with a diminished baseline $P_{O,max}$ of $Ca_V1.1$ channels (Figure 3.4C). Moreover, normalized 'ON' and 'OFF' gating charges plotted as a function of voltage overlays upon each other demonstrating that Q_{ON} and Q_{OFF} were similar in magnitude and voltage-dependence (Figure 3.4D; Figure 3.4S). In contrast, with CaM or β_{2A}-CaM co-expressed, $Ca_V1.1$ produce markedly enhanced I_{tail} (Figure 3.4E and Figure 3.4I) with similar gating currents (Figure 3.4F and Figure 3.4J). Further analysis shows that the saturating value of I_{tail} / q_{rev} is ~ 5-fold enhanced in the presence of CaM (Figure 3.4G, $p = 0.006$) or β_{2A}-CaM (Figure 3.4K, $p = 0.004$) suggesting that CaM upregulates $P_{O,max}$. Reassuringly, normalized Q_{on} and Q_{off} were similar in magnitude in the presence of CaM and β_{2A}-CaM (Figure 3.4H and Figure 3.4L). In like manner, overexpression of stac3 also resulted in enhanced I_{tail} / q_{rev} ($p = 0.006$) for $Ca_V1.1$ (Figure 3.4M-P). These results indicate that both CaM and stac upregulates the maximal P_O of $Ca_V1.1$ (Figure 3.4Q). Reassuringly, further quantification of gating charge density at +80 mV ($Q_{density}(+80)$) shows significant increase for β_{2A}-CaM ($p = 0.039$) and stac3 ($p = 0.045$), confirming modulatory agents also enhance trafficking of $Ca_V1.1$ to the plasma membrane (Figure 3.4R). Together, these data suggest that both modulators not only boost surface-membrane expression, but also upregulate the activity of $Ca_V1.1$. The CaM-dependent change in maximal P_O is reminiscent of findings with related $Ca_V1.3$ channels (Adams et al., 2014).

Myopathy-associated stac3 mutants diminish $Ca_V1.1$ surface-membrane trafficking – Recent genetic screens have identified multiple mutations within the stac3 gene that are associated with severe congenital myopathies as illustrated in Figure 3.5A. The first autosomal recessive mutation observed in patients of the Lumbee Native American tribe were homozygous missense mutation (W[284]S) in the first SH3 domain of stac3 (Stamm et al., 2008). Subsequently, compound heterozygous variants (K[288]* and L[111]Δ) were identified in a patient of Turkish heritage (Grzybowski et al., 2017). Given that stac3 binds to the $Ca_V1.1$ CT, we considered whether myopathy-associated mutants may disrupt this interaction and diminish surface-membrane trafficking.

Using FRET-two hybrid assay, we assessed the binding of Ven-tagged $Ca_V1.1$ CI and Cer-tagged stac3 variants (Figure 3.5B). In comparison to wild-type, all three disease-associated stac3 variants exhibited a spectrum of weakened binding affinities (Figure 3.5C; black: WT, red: mutant). Stac3 variants, L[111]Δ and W[284]S, showed a nearly 10-fold weakened affinity while the mutation K[288]* resulted in a 2-fold reduced binding of $Ca_V1.1$ carboxy-terminus (Figure 3.5J). To discern analogous functional changes, we compared the surface-membrane trafficking of $Ca_V1.1_{BBS}$ with wildtype or mutant stac3 in the presence of both β_{1A} and $\alpha_2\delta$ subunits. Upon co-expression of wildtype stac3, $Ca_V1.1_{BBS}$ showed strong QD labeling confirmed by confocal imaging (Figure 3.5D) and flow cytometric analysis (Figure 3.5E and Figure 3.5K) suggesting robust surface-membrane expression. In contrast, co-expression of stac3 variant W[284]S with $Ca_V1.1_{BBS}$ resulted in sharply diminished QD labeling visualized via confocal imaging (Figure

3.5F). Population analysis using flow cytometric analysis further confirms this result (p < 1E-5) (Figure 3.5G and Figure 3.5K). Likewise, analysis of two additional disease-associated stac3 variants, L[111]Δ (p < 1E-5) and K[288]* (p < 1E-5), revealed variably diminished channel surface-membrane trafficking as evident from reduced $\phi_{\max}$ (Figure 3.5K). Quantitatively, if the binding of stac3 to $\mathrm{Ca_V1.1_{BBS}}$ genuinely underlies the enhancement in channel surface-membrane trafficking, then this functional increase will follow a Langmuir function with the binding affinity of the stac-channel interaction as follows,

$$\phi_{\max}^{\text{stac3}} = \phi_{\max}^{\text{baseline}} + \varphi_{stac3} \cdot \frac{K_a}{K_a + \Lambda} \tag{2.19}$$

where φ_{stac3} and Λ are constants and $\phi_{\max}^{\text{stac3}}$ and $\phi_{\max}^{\text{baseline}}$ represent the saturating surface-membrane trafficking limit in the presence and absence of stac3 respectively (as described in Chapter 2). For stac3 variants, we assume that their relative binding affinity for the $\mathrm{Ca_V1.1}$ CI deduced from FRET two-hybrid binding assays ($K_{\mathrm{a,EFF}}$) is proportional to that for the holochannel interface (K_{a}). This theoretical framework for channel trafficking mirrors individually Transformed Langmuir (iTL) analysis previously developed to deduce binding interfaces critical for channel gating (Ben Johny et al., 2013). Plotting the experimentally determined saturating surface-membrane trafficking ratio $\phi_{\max}$ versus the relative $\mathrm{Ca_V1.1}$ CI binding affinities ($K_{\mathrm{d,EFF}}$) for the stac3 variants reveals the predicted Langmuir relationship (Figure 3.5I). These results demonstrate that stac3 binding to $\mathrm{Ca_V1.1}$ promotes plasmalemmal trafficking and myopathy-associated stac variants exhibit weakened trafficking resulting from disrupted binding to the $\mathrm{Ca_V1.1}$ CT.

Given that both CaM and stac3 independently enhance surface-membrane trafficking of $\mathrm{Ca_V1.1}$, we next investigated whether CaM might rescue the defects in trafficking associated with myopathy-associated stac3. Consequently, we assessed surface-membrane trafficking of $\mathrm{Ca_V1.1_{BBS}}$ in the presence of both stac3 W[284]S and $\mathrm{CaM_{WT}}$. Confocal imaging showed a marked increase in QD labeling (Figure 3.5H) and flow-cytometry confirms this partial rescue at a population level ($p < 1E\text{-}5$) (Figure 3.5I). Similar analysis with other myopathy-associated stac3 variants (L[111]Δ and K[288]*) further confirmed the partial rescue of $Ca_V1.1_{BBS}$ trafficking when CaM_{WT} is coexpressed ($p < 1E\text{-}5$ for both variants) (Figure 3.5K). Intriguingly, the net magnitude of CaM-dependent enhancement in $Ca_V1.1$ surface-membrane trafficking is similar in the presence of all stac3 variants irrespective of their binding affinities (Figure 3.6). These results suggest that the CaM effect on channel trafficking is independent of stac consistent with the two regulatory proteins utilizing distinct binding interfaces (Figure 3.6). These results also suggest that CaM-delivery to $Ca_V1.1$ furnishes an orthogonal strategy for rescue of functional defects resulting from myopathy-associated mutations in stac3. Moreover, $Ca_V1.1$ CT represents a prime interface for screening small-molecules that promote $Ca_V1.1$ trafficking and function.

Small-molecule modulators reverse myopathy-associated $Ca_V1.1$ trafficking defects – Recently, pharmacological chaperones have emerged as a promising strategy to rescue surface-membrane trafficking deficits observed in a variety of genetic disorders involving both G-protein coupled receptors (Beerepoot et al., 2017) and ion channels such as CFTR (cystic fibrosis transmembrane conductance regulator) associated with cystic fibrosis (Hanrahan et al., 2013), K_{ATP} channels associated with congenital hyperinsulinism of infancy (Martin et al., 2013), and $Na_V1.5$ channels associated with Brugada syndrome (Moreau et al., 2012; Valdivia et al., 2004). In many of these cases, small molecule modulators that alter channel gating may offer a dual-purpose as chaperones by stabilizing key channel conformations. Moreover, as Ca^{2+}-influx through $Ca_V1.1$ channels is not necessary to trigger muscle contraction, we reasoned that clinically-relevant small-molecule Ca_V1 antagonists, that traditionally block Ca^{2+}-influx, may be repurposed to reverse trafficking defects of $Ca_V1.1$ observed in the presence of myopathy-associated mutant stac3 (Figure 3.7A). To evaluate this possibility, bungarotoxin-labeling assay and flow-cytometric analysis was used to quantify drug-induced changes in $Ca_V1.1$ trafficking co-expressed with mutant stac3 W[284]S, the most prevalent myopathy-associated stac variant, and $\alpha_2\delta$ and β_{1A} auxiliary subunits.

We tested three L-type Ca^{2+}-channel modulators, nifedipine, diltiazem, and verapamil (Figure 3.7B, cyan bars), as well as two Na channel modulators, mexiletine and ranolazine (Figure 3.7B, blue bars), clinically-approved for various cardiovascular conditions at two concentrations reflecting typical low and high therapeutic plasma concentrations. Remarkably, amongst Ca_V channel modulators, incubation with verapamil resulted in ~40% recovery of $Ca_V1.1$ trafficking (Figure 3.7B) at low (>60%) drug concentration and ~67% recovery at high (> 80%) drug concentration. Diltiazem also increased channel trafficking by ~34% at high (> 80%) drug concentration. By contrast, incubation with nifedipine, mexiletine, and ranolazine resulted in minimal change (<10%) in the saturating fraction of surface-membrane channels (ϕ_{max}) (Figure 3.7B). Of note, in all five conditions, the total GFP fluorescence remained the same suggesting that the increase in the fraction of surface-membrane channels (ϕ_{max}) observed in the presence of verapamil and diltiazem reflects genuine potentiation of channel plasmalemmal trafficking. Verapamil application increased $Ca_V1.1$ trafficking in the absence of stac3 by approximately 2-fold (Figure 3.7B) but only increased channel trafficking in the presence of CaM and stac3 by 24% and 33% respectively (Figure 3.7C).

We also verified the functionality of these channels electrophysiologically. HEK293 transfected with $Ca_V1.1$ and stac3 W[284]S incubated overnight with 0.5 μM verapamil displayed robust ionic currents (Figure 3.7D) and large gating currents (Figure 3.7E) comparable to $stac3_{WT}$ (Figure 3.7F-G) following acute wash off of verapamil. To probe whether drug-mediated enhancement in trafficking is reversible, we incubated $Ca_V1.1$ co-transfected with stac3 W[284]S in verapamil for 24 h, and subsequently washed off the drug for 24 h. Intriguingly, while cells continually incubated in drug showed ~30% increase in trafficking (Figure 3.7H; $p < 1E\text{-}5$), wash off of verapamil saw a reversal of channel trafficking (Figure 3.7H; $p < 1E\text{-}5$). All together, these results reveal plausible therapeutic potential for diltiazem and verapamil or related drugs as well as highlight the utility of the bungarotoxin-labeling assay for small-molecule screens of pharmacological chaperones.

DISCUSSION

$Ca_V1.1$ has often appeared atypical amongst L-type channels, with seemingly poor conservation of regulatory mechanisms, and idiosyncratic requirements for membrane expression manifesting as a loss of function in heterologous systems. While related $Ca_V1/2$ channels exhibit robust plasmalemmal trafficking with β and $\alpha_2\delta$ subunits, additional components such as cytosolic stac3 and the transmembrane γ_1 subunit, are thought obligatory for $Ca_V1.1$ currents in heterologous systems (Bannister and Beam, 2013; Polster et al., 2016; Polster et al., 2015; Tuluc et al., 2009). How do these modifications at disparate channel interfaces influence trafficking?

Our results point to a unified trafficking scheme (Figure 3.8) with the requirements for $Ca_V1.1$ trafficking paralleling those for related Ca_V channels (Fang and Colecraft, 2011). Specifically, the β-subunit is a dominant effector necessary for $Ca_V1.1$ plasmalemmal trafficking (Figure 3.8A). This requirement of β-subunits for $Ca_V1.1$ trafficking fits well with reduced channel expression and diminished tetrad formation observed in β_{1A}-knockout mice (Schredelseker et al., 2005). Upon binding the β-subunit, $Ca_V1.1$ however exhibits only low baseline trafficking (Figure 3.8B). The binding of either CaM or stac3 alone leads to only a partial enhancement in membrane trafficking (Figure 3.8C-D). Finally, the binding of both CaM and stac3 to the $Ca_V1.1$ CT yields a supra-linear increase in membrane trafficking (Figure 3.8E). Interestingly, complete removal of the CT results in a basal increase in channel trafficking suggesting that there may be retention motifs encoded within the CT that are masked upon the interaction of either stac3 or CaM (Figure 3.2J). This simplified scheme captures the experimentally-observed effects of stac3 and CaM on $\mathrm{Ca_V}1.1$ and provides a platform for other indirect mechanisms to be assessed.

Mechanistically, the $\mathrm{Ca_V}1.1$ CT is a critical determinant for surface-membrane trafficking by harboring both CaM and stac3, a finding that resonates with early studies that identified a vital role for this domain in triad localization (Flucher et al., 2000). As CaM is enriched in the triad via transient association with cytoplasmic loops of RyR1 (Mochca et al., 2001; Sencer et al., 2001; Xiong et al., 2002), its weak binding to $\mathrm{Ca_V}1.1$ may promote co-localization of the channels at the tubular or surface membranes (Rodney and Schneider, 2003). Recurrent large-amplitude Ca^{2+}-transients in the triadic space may further reinforce this localization. Indeed, the role of Ca^{2+}/CaM in mediating activity-dependent trafficking has emerged as a pervasive theme in $\mathrm{Ca_V}$ channel physiology, yet the precise motifs that orchestrate this phenomenon are yet to be elucidated (Hall et al., 2013; Tseng et al., 2017; Wang et al., 2007). Similarly, our results indicate that stac3 potentiates $\mathrm{Ca_V}1.1$ trafficking also via interaction with the CT. Even so, CaM and stac3 likely act through distinct sites as their combination supra-additively enhance channel trafficking. Analysis of stac3$^{-/-}$ zebrafish and mouse skeletal myotubes revealed a partial reduction of $\mathrm{Ca_V}1.1$ at the triad leading to incomplete tetrads and a loss of EC coupling (Linsley et al., 2017a; Linsley et al., 2017b; Polster et al., 2015). The magnitude of reduction varied between the two models suggest that other regulators such as CaM may play a role in channel trafficking in the muscle. As various stac isoforms promote trafficking of $\mathrm{Ca_V}1.2$ and $\mathrm{Ca_V}3$ (Rzhepetskyy et al., 2016), stac may be a shared modulator across the $\mathrm{Ca_V}$ family (Weiss and Zamponi, 2017). Our quantitative framework and flow-cytometric analysis of external-epitope labeling may delineate vital signals for membrane trafficking of $\mathrm{Ca_V}$ channels in skeletal muscle and other native cell types.

Furthermore, stac3 co-expression upregulates the baseline P_O of $\mathrm{Ca_V}1.1$ to the same extent as CaM depending on the CI module (Figure 3.4O). Interestingly, in skeletal myotubes, homozygous stac3 knockout (Linsley et al., 2017a; Polster et al., 2015) and $\mathrm{Ca_V}1.1$ mutants with weakened CaM binding (Stroffekova, 2011) lead to a dramatic loss of EC coupling despite the presence of gating charge movements. Thus, robust EC coupling may require a permissive $\mathrm{Ca_V}1.1$ CT conformation along with that for the II-III loop (Tanabe et al., 1990a). Synthesizing a general framework of $\mathrm{Ca_V}$ modulation by CaM and stac is an exciting frontier and the ability to express $\mathrm{Ca_V}1.1$ in heterologous systems under a wide-range of conditions facilitates this pursuit and will be further discussed in Chapter 4.

Pathophysiologically, our analysis reveals that disease-associated stac3 variants weaken binding to the CT resulting in variably diminished $\mathrm{Ca_V}1.1$ surface-membrane trafficking, highlighting potential pathogenic mechanisms. Indeed, reconstitution of myopathy-associated mutant stac3 (W[284]S) in $\mathrm{stac3^{-/-}}$ knockout zebrafish and mouse models led to diminished trafficking, triadic organization, and activity of $\mathrm{Ca_V}1.1$ resulting in marked loss of EC coupling (Linsley et al., 2017a; Linsley et al., 2017b; Polster et al., 2016). As $\mathrm{Ca^{2+}}$-influx through $\mathrm{Ca_V}$ channels is not necessary for EC coupling (Dayal et al., 2017), our findings suggest that diltiazem and verapamil, traditionally used as $\mathrm{Ca_V}$ channel antagonists, may be repurposed as pharmacological chaperones that rescue trafficking defects for stac3-associated congenital myopathies, although this effect is contingent upon continual exposure to the drug. Diltiazem and verapamil are clinically prescribed for various diseases including hypertension, arrhythmia, angina, and cluster headaches. Side-effects presented include headaches, hypotension, gingival hyperplasia, constipation, and edema. Consequently, we show that low therapeutic plasma concentration is sufficient for strikingly enhanced surface-membrane trafficking of Ca$_V$1.1 and gating charge movement remains unimpaired. Indeed, similar pharmacological chaperones have emerged as a potential therapeutic avenue for rescue of trafficking deficits associated with cystic fibrosis (Hanrahan et al., 2013), congenital hyperinsulinism of infancy (Martin et al., 2013), and Brugada syndrome (Moreau et al., 2012; Valdivia et al., 2004).

These results highlight the utility of reconstituted Ca$_V$1.1 channels in HEK293 cells as a simplified platform to distinguish distinct regulatory effects of individual triadic signaling molecules, and as an attractive venue for high-throughput screens of small molecules that modulate Ca$_V$ trafficking. Our findings illustrate that Ca$_V$1.1 trafficking and gating are tuned by redundant signaling mechanisms and shed light upon pathophysiological mechanisms and strategies for pharmacological intervention of stac3-associated congenital myopathies.

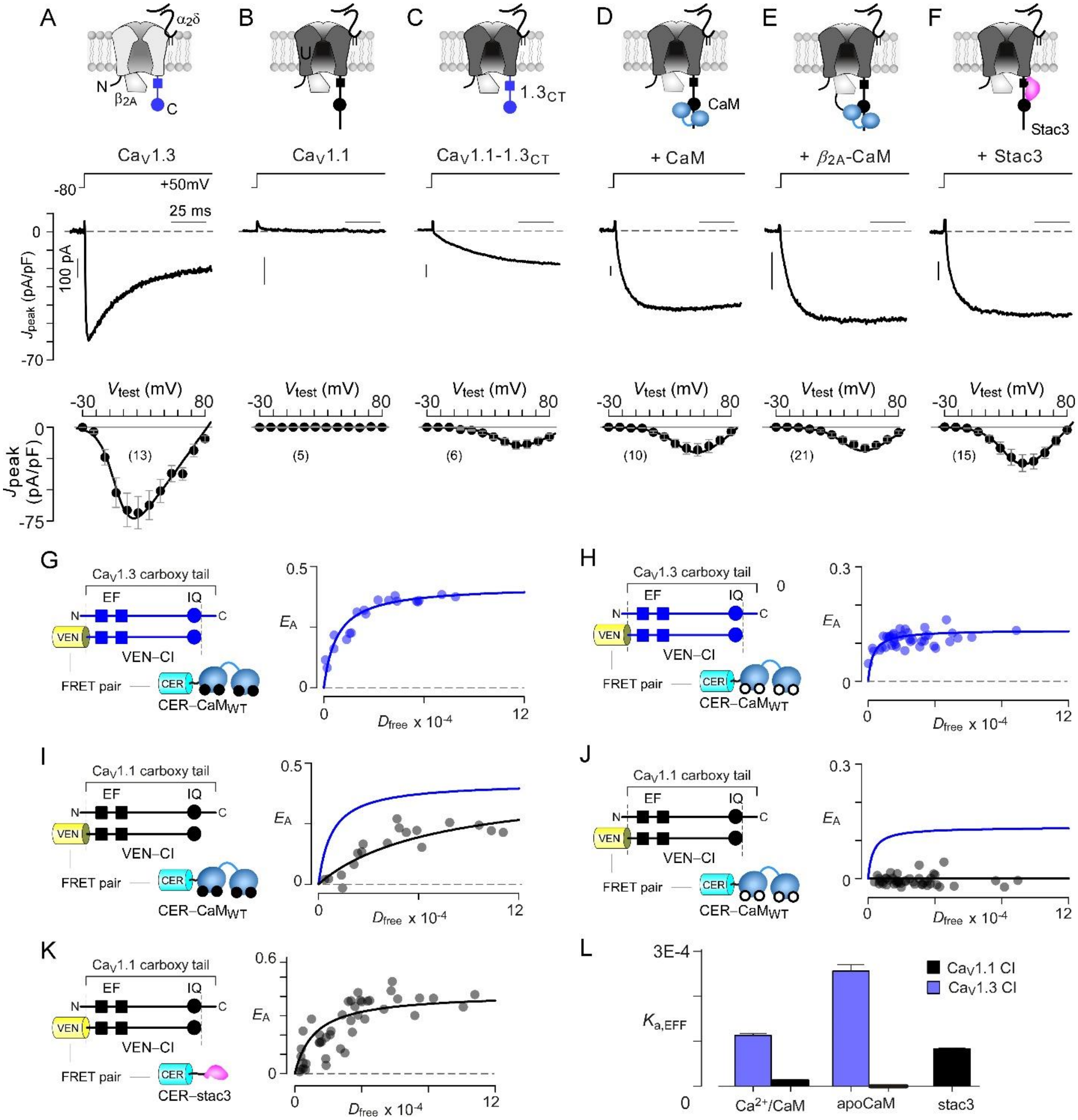

Figure 3.1. Robust expression of Ca$_V$1.1 is dependent on its carboxy-tail and binding to CaM and stac3.

(A) Ca$_V$1.3 with β$_{2a}$ and α$_2$δ auxiliary subunits exhibit robust currents in HEK293 cells. Top, cartoon depicts the Ca$_V$1.3 pore-forming α$_1$ subunit with auxiliary subunits co-transfected. Middle, exemplar current traces in response to a voltage-step protocol from -80 mV to +50mV. Gray dashed line, baseline of 0 pA. Bottom, population data for current density-voltage relationship from -30 to +80 mV in 10 mV increments for indicated number of cells (*n*). Gray solid line, baseline of 0 pA.

(B) Ca$_V$1.1 with auxiliary subunits do not exhibit functional expression. Format as in panel A.

(C) Chimeric Ca$_V$1.1 with the Ca$_V$1.3 CT partially rescues functional expression. Format as in panel A.

(D-E) Restoration of CaM binding to $Ca_V1.1$ through overexpression of CaM or direct linkage to the auxiliary β_{2A}-subunit produces robust functional expression. Format as in panel A.
(F) Co-expression of stac3 also elicts robust Ca^{2+} currents through $Ca_V1.1$. Format as in panel A.
(G) Left, schematic show FRET binding pairs, Cer-CaM_{WT} and Ven-$Ca_V1.3$ CI. Here, the CI module consists of the dual vestigial EF hand, pre-IQ and IQ segments of carboxy-tail. Right, the CI region of $Ca_V1.3$ binds well to Ca^{2+}/CaM ($K_{d,EFF}$ = 8000 D_{free} units ~ 260 nM). FRET efficiency (E_A) is plotted as a function of donor-fluorophore tagged molecule (D_{free}) concentration (right). Gray dashed line indicates baseline for no binding.
(H) $Ca_V1.3$ CI binds well to apoCaM ($K_{d,EFF}$ = 3000 D_{free} units ~ 98 nM). Format as in panel G.
(I) The CI region of $Ca_V1.1$ binds weakly to Ca^{2+}/CaM. Format as in panel d ($K_{d,EFF}$ = 70000 D_{free} units ~ 2.3 μM). Format as in panel G.
(J) $Ca_V1.1$ CI also binds poorly to apoCaM. Format as in panel G.
(K) Stac3 binds to the CI region of $Ca_V1.1$ ($K_{d,EFF}$ ~ 12000 D_{free} units ~ 400 nM). Format as in panel G.
(L) Bar graph summarizes binding affinities from FRET curves, average ± SEM.

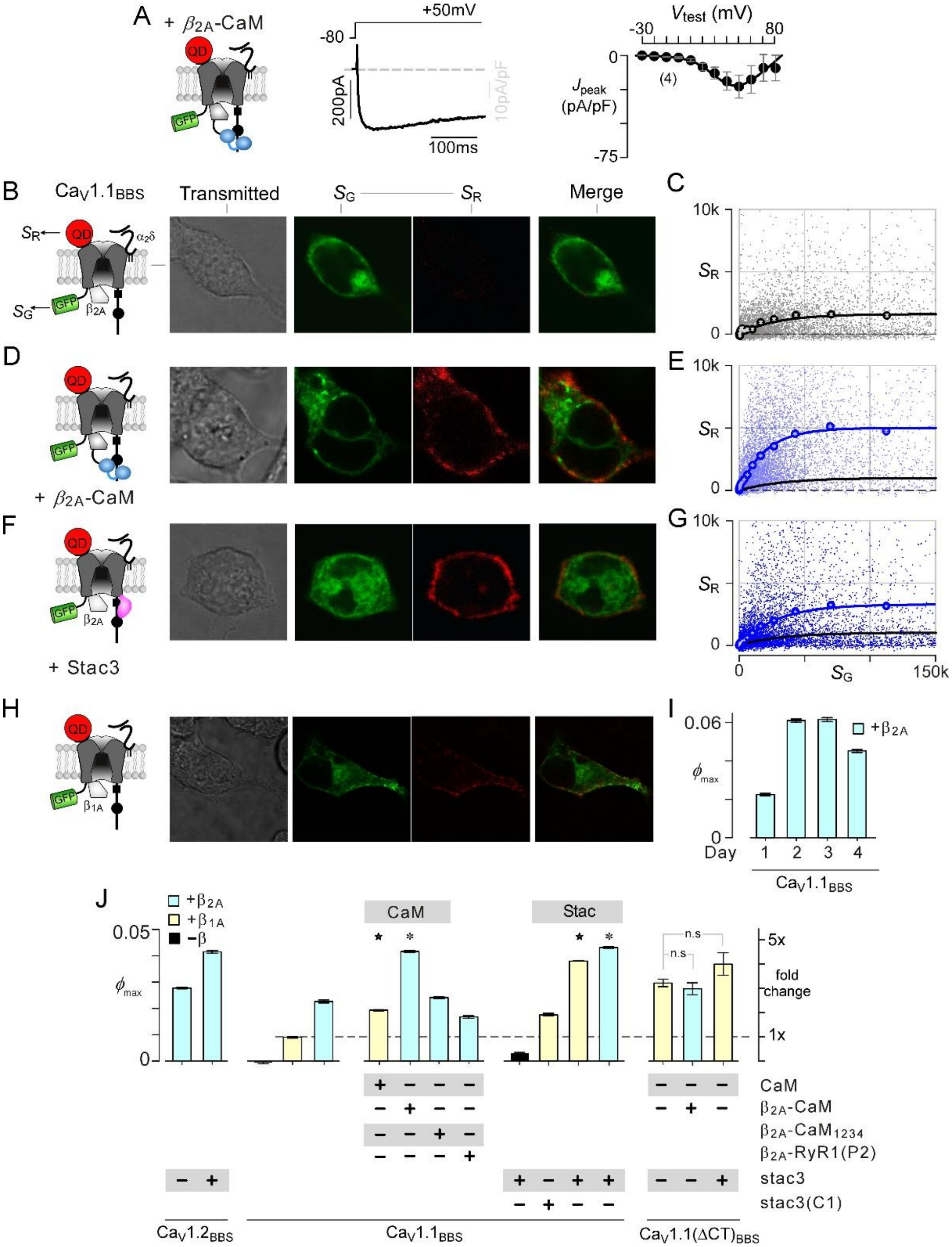

Figure 3.2. CaV1.1 surface-membrane trafficking is enhanced by CaM and stac3.

(A) Both CaV1.1 and CaV1.1BBS yield similar Ca^{2+} currents when co-expressed with β_{2a}-CaM. Left, cartoon of CaV1.1BBS transfected with $\alpha_2\delta$ subunit and β_{2a}-CaM. Middle, exemplar trace of current elicited with a +50 mV voltage-step. Right, J_{peak} (mean ± SEM) computed from indicated number of cells (n). Format as in Figure 3.1A.

(B) CaV1.1 in the presence of $\alpha_2\delta$ and β_{2A} auxiliary subunits traffics poorly and exhibits weak extracellular labeling. Left, schematic shows external-epitope labeling of GFP-tagged CaV1.1 engineered with an α-bungarotoxin binding site (CaV1.1BBS) in the presence of $\alpha_2\delta$ and β_{2A} auxiliary subunits. Here the external epitope is α-bungarotoxin conjugated to QD. Right, transmitted-light, intracellular GFP (S_G), extracellular QD (S_R), and merged images for transfected and labelled cells were collected by confocal microscopy.

(C) Flow-cytometric analysis confirms weak surface-membrane expression for Ca$_V$1.1$_{BBS}$ with α2δ and β_{2A} auxiliary subunits co-transfected. QD fluorescence, S_R, is plotted as a function of GFP fluorescence, S_G. Each dot represents one cell. Black dashed line indicates no extracellular labeling (S_R = 0). Black circles and fit denote binned data for QD and GFP fluorescence fitted a single-exponential function.

(D-E) Confocal imaging and flow cytometry experiment show that co-transfection of β_{2a}-CaM augments Ca$_V$1.1 surface-membrane labeling. $\alpha_2\delta$ was co-transfected. Format as in panels a and b. Blue circles and fit in panel d correspond to binned data while black fit is reproduced from panel b to facilitate comparison with baseline Ca$_V$1.1 trafficking.

(F-G) Confocal imaging and flow-cytometry of Ca$_V$1.1$_{BBS}$ co-transfected with stac3, β_{2A} and $\alpha_2\delta$ subunits confirms enhanced surface-membrane trafficking of Ca$_V$1.1 when bound to stac3. Format as in panels a-b.

(H) Ca$_V$1.1$_{BBS}$ co-expressed with only auxiliary β_{1A} and $\alpha_2\delta$ subunits traffic to the plasma membrane. Format as in panel B.

(I) Bar graph shows surface-membrane trafficking limit ϕ_{max} for Ca$_V$1.1$_{BBS}$ with β_{1A} and $\alpha_2\delta$ subunits increases and stabilizes after multiple days of transient transfection.

(J) Bar graph summarizes saturating surface-membrane trafficking limit ϕ_{max}, proportional to the maximal fraction of Ca$_V$1.1 trafficked to the plasma-membrane, under various conditions as indicated. ★ denotes p<1E-5 with Welch's T-test compared to Ca$_V$1.1 expressed with β_{1A}. * indicates p<1E-5 for Ca$_V$1.1 expressed with β_{2A}.

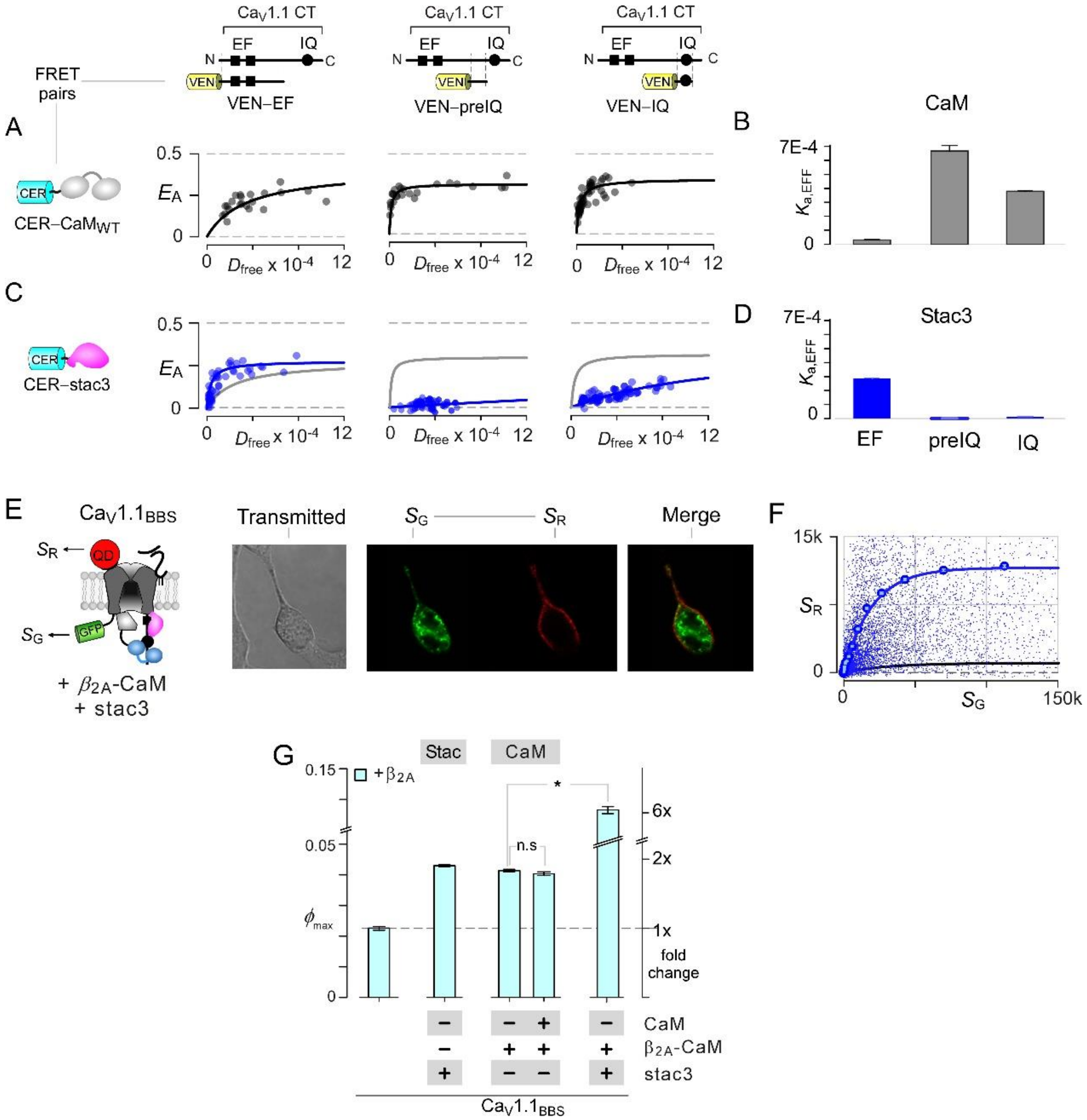

Figure 3.3. CaM and stac3 bind to distinct sites on the CT and exert independent trafficking effects. (A) FRET binding of Ca^{2+}/CaM with EF hands (left), pre-IQ (middle), and IQ domain (right) shows weak binding for EF hands and strong binding for pre-IQ and IQ domains.

(B) Bar graph summary of binding affinities from panel A.

(C-D) Stac3 binds preferentially to EF hands. Format as in panels A and B.

(E-F) Coexpression of CaM and stac3 results in a distinct extracellular labeling and supralinear increase of channels on the membrane. Format as in Figure 3.2B-C.

(G) Bar graph summarizing ϕ_{max} for CaM and stac3 separately as well as together. Expressing CaM and β_{2A}-CaM does not result in a large change of ϕ_{max} in comparison to a 6-fold increase from coexpressing CaM and stac3. * indicates $p<1E-5$.

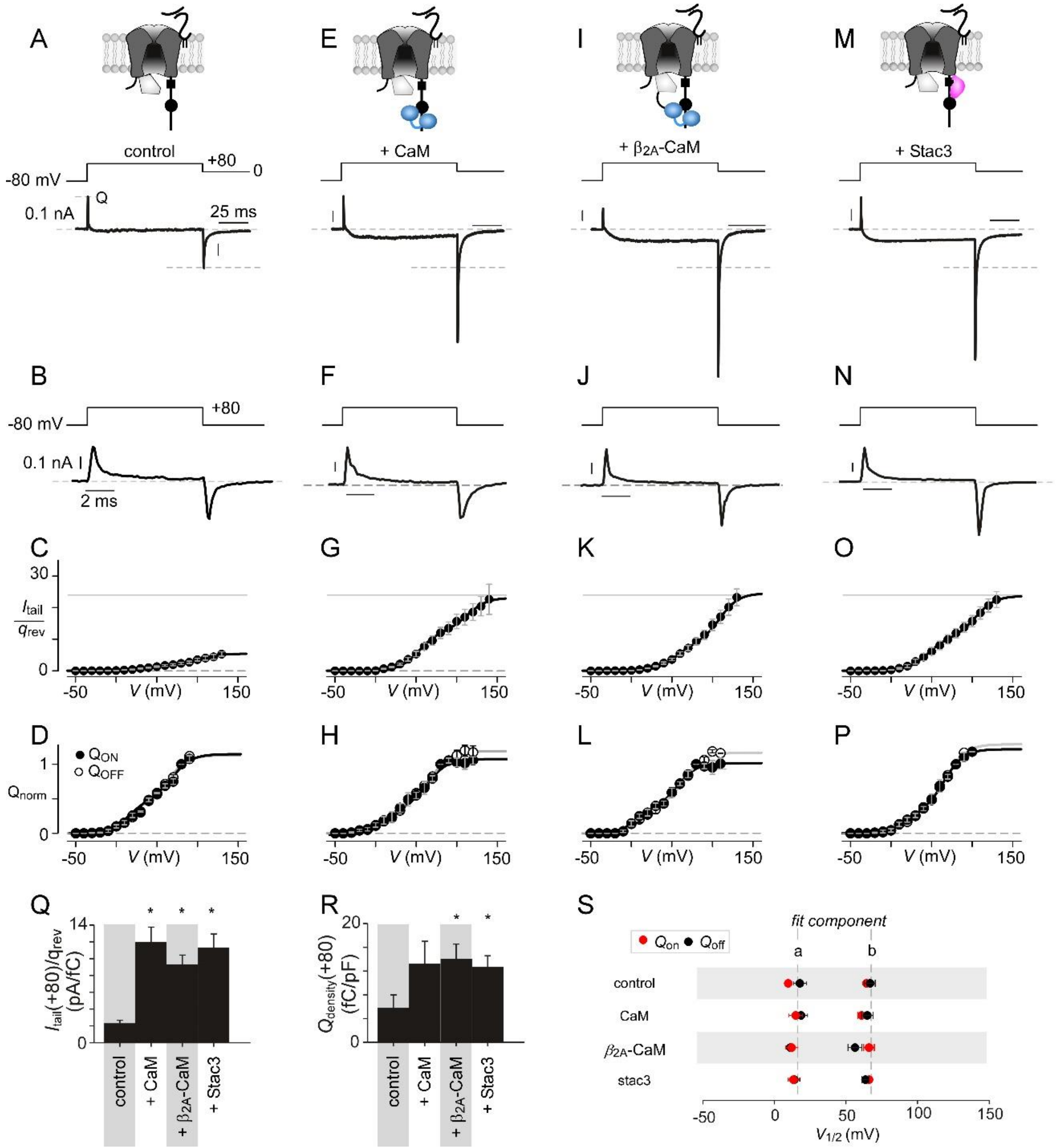

Figure 3.4. P_{O} of Ca$_{\mathrm{V}}$1.1 is increased with CaM and stac3.

(A) Ca$_{\mathrm{V}}$1.1 with only its auxiliary β_{2A} and $\alpha_2\delta$ subunits elicit small tail current (I_{tail}) despite large gating charge movement indicating a low-PO for these channels at baseline. Top, cartoon depicts Ca$_{\mathrm{V}}$1.1 α_1 subunit bound to auxiliary β_{2A} and $\alpha_2\delta$ subunits in HEK293 cells Bottom, exemplar currents elicited in response to voltage step-depolarization from -80 mV to +80 mV show large gating-charge movement at the reversal potential (q_{rev}) and I_{tail} evoked upon repolarization to 0 mV.

(B) Exemplar current trace for gating charge movement after pore block with Cd^{2+}/La^{3+} with voltage step-depolarization from -80 mV to +80 mV and back to -80 mV. Trace shows equivalent gating charge movement into the open conformation (Q_{ON}) and gating charge movement into the closed conformation (Q_{OFF}).

(C) Population data of $I_{\mathrm{tail}}/q_{\mathrm{rev}}$ reveals low P_{O}. Here, I_{tail} evoked in response to a voltage-step family with varying pre-pulse potentials are normalized by the gating charge movement at the reversal potential, q_{rev}. This ratio ($I_{\mathrm{tail}}/q_{\mathrm{rev}}$) is proportional to P_{O} of the channel.
(D) Population data of normalized Q_{OFF} to Q_{ON} confirms equivalent charge movement and also the reliability for approximating P_{O}.
(E-H) Overexpression of CaM enhances the ratio of $I_{\mathrm{tail}} / q_{\mathrm{rev}}$ arguing that CaM enhances baseline P_{O} of $\mathrm{Ca_V}1.1$. Format as in panels a-d. (I-L) Similarly, localized-delivery of CaM via fusion to the β_{2A}-subunit enhances I_{tail} despite similar q_{rev}. Format as in panel A-D.
(M-P) Co-expression of stac3 also increases $I_{\mathrm{tail}} / q_{\mathrm{rev}}$ by approximately 5-fold, which is comparative to CaM. Format as in panel A-D.
(Q) Population data of I_{tail} (+80 mV) / q_{rev} shows significant increase of P_{O} with the addition of CaM or stac3. * for $p<0.01$.
(R) Population data of Q_{density} (+80 mV) confirms increase of channels on the membrane with the addition of CaM or stac3. * for $p<0.05$.
(S) The Q-V curves (Figure 3.4D, H, L, P) were fit with double Boltzmann relations. Plot compares half-activation potentials for the two components ($V_{1/2,\mathrm{a}}$ and $V_{1/2,\mathrm{b}}$) for various conditions. For each component and across all conditions, we did not observe a statistically significant difference between Q_{on} (red) and Q_{off} (black) ($p > 0.15$). Moreover, no statistically significant differences were observed for $V_{1/2,\mathrm{a}}$ and $V_{1/2,\mathrm{b}}$ values in the presence of different modulators ($p > 0.1$). These results suggest that both Stac3 and CaM spare voltage-sensor movement. The profound difference in saturating $I_{\mathrm{tail}}/Q_{\mathrm{rev}}$ in the presence of CaM and Stac3 would indicate that these regulatory proteins alter the coupling between voltage-sensor movement and channel pore domain.

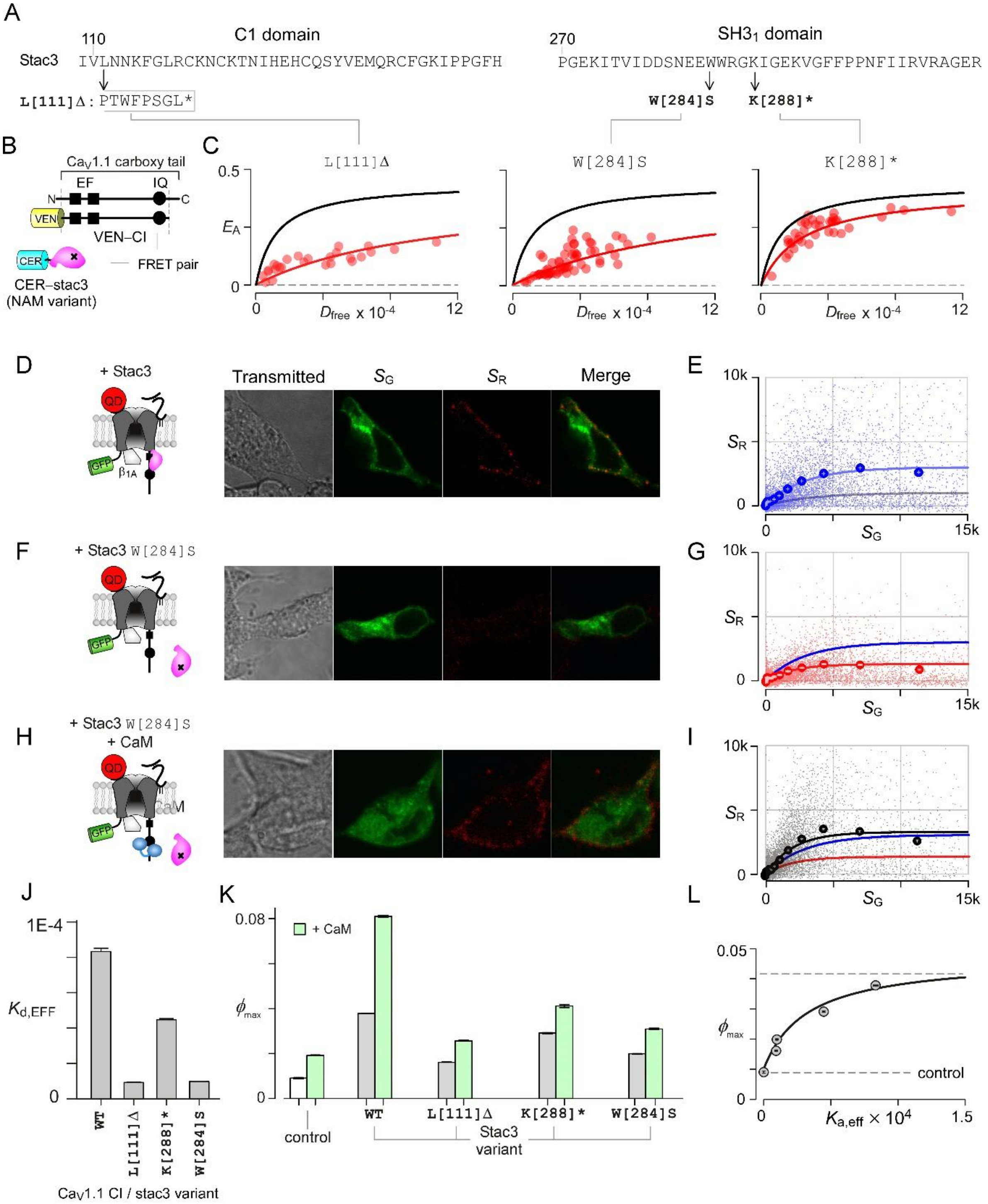

Figure 3.5. Myopathic stac3 mutations reduce binding to the CT and surface membrane trafficking.

(A) Amino acid sequence for stac3 mutations in both the C1 and first SH3 domain ($SH3_1$).

(B) Schematic shows fluorophore tagged FRET pairs, Ven-CI of $Ca_V1.1$ with Cer-tagged stac3 variants.

(C) Myopathy-associated stac3 variants weaken binding to $Ca_V1.1$ CI. Left, intron insert results in a frameshift and truncation of SH3 domains (L[111]Δ) dramatically reduces stac3 binding to

$Ca_V1.1$ CI. Middle, a point mutation in the 1st SH3 domain (W[284]S) strongly reduces stac3 binding. Right, disease-associated stac3 variant with a nonsense mutation in the 2nd SH3 domain (K[288]*) moderately weakens binding to $Ca_V1.1$.

(D) Stac3 strongly enhances $Ca_V1.1$ surface-membrane trafficking in the presence of β_{1A} and α2δ subunits, as demonstrated by detectible BTX-labeling in exemplar confocal images. Format as in Figure 3.2B.

(E) Flow cytometric analysis confirms high expression of $Ca_V1.1$ when bound to stac3. Format as Figure 3.2B.

(F-G) Co-expression of myopathy-associated stac3 mutant (W[284]S) results in only modest enhancement in $Ca_V1.1$ surface-membrane trafficking as illustrated by confocal imaging and flow cytometry. Format as in panels D and E respectively.

(H-I) Co-expression of CaM with mutant stac3 (W[284]S) results a large increase of $Ca_V1.1$ surface membrane trafficking comparable to that with wildtype stac3. Format as in panels D and E.

(J) Bar graph summarizes binding affinities of stac variants to $Ca_V1.1$ CI, average ± SEM.

(K) Bar graph summarizes the saturating surface-membrane trafficking limit $\phi_{\max}$ of $Ca_V1.1$ in the presence of myopathy-associated mutant stac3 and corresponding rescue with CaM. Stac3 mutations that weaken binding to $Ca_V1.1$ CT also reduces surface-membrane trafficking (gray bar) and may be partially rescued with CaM co-expression (green bar). Control (white) bar is $Ca_V1.1$ expressed with basic auxiliary subunits $\alpha_2\delta$ and β_{1A} for comparison.

(L) For all stac3 variants, plotting $\phi_{\max}$ versus the association constant ($K_{a,EFF} = 1 / K_{d,EFF}$; panel C) for the binding of mutant stac3 to $Ca_V1.1$ CI module reveals a Langmuir relationship suggesting that the binding of stac3 is a key determinant for Cav1.1 surface-membrane trafficking. Dashed gray lines are the $\phi_{\max}$ for with (upper) and without (lower) $stac3_{WT}$.

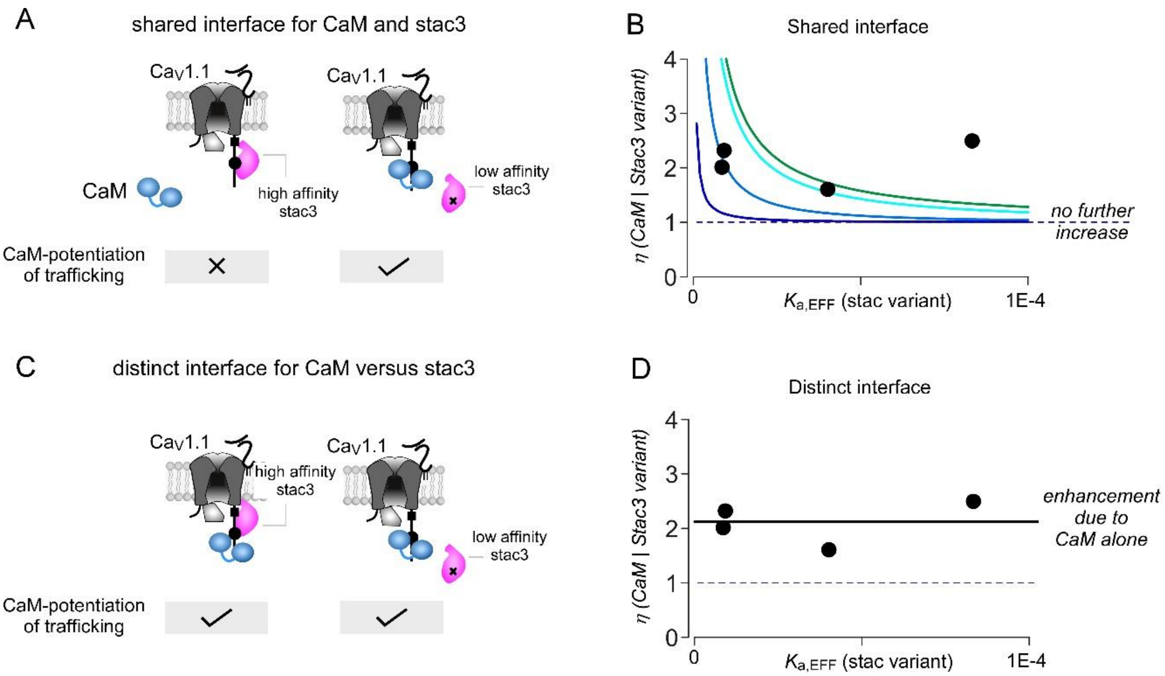

Figure 3.6. Extended analysis of CaM-dependent enhancement in Ca$_V$1.1 plasmalemmal trafficking in the presence of stac3 variants suggests distinct binding interfaces.

(A) If CaM and stac3 share a common interface, then in the presence of high-affinity stac3 variants, CaM is incapable of reaching this interface and the effective enhancement in trafficking due to CaM would be minimal. However, if stac3 variants have a low affinity, then the shared interface is unoccupied and available for CaM.

(B) Simulation shows CaM-dependent enhancement in Ca$_V$1.1 trafficking in the presence of various stac3 variants as a function of stac3 binding association constant for Ca$_V$1.1 CI ($K_{\mathrm{a,EFF}}$ (stac variant)). Specifically,

$$\eta\,(\,\mathrm{CaM} \mid \mathrm{stac3variant}\,) =$$
$$(\,\phi_{\max}(\mathrm{stac3\ variant} + \mathrm{CaM}) - \phi_{\max}(\mathrm{basal})\,)/(\,\phi_{\max}(\mathrm{stac3\ variant}) - \phi_{\max}(\mathrm{basal})\,).$$

Dashed line corresponds to no enhancement in plasmalemmal trafficking with CaM. Blue curves are simulations obtained at low levels of CaM, while cyan and green are relations at high levels of CaM. Experimental data shows that η (black dots) is relatively constant as a function of $K_{\mathrm{a,\,EFF}}$ (stac variant).

(C) If CaM and stac3 utilize distinct interfaces, then CaM will be able to enhance Ca$_V$1.1 trafficking irrespective of stac3 binding status. Moreover, in this scenario the magnitude of CaM-dependent enhancement of Ca$_V$1.1 trafficking in the presence of stac3 variants should equal the net increase in Ca$_V$1.1 trafficking by CaM in the absence of stac3.

(D) Black line shows expected outcome for η (CaM | stac3 variant) if CaM and stac3 use distinct interfaces. Reassuringly, the experimentally-determined η values match the predicted relationship suggesting that CaM and stac utilize distinct interfaces to enhance channel trafficking.

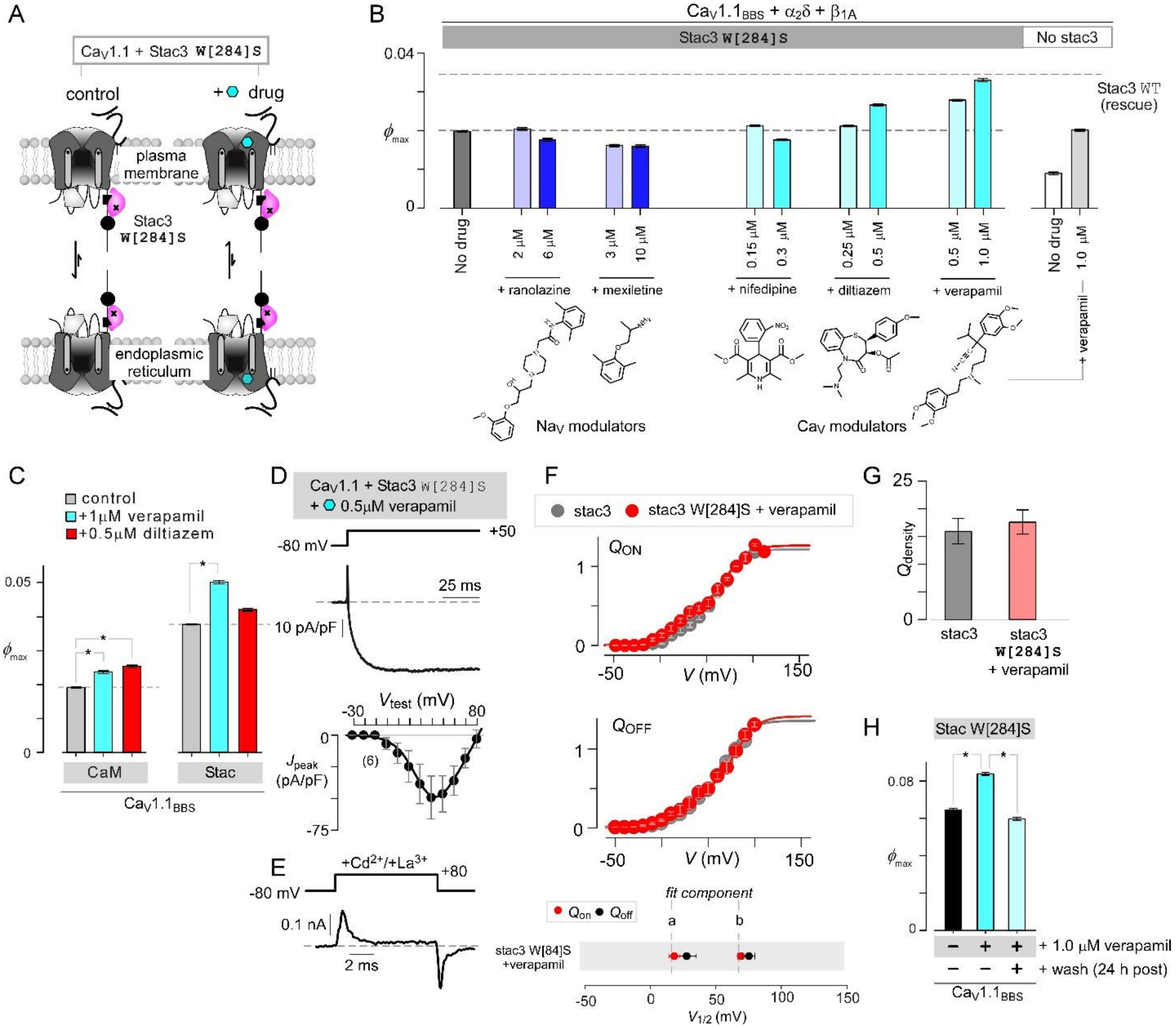

Figure 3.7. Small-molecule modulators partially rescue pathological deficits in CaV1.1 trafficking. (A) Cartoon schematizes potential enhancement of CaV1.1 plasmalemmal trafficking in the presence of potential pharmacological agents. Left, CaV1.1 when bound to myopathy-associated mutant stac3 (W[284]S) and $\alpha_2\delta$ and β_{1A} subunits traffics poorly to the plasma membrane. Right, addition of a small-molecule trafficking modulator may enhance the fraction of surface-membrane channels.

(B) Bar graph summarizes changes in the saturating surface-membrane trafficking limit (ϕ_{max}) of CaV1.1 trafficking following addition of various small-molecule modulators at low and high concentrations. Lower dashed line corresponds to baseline trafficking with myopathic stac3 (W[284]S) (gray) while upper dashed line corresponds to CaV1.1 trafficking with wildtype stac3. Both diltiazem and verapamil markedly enhanced ϕ_{max} while dihydropyridines and Na channel modulators ranolazine and mexiletine did not substantially alter CaV1.1 trafficking. Without stac3, 1 μM verapamil increased CaV1.1 trafficking by approximately 2-fold.

(C) Bar graph summarizing drug effects on CaV1.1 trafficking transfected with CaM_{WT} and stac3_{WT}. Asterisk indicates statistically significant differences ($p < 1\text{E-}6$).

(D) CaV1.1 expressing stac3 W[284]S are functional after incubation with 0.5 μM verapamil. Top, given a voltage step-depolarization from -80 mV to +50 mV, channels produce robust inward current. Bottom, population data of current density-voltage relationship from -30 to +80 mV in 10 mV increments for indicated number of cells (*n*). Gray solid line, baseline of 0 pA.

(E) Gating charge movement of these channels also appear normal after pore block with Cd^{2+}/La^{3+}. Format as in Figure 3.4B.

(F) Population data summarizing Q_{ON} and Q_{OFF} for $stac3_{WT}$ and stac3 W[284]S. Left, Q_{ON} for stac3 W[284]S (red) is overlaid on top of Q_{ON} for $stac3_{WT}$ (gray). Right, Q_{OFF} for stac3 W[284]S (red) is overlaid on top of Q_{OFF} for $stac3_{WT}$ (gray).

(G) Population data summary of maximal $Q_{density}$ for $stac3_{WT}$ and stac3 W[284]S.

(H) Bar graph summarizing $Ca_V1.1$ co-expressed with $stac3_{W[284]S}$ incubated with and without 1.0 µM verapamil for 48 h and with wash after 24 h. Asterisk indicates statistically significant difference ($p < 1E\text{-}6$).

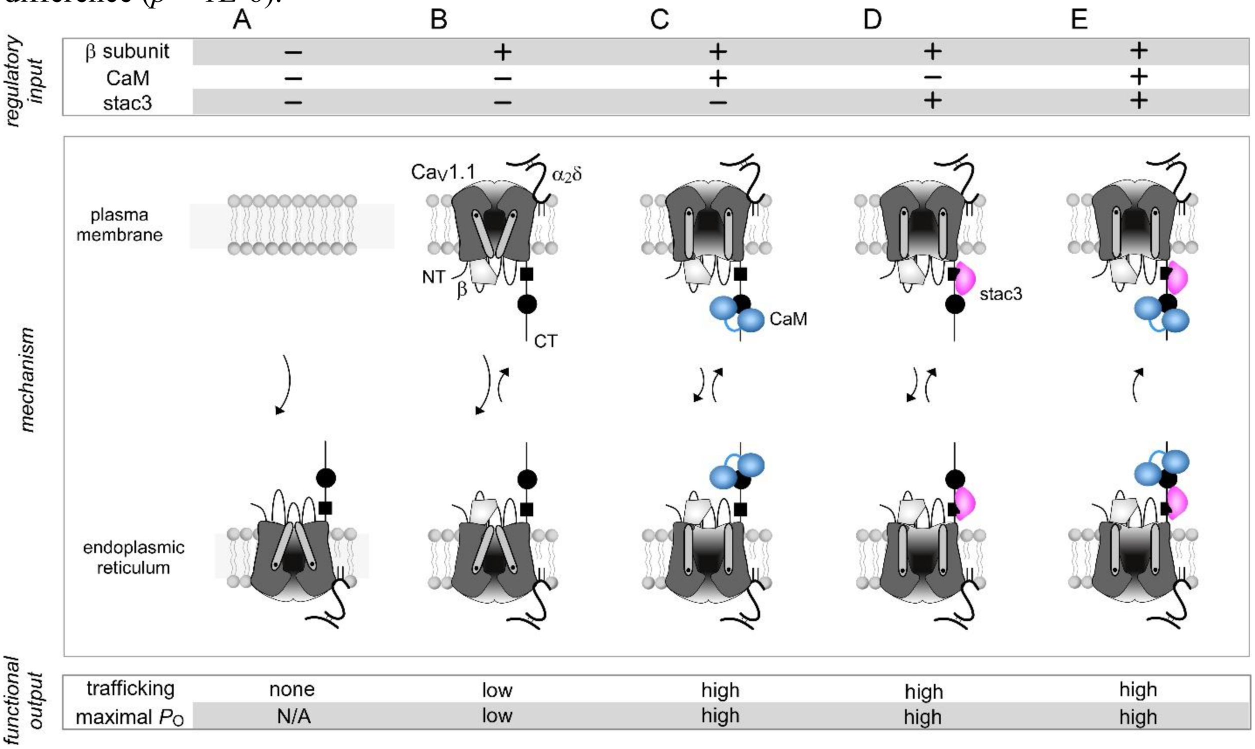

Figure 3.8. Molecular determinants for $Ca_V1.1$ functional expression.

Schematic illustrates a simplified model for the effect of various regulatory protein on $Ca_V1.1$ functional expression. For all panels, top and bottom rows identify the regulatory input and functional outcomes respectively. Middle row schematizes underlying molecular mechanism.

(A) Devoid of a *β* subunit, $Ca_V1.1$ fail to traffic to the surface membrane presumably due to ER retention motifs.

(B) Binding of the *β* subunit enables low basal $Ca_V1.1$ surface-membrane trafficking. Channels at the plasma-membrane feature a low P_O.

(C) CaM enhances $Ca_V1.1$ surface-membrane trafficking. The same CaM also enhances baseline P_O.

(D) Stac3 binding enhances $Ca_V1.1$ surface-membrane trafficking and upregulates baseline P_O.

(E) Binding of CaM and stac allows for high $Ca_V1.1$ trafficking. The channels are presumed to retain a high baseline P_O.

CHAPTER 4

Stac selectively tunes Ca^{2+}-regulation of Ca_V1 ion channels

High-voltage activated calcium (Ca^{2+}) channels (Ca_V1 and Ca_V2) support many vital physiological processes including muscle contraction, neurotransmission, and gene transcription(Berridge et al., 2000; Clapham, 2007; Maier and Bers, 2002). In the past few decades, it has been shown that despite these vastly different physiological roles, Ca_V1 and Ca_V2 possess high sequence homology within an ~150 residue stretch in the carboxy-tail (CT) known as the Ca^{2+}-inactivating (CI) module(Ben-Johny et al., 2015; Findeisen and Minor, 2010). This CI region interacts with a Ca^{2+}-binding protein, calmodulin (CaM), to confer dynamic Ca^{2+}-dependent regulation to Ca_V1 and Ca_V2. Furthermore, misregulation of Ca^{2+} through CaM signaling to the CI has been implicated in cardiac arrhythmias(Limpitikul et al., 2014; Mahajan et al., 2008; Venetucci et al., 2012; Zimmer and Surber, 2008) as well as neurological and neuropsychiatric disorders (Adams and Snutch, 2007; Striessnig et al., 2010; Zamponi, 2016). Subsequently, the challenge arises for how biology tunes CaM-regulation of these structurally similar tail elements to produce diverse cell signals. One way for cells to achieve this is through specialized gene expression patterns. In ventricular myocytes, the Ca_V isoform $Ca_V1.2$ is the predominant channel expressed throughout the cell(Mikami et al., 1989) while in Purkinje neurons, $Ca_V2.1$ is the principal channel expressed(Mintz et al., 1995). Another way to generate diversity in activity is by adding an extra layer of regulatory proteins that tune Ca_V function through interactions with other parts of the channel itself. More recently, SH3 and cysteine rich domain (stac), has been identified as a potential partner for Ca_V(Polster et al., 2015; Suzuki et al., 1996).

In this chapter, we leverage synergistic insights from Ca$_V$ channels and demonstrate that stac selectively suppresses Ca^{2+}-regulation of Ca$_V$1. In depth functional analysis demonstrates that stac attains this selectivity via an allosteric mechanism that exploits a distinct binding site from CaM, as discussed in Chapter 3 for Ca$_V$1.1, to lock Ca$_V$1 into a persistent high open probability (P_O) gating mode. In so doing, we further identified a minimal motif that recapitulates stac modulation of Ca$_V$1 gating. In all, our findings identify a general class of auxiliary proteins that specifically intercept CaM signaling to individual targets, allowing spatial and temporal orchestration of Ca^{2+}-feedback.

RESULTS

Stac selectively suppresses Ca^{2+}-feedback of Ca$_V$1 channels – To contextualize plausible physiological roles of stac, we immunohistochemically assessed the expression and localization of stac isoforms in neurons and cardiac myocytes by using stac1 and stac2 specific antibodies (Figure 4.1A). Staining coronal slices of mouse cortex with stac1 antibody showed labeling within neurons, consistent with reports of stac1 and stac2 mRNA in cortical neurons (Figure 4.1B) (Nelson et al., 2013). Similar analysis of acutely dissociated adult guinea pig ventricular myocytes (aGPVMs), however, showed no labeling of stac1 (Figure 4.1C). By contrast, aGPVM staining with stac2 antibody revealed low levels of stac2 labeling (Figure 4.1C) with weak t-tubular localization (Figure 4.1D-E). These results suggest that stac may be a regulator of both neuronal and cardiac ion channels.

Thus assured, we sought to determine whether stac is a selective modulator of Ca$_V$1, Ca$_V$2, or Na$_V$1 channels in heterologous systems. Accordingly, Figure 4.2A shows baseline effects of stac on Ca$_V$1.2 (Polster et al., 2015). Devoid of stac, Ca$_V$1.2 exhibits CaM-mediated CDI manifesting as enhanced decay of Ca^{2+} (red) versus Ba^{2+} current (black) when elicited using a step depolarization (top panel). As Ba^{2+} binds CaM poorly (Linse and Forsen, 1995), Ba^{2+}-currents furnish a convenient baseline measure of voltage-dependent inactivation without CDI. Upon coexpression of stac2, CDI is eliminated (Figure 4.2C). To quantify steady-state inactivation, we measured the fraction of peak Ca^{2+} and Ba^{2+} current remaining after 300-ms depolarization, r_{Ca} and r_{Ba} (Figure 4.2A-B, bottom panels). The strength of CDI is quantified as $CDI_{300} = 1 - r_{\mathrm{Ca}} / r_{\mathrm{Ba}}$, the fractional Ca^{2+}-dependent component of inactivation. Thus quantified, the population data confirms the strong reduction in CDI of $Ca_V1.2$ upon co-expression of stac2 ($p = 3.6\times10^{-5}$; Figure 4.2E). Further analysis demonstrates that both stac1 and stac3 isoforms also suppress CDI ($p = 2.0\times10^{-5}$ and 7.1×10^{-5} respectively, Figure 4.2B, D, E). Similarly, $Ca_V1.3$ short variant ($Ca_V1.3_S$), a close homolog of $Ca_V1.2$, also exhibits strong baseline CDI that is suppressed upon co-expression of stac2 (Figure 4.2F, H, J). Generalizing this phenomenon, both stac1 and stac3 isoforms also diminish CDI of $Ca_V1.3$ (Figure 4.2G, I, J). In like manner, we tested the effect of stac2 on $Ca_V1.4_{43*}$, a splice variant of $Ca_V1.4$ that exhibits robust CDI (Figure 4.2K) (Tan et al., 2012). Remarkably, stac2 strongly diminished CDI of $Ca_V1.4$ ($p = 3.2\times10^{-5}$; Figure 4.2L-M). In all cases, voltage-dependent inactivation is minimally perturbed by the presence of all three stac isoforms (Figure 4.2) while Ca^{2+}-regulation of Ca_V1 is potently suppressed.

Encouraged by its pervasiveness, we considered whether stac alters Ca^{2+}-dependent modulation of Ca_V2 isoforms abundant in the central nervous system. For $Ca_V2.1$, CaM elaborates both CDF and CDI (DeMaria et al., 2001; Lee et al., 2000). However, the Ca^{2+}-sensitivity of CDI process is over 50-fold weaker than that of CDF casting this negative feedback beyond physiological bounds (Lee et al., 2015). As such, we probed whether stac tunes CDF of $Ca_V2.1$ using a well-established prepulse protocol (DeMaria et al., 2001; Thomas and Lee, 2016). Figure 4.3A displays wildtype $Ca_V2.1$ currents in the absence of stac2. Upon presentation of an isolated test pulse to 0 mV, the activation of Ca^{2+} current follows a biphasic response (gray trace). Following a brief voltage prepulse, however, the ensuing test the ensuing test pulse yield enhanced Ca^{2+}-currents with monophasic activation reflecting CDF (red trace). Further quantification revealed no change in CDF of $Ca_V2.1$ following the addition of stac2 in both exemplar current recordings (Figure 4.3B) and population data (Figure 4.3C). For $Ca_V2.2$, CaM-regulation manifests as a kinetically slow CDI in response to step voltage depolarization (Figure 4.3D) (Liang et al., 2003). Intriguingly, CDI of $Ca_V2.2$ persisted despite overexpression of stac (Figure 4.3E). Population data of CDI_{800} quantified as the enhanced reduction in peak Ca^{2+} versus Ba^{2+} current ($1 - r_{Ca} / r_{Ba}$) following 800 ms of depolarization further confirms this trend (Figure 4.3F). Lastly, neuronal $Ca_V2.3$ also possesses robust and recognizable CDI (Figure 4.3G). Intriguingly, strong $Ca_V2.3$ CDI persists despite stac2 overexpression as confirmed by exemplary traces (Figure 4.3H). Furthermore, population data of CDI_{300} shows a minor reduction that is statistically insignificant ($p > 0.01$) (Figure 4.3I). These results reveal the selectivity of stac in tuning CaM feedback to Ca_V1 versus Ca_V2 channels.

Given this selectivity, we tested whether stac suppresses Ca^{2+}-regulation of Na_V1 channels. Though all Na_V1 possess a conserved CI module homologous to both Ca_V1 and Ca_V2 (Babitch, 1990), functional CDI that bears mechanistic similarity to Ca_V has thus far only been identified in $Na_V1.4$ (Ben-Johny et al., 2014). Unlike Ca_V channels, however, Na_V channels do not convey Ca^{2+} influx that triggers Ca^{2+}-feedback. As such, we used rapid photouncaging of Ca^{2+} to produce step-like increase in intracellular $[Ca^{2+}]_i$, whose magnitude is simultaneously measured via Ca^{2+} fluorescent indicators. Figure 4.3J displays baseline Ca^{2+}-regulation of $Na_V1.4$ channels. As CDI is kinetically slow in comparison to fast inactivation of Na_V channels, we applied a train of step-depolarizations evoked at 10 Hz to probe possible Ca^{2+}-dependent effects (Ben-Johny et al., 2014).

Without Ca^{2+}-uncaging, peak $Na_V1.4$ currents remained steady (gray dots). However, in response to a Ca^{2+} step, the peak $Na_V1.4$ current declined rapidly revealing CDI (red envelope). Upon stac overexpression, a similar Ca^{2+} step evoked robust CDI of $Na_V1.4$ as confirmed by exemplar traces (Figure 4.3K) and population data (Figure 4.3L). Overall, these results show the specificity of stac in tuning Ca^{2+}-regulation of Ca_V1 channels.

Stac utilizes an allosteric mechanism to suppresses CaM signaling – We sought to identify molecular mechanisms that underlie selective Ca_V1 modulation by stac. Accordingly, we systematically scanned candidate binding sites by using a live-cell FRET 2-hybrid assay (Erickson et al., 2001) to characterize binding between YFP-tagged $Ca_V1.3$ intracellular domains (Yang et al., 2014a) (Figure 4.4A) and CFP-tagged stac3 (Figure 4.4B). As all three stac variants suppress the CDI of all Ca_V1 channel isoforms, we chose $Ca_V1.3$ as YFP-tagged intracellular loop peptides are readily available and well characterized (Yang et al., 2014a), while stac3 was selected for its high potency in suppressing $Ca_V1.3$ CDI (Figure 4.2I). Accordingly, we quantified 3^3-FRET efficiency (E_A) between FRET pairs co-expressed in individual cells. By leveraging stochastic expression of the FRET pairs in cells, we obtained a saturating Langmuir relation between E_A and the free donor concentration (D_{free}) allowing for estimation of relative binding affinities ($K_{d,EFF}$). We found that stac3 binds well to the CI region ($K_{d,EFF} = 20697 \pm 3023\ D_{free} \sim 0.67 \pm 0.1\ \mu M$, Figure 4.4C). By contrast, analysis of the amino-terminus, intracellular loops between domains I and II (I-II loop), domains II and III (II-III loop), and domains III and IV (III-IV loop) revealed far weaker binding (Figure 4.4D-H). To further localize the putative binding loci, we subdivided the CI module into two: (1) a proximal CI segment (PCI) composed of dual vestigial EF hand and preIQ segments and (2) the IQ domain (IQ). Intriguingly, the YFP-tagged PCI segment bound stac3 with an ~10-fold higher affinity ($K_{d,EFF} = 17725 \pm 3990\ D_{free} \sim 0.58 \pm 0.1\ \mu M$) than the downstream IQ domain ($K_{\mathrm{d,EFF}} = 204739 \pm 25465\ D_{\mathrm{free}} \sim 6.67 \pm 0.8$ μM) (Figure 4.4C). In all, systematic FRET analysis reveals that stac binds to $\mathrm{Ca_V1}$ CI relying on upstream elements including the dual vestigial EF hand and preIQ domains, an interface distinct from that for CaM (Bazzazi et al., 2013; Minor and Findeisen, 2010).

To test for the functional relevance of stac binding to the $\mathrm{Ca_V1}$ CI module, we sought to confer stac-sensitivity to stac-insensitive channels via a chimeric approach. We turned to $\mathrm{Ca_V2.3}$ that lacks strong stac-mediated CDI suppression (Figure 4.3G-I), yet readily forms functional chimeras with $\mathrm{Ca_V1}$ channels (Mori et al., 2008; Yang et al., 2014a). Accordingly, we replaced the CI region of $\mathrm{Ca_V2.3}$ with the corresponding segment from $\mathrm{Ca_V1.3}$ ($\mathrm{Ca_V2.3/1.3CI}$). Devoid of stac, $\mathrm{Ca_V2.3}$-1.3CI channels exhibit strong CDI driven by local Ca^{2+} (Figure 4.5A, C), isolated by high intracellular buffering. In contrast to wildtype $\mathrm{Ca_V2.3}$, stac2 co-expression strongly attenuated CDI ($p = 4.7\times10^{-4}$, Figure 4.5B, C) suggesting that the $\mathrm{Ca_V1}$ CI module is necessary for stac-mediated suppression of CDI.

Given that both CaM and stac share the CI module as an effector site, two disparate mechanistic possibilities may engender functional suppression of Ca^{2+}-regulation. First, the binding of stac may competitively displace Ca^{2+}-free CaM (apoCaM) from its preassociation site. Second, stac may supersede CaM signaling to the channel pore via an allosteric mechanism. Systematic FRET analysis suggests that stac preferentially binds upstream CI elements (Figure 4.4C) while high-affinity CaM preassociation is supported via the IQ domain (Bazzazi et al., 2013; Minor and Findeisen, 2010) hinting that the two modulatory proteins may bind concurrently. To explicitly rule out competitive displacement of CaM preassociation functionally, we covalently tethered CaM onto the $\mathrm{Ca_V1.3}$ carboxy-terminus using a poly-glycine linker ($\mathrm{Ca_V1.3_S}$-CaM) (Mori et al., 2004; Yang et al., 2014a). This maneuver enables robust CDI (Figure 4.5D) and ensures a high local concentration of CaM near the $\mathrm{Ca_V1}$ channel extending into the millimolar range, sufficient to thwart even high levels of a competitive inhibitor (Mori et al., 2004). Dominant-negative $\mathrm{CaM_{1234}}$ with its $\mathrm{Ca^{2+}}$-binding sites disabled, typically competitively displaces intact apoCaM from the CI module thereby resulting in a complete loss of CDI for wildtype channels (Figure 4.6A). However, co-expression of $\mathrm{CaM_{1234}}$ with $\mathrm{Ca_V1.3_S}$-CaM does not abrogate CDI highlighting the protective nature of fused CaM against competitive inhibitors (Figure 4.6B). Thus, if stac competitively displaces CaM, then strong CDI should persist for $\mathrm{Ca_V1.3_S}$-CaM despite over-expression of stac. However, CDI of $\mathrm{Ca_V1.3_S}$-CaM is strongly diminished by co-expression of stac2 ($p = 3.8\times10^{-6}$, Figure 4.5E-F) and stac3 ($p = 4.5\times10^{-4}$, Figure 4.6C). We observed a similar fate for $\mathrm{Ca_V1.2}$-CaM in the presence of stac2 ($p = 1.5\times10^{-5}$, Figure 4.5G-I). These results suggest that both stac and CaM act concurrently via distinct sites, in contradiction with a competitive mechanism.

Elementary mechanisms underlying stac-regulation of $\mathrm{Ca_V1}$ – In addition to $\mathrm{Ca^{2+}}$-dependent regulation, apoCaM binding itself tunes the baseline gating of $\mathrm{Ca_V}$ channels (Adams et al., 2014). Absent stac, $\mathrm{Ca_V1}$ lacking prebound CaM adopt a low P_O gating configuration (empty configuration, $P_{O/E}$) while apoCaM binding switches channels into a high P_O gating mode (CaM-bound configuration, $P_{O/A}$) (Adams et al., 2014). $\mathrm{Ca^{2+}}$/CaM divests this initial enhancement in P_O and returns channels into a low P_O gating mode ($P_{O/E}$) manifesting as CDI. The addition of stac as a second regulatory ligand vastly enriches this modulatory scheme (Figure 4.7A). Three distinct mechanistic scenarios may thus underlie suppression of $\mathrm{Ca^{2+}}$-regulation by stac as illustrated in Figure 4.7B: (1) stac binding may pre-inhibit or lock channels into the low P_O gating configuration ($P_{O/E}$) akin to $\mathrm{Ca^{2+}}$-inactivated channels and forestall further $\mathrm{Ca^{2+}}$-modulation, (2) stac may obstruct $\mathrm{Ca^{2+}}$/CaM-dependent modulation alone sparing apoCaM to freely elicit changes in baseline P_O switching between $P_{O/E}$ and $P_{O/A}$, (3) stac-binding may allosterically lock channels into a high P_O gating mode irrespective of CaM-binding status. For Scenario 3, it is possible that the baseline P_O of $Ca_V1.3$ in the presence of stac may be distinct from that observed with CaM-overexpressed. Importantly, the three scenarios may be distinguished at the single-molecule level by assessing Ca_V channel P_O under various CaM-bound conditions using low-noise electrophysiology. Hence, we focused on $Ca_V1.3$ given the rich assortment of post-transcriptionally and post-translationally modified channel variants with vastly distinct CaM binding affinities (Bazzazi et al., 2013; Liu et al., 2010; Singh et al., 2008). We focused on three variants, $Ca_V1.3_S$ with high apoCaM affinity, and $Ca_V1.3_{MQDY}$ and $Ca_V1.3_L$ with low affinities. These variants possess distinct baseline P_O and corresponding levels of CDI and constitute a rich platform to unravel stac-dependent effects (Adams et al., 2014; Tan et al., 2011).

First, we analyzed $Ca_V1.3_S$ in the presence and absence of stac (Figure 4.7C-E) to determine whether stac may promote channel entry into a low P_O gating configuration. $Ca_V1.3_S$ is typically prebound to CaM at endogenous CaM concentrations given their high affinity (Adams et al., 2014). We employed Ba^{2+} as a charge carrier to estimate baseline behavior of channels without confounding effects of CDI. A slow voltage-ramp (shown between -50 and +40 mV) evokes stochastic channel openings that approximate near steady-state P_O at each voltage. Stochastic records displayed in Figure 4.7C show channel openings as downward deflections to the open level (gray curves) and closures correspond to the zero-current portions of the trace. Robust channel openings are detected both in the presence and absence of stac (Figure 4.7C). To estimate steady-state P_O versus voltage relationship, we averaged many stochastic records to obtain a mean current that is divided into the open level, and averaged over multiple patches. $Ca_V1.3_S$ variant exhibits high P_O in the absence of stac (Figure 4.7D) in agreement with previous studies (Adams et al., 2014). Upon over-expression of stac2, the open probability remains high with an ~10 mV hyperpolarizing shift in the voltage-dependence of activation (Figure 4.7D). We further scrutinized single channel trials to assess changes in gating modes. Figure 4.8 displays ten sequential trials of Ca$_{V}$1.3 single channel activity evoked by voltage-ramps introduced at 12 sec intervals both in the presence and absence of stac. In the absence of stac, Ca$_{V}$1.3$_{S}$ activity switches between epochs of high activity and brief periods of low activity, as evident from diary plot of average P_{O} within individual trails ($\bar{P}_{O}$) (Figure 4.8B). Analysis of single-trial $\bar{P}_{O}$ distribution reveals a bimodal distribution denoting discrete high and low P_{O} gating modes (Figure 4.7E). Upon stac overexpression, however, channel activity is largely high as evident from $\bar{P}_{O}$ diary plots (Figure 4.8D) and single-trial $\bar{P}_{O}$ distribution (Figure 4.7E). Thus, in contradiction with scenario 1, stac bound channels are not preinhibited; rather, channels preferentially adopt a high P_{O} gating mode.

To distinguish between the second and third mechanistic possibilities, we considered Ca$_{V}$1.3 variants with weakened apoCaM binding affinity that largely reside in the low P_{O} configuration (Adams et al., 2014). Accordingly, we tested the baseline P_{O} of Ca$_{V}$1.3$_{MQDY}$, an RNA-edited variant whose central isoleucine within the IQ domain is substituted to a methionine, (Bazzazi et al., 2013; Huang et al., 2012) and an alternative splice variant Ca$_{V}$1.3$_{L}$ containing an autoinhibitory domain that competitively displaces CaM (Liu et al., 2010; Singh et al., 2008). In the absence of stac and under endogenous CaM levels, both Ca$_{V}$1.3$_{MQDY}$ (Figure 4.7F-G) and Ca$_{V}$1.3$_{L}$ (Figure 4.7I-J) open sparsely, exhibiting a sharply diminished maximal P_{O} consistent with channels lacking CaM (Adams et al., 2014; Bock et al., 2011). Indeed, single-channel trials of Ca$_{V}$1.3$_{MQDY}$ (Figure 4.9A-C) and Ca$_{V}$1.3$_{L}$ (Figure 4.10A-C) under endogenous levels of CaM reveal uniformly low activity with single-trial $\bar{P}_{O}$ distribution restricted to low limits (Figure 4.7H for Ca$_{V}$1.3$_{MQDY}$; Figure 4.7K for Ca$_{V}$1.3$_{L}$). CaM overexpression with both channel variants, reveal the resurgence of epochs of high activity (Figure 4.9D-E; Figure 4.10D-E) and a bimodal $\overline{P_O}$ distribution with a substantial fraction of trials corresponding to a high P_O gating configuration (Figures 4.7H and 4.7K for $Ca_V1.3_{MQDY}$ and $Ca_V1.3_L$ respectively). Upon stac co-expression, robust channel openings re-emerge for both $Ca_V1.3_{MQDY}$ (Figures 4.7F-G) and $Ca_V1.3_L$ (Figures 4.7I-J) yielding a markedly enhanced baseline P_O akin to $Ca_V1.3_S$ variant (Adams et al., 2014). In fact, scrutiny of single-channel trails for both channel variants reveal uniformly high channel activity (Figure 4.9F-G for $Ca_V1.3_{MQDY}$; Figure 4.10F-G for $Ca_V1.3_L$) and single-trial $\overline{P_O}$ distributions are now firmly within the high activity limits (Figures 4.7H and 4.7K) reminiscent of the CaM overexpression. Interestingly, the steady state P_O-V relations for $Ca_V1.3_S$, $Ca_V1.3_{MQDY}$ and $Ca_V1.3_L$ in the presence of stac closely approximate each other with a maximal P_O matching that for channels with prebound apoCaM (Figures 4.7D, G, and J). These findings demonstrate that consistent with Scenario 3, stac-binding locks $Ca_V1.3$ channels in the high P_O configuration and effectively decouples the channel pore from CaM-dependent conformational changes. Moreover, these results highlight the dominance of stac over CaM in modulation of Ca_V1.

U-domain constitutes a minimal motif for Ca_V1 CDI suppression – With elementary mechanisms discerned, we turned to identify stac motifs functionally-critical for allosteric suppression of CaM-regulation. Structurally, stac isoforms share a strikingly modular architecture composed of a C1 domain linked to one or two SH3 domains via a largely unstructured linker segment (U-linker region) (Suzuki et al., 1996). As these modular subcomponents typically recognize distinct ligands, we reasoned that their molecular functions may be separable (Cohen et al., 1995; Colon-Gonzalez and Kazanietz, 2006). Accordingly, we trisected stac2 to assess whether individual subcomponents can recapitulate functional regulation. We focused initially on C1 and tandem SH3 domains as these segments were recently shown to be critical for $Ca_V1.1$ binding and triadic localization in skeletal muscle (Campiglio and Flucher, 2017; Wong King Yuen et al., 2017). Surprisingly, co-expression of either segment, however, only minimally perturbed CDI of Ca$_V$1.2-CaM (Figures 4.11A, C, and D). By contrast, the linker region by itself fully abolished CDI of these channels ($p = 8.9\times10^{-6}$, Figures 4.11B, D), recapitulating the effect of stac2 on Ca$_V$1.2.

To further localize vital functional domains within the U-linker, we undertook bioinformatic analysis to identify highly conserved regions. We performed multiple sequence alignment of complete sequences of 780 orthologs of stac isoforms using the MUSCLE algorithm (Edgar, 2004) and subsequently computed an empirical measure for the degree of protein sequence conservation at each position. The degree of conservation is defined as the likelihood of observing the consensus residue at each sequence position divided by the number of distinct residues observed at this position. By this algorithm, perfectly conserved residues will yield a unitary value while poorly conserved residues have a lower score. Thus probed, we identified a 22-amino acid stretch, termed the U-domain ('unknown' domain), exhibiting a high degree of conservation (Figure 4.11E, blue shaded region). Remarkably, coexpression of U-domain alone is sufficient to strongly diminish CDI of both Ca$_V$1.2-CaM and Ca$_V$1.3-CaM (Figure 4.11F-H). Thus armed, we undertook systematic alanine scanning mutagenesis of stac2 U-domain to identify functionally-critical residues (Figure 4.11I; Figure 4.12). Remarkably, coexpression of mutant stac2 with triple alanine substitution of residues ETL[206-208] resulted in minimal disruption of Ca$_V$1.2 and Ca$_V$1.3 CDI (Figure 4.11J-K) suggesting that these residues are necessary for stac function. Further analysis also revealed residues PVY[203-205] and KVD[200-202] to be critical for stac function (Figure 4.11I; Figure 4.12A-C). Residues outside these loci only minimally affected stac function (Figure 4.11I; Figure 4.12D-G). Altogether, these findings demonstrate the necessity and sufficiency of the U domain as a minimal motif in suppressing CaM-regulation of Ca$_V$1 channels.

U-domain modulates native Ca$_V$1 and reshapes cardiac action potentials – Having identified minimal U-domain that fully recapitulates stac mediated CDI suppression, we sought to assess the physiological consequences of stac misregulation in ventricular myocytes. Accordingly, we synthesized the U-domain of stac2 as a peptide and delivered it via pipet dialysis to acutely elevate the myocyte's cytosolic concentration. We functionally validate the synthesized peptide by first testing its effect on recombinant Ca$_V$1.2 expressed in HEK293 cells (Figure 4.13A). Following pipet dialysis of the U-peptide, CDI of Ca$_V$1.2 was strongly suppressed as evident from exemplar currents and population data (Figure 4.13B-C).

Thus affirmed, we isolated ventricular myocytes from adult guinea pigs (aGPVMs) to probe changes in CDI of native Ca$_V$ channels and action potential duration in response to changes in stac levels (Figure 4.13D). Devoid of U-peptide, endogenous Ca$_V$ channels in ventricular myocytes displayed strong CDI, establishing baseline levels of CaM-regulation (Figure 4.13E). Remarkably, pipet dialysis of U-peptide dramatically reduced CDI in myocytes (Figures 4.13E-F). The dramatic reduction in overall inactivation of Ca$_V$ channels suggests that fluctuations in stac levels may markedly alter action potential waveforms. To explicitly test this possibility, we collected current clamp recordings of aGPVMs and compared action potential waveforms in the presence and absence of U-peptide. Figure 4.13G shows typical voltage profiles of action potentials in aGPVMs paced at 0.5 Hz. Waveforms are stable between traces and the mean action potential duration (APD_{80}), the duration of time when the action potential is 80% repolarized, is 277.9 ± 31.37 ms (mean ± S.E.M., n = 6). Figure 6H displays the complement of the cumulative distribution of APD_{80}. When the peptide is added to the internal solution, APD_{80} is greatly enhanced to 740.1±105.49 ms (n = 6) (Figure 4.13G-H). Thus, the U-peptide both alters the CDI of endogenous cardiac Ca_V1 and, in so doing, markedly prolongs the APD. This action potential prolongation may ultimately destabilize rhythmicity of the heart.

DISCUSSION

Though distinct physiologically, Ca_V1, Ca_V2, and Na_V1 feature a modular CI element suggesting a common fingerprint of CaM interaction and shared mechanistic basis for Ca^{2+}-regulation. Our findings suggest that stac allosterically overrides CaM-signaling to Ca_V1 by locking the channel into a high P_O gating mode irrespective of whether apoCaM or Ca^{2+}/CaM is bound. This effectively disengages the pore from CaM-conformational changes and abolishes CDI.

In cardiac myocytes, CDI of Ca_V1 is a key factor for action potential duration (Limpitikul et al., 2014; Mahajan et al., 2008). Experimentally, this prominence is inferred from prolongation of action potentials upon expression of mutant CaM_{1234} (Alseikhan et al., 2002). Yet, constitutive CaM expression may evoke nonspecific effects (Hall et al., 2013; Wang et al., 2007) that obfuscate the net contribution of Ca_V1 CDI (Ben-Johny et al., 2015). Acute elevation of the U-domain bypasses these ambiguities and confirms a key role for Ca_V1 CDI for cardiac action potentials. Pathophysiologically, aberrant stac expression may be also be a risk factor for arrhythmias as differential expression of stac2 has been reported in right ventricular heart failure hinting at a potential role in calcium remodeling following heart failure (di Salvo et al., 2015).

Furthermore, we show that stac uniformly locks $Ca_V1.3$ variants into a high P_O configuration incapable of CDI, thus abolishing diversity in gating behavior. Post-transcriptional modification of $Ca_V1.3$ generates an impressive array of variants with modified carboxy-termini (Bock et al., 2011; Huang et al., 2012) to modulate rhythmicity in suprachiasmatic nucleus (Huang et al., 2012), substantia nigra (Adams et al., 2014; Guzman et al., 2009) and chromaffin cells (Vandael et al., 2010). Notably, the functional manifestation of $Ca_V1.3$ alternative splicing is cell-type specific suggesting that auxiliary regulators may refine channel properties (Scharinger et al., 2015). Consequently, resolving stac function in these settings may reveal new physiological and pathophysiological insights.

Stac1 and stac2 isoforms are expressed in both hippocampal and midbrains neurons as well as ventricular cardiac myocytes, cell-types where endogenous Ca_V1 exhibit robust CDI (Bazzazi et al., 2013; Oliveria et al., 2012) (Figure 4.13E). As all stac variants shunted CDI of Ca_V1 in HEK293, it is possible that stac function may be tightly regulated in native settings. One possibility is that stac abundance may be limited either developmentally (Suzuki et al., 1996) or via interacting proteins (Satoh et al., 2006). Indeed, acute elevation of U-domain diminished CDI in myocytes consistent with low baseline stac function. Physiologically, as Ca_V1 CDI is a potent homeostatic mechanism that prevents pathological Ca^{2+}-overload (Dunlap, 2007), a low concentration regime of stac may be advantageous. By modulating a subpopulation of Ca_V1, stac may circumvent homeostatic requirements to amplify local Ca^{2+}-signals via sustained Ca^{2+} influx. The C1 and SH3 domains may serve as scaffolds to localize stac to specific signaling complexes (Campiglio and Flucher, 2017; Cohen et al., 1995; Colon-Gonzalez and Kazanietz, 2006). Alternatively, phosphorylation of stac may dynamically tune its function (Huttlin et al., 2010). Resolving these complexities may unveil mechanisms that tune Ca_V function spatially and temporally.

Interestingly, Ca^{2+}-binding proteins (CaBPs) (Haeseleer et al., 2000) also suppress CaM signaling to Ca_V1 (Lee et al., 2002; Yang et al., 2006). Mechanistically, CaBPs exploit a mixed allosteric scheme – at low concentrations, CaBPs engage interfaces distinct from that of CaM and while at higher concentrations CaBPs displace CaM (Findeisen and Minor, 2010; Oz et al., 2013; Yang et al., 2014a). Like stac, CaBPs also interact with upstream CI module of Ca_V1 hinting at commonalities in regulatory mechanisms (Oz et al., 2013; Yang et al., 2014a; Zhou et al., 2005).

The selectivity of CaBPs in modulating Ca$_V$1, however, is yet to be resolved as CDF of Ca$_V$2.1 is reduced (Lee et al., 2002) though CDI of Ca$_V$2.3 is unperturbed (Yang et al., 2014a). Nonetheless, the existence of other regulatory proteins to curtail Ca^{2+}-feedback points to a general class of auxiliary regulators of CaM-signaling and identifying such molecular players is critical to elucidating how CaM signaling is globally orchestrated.

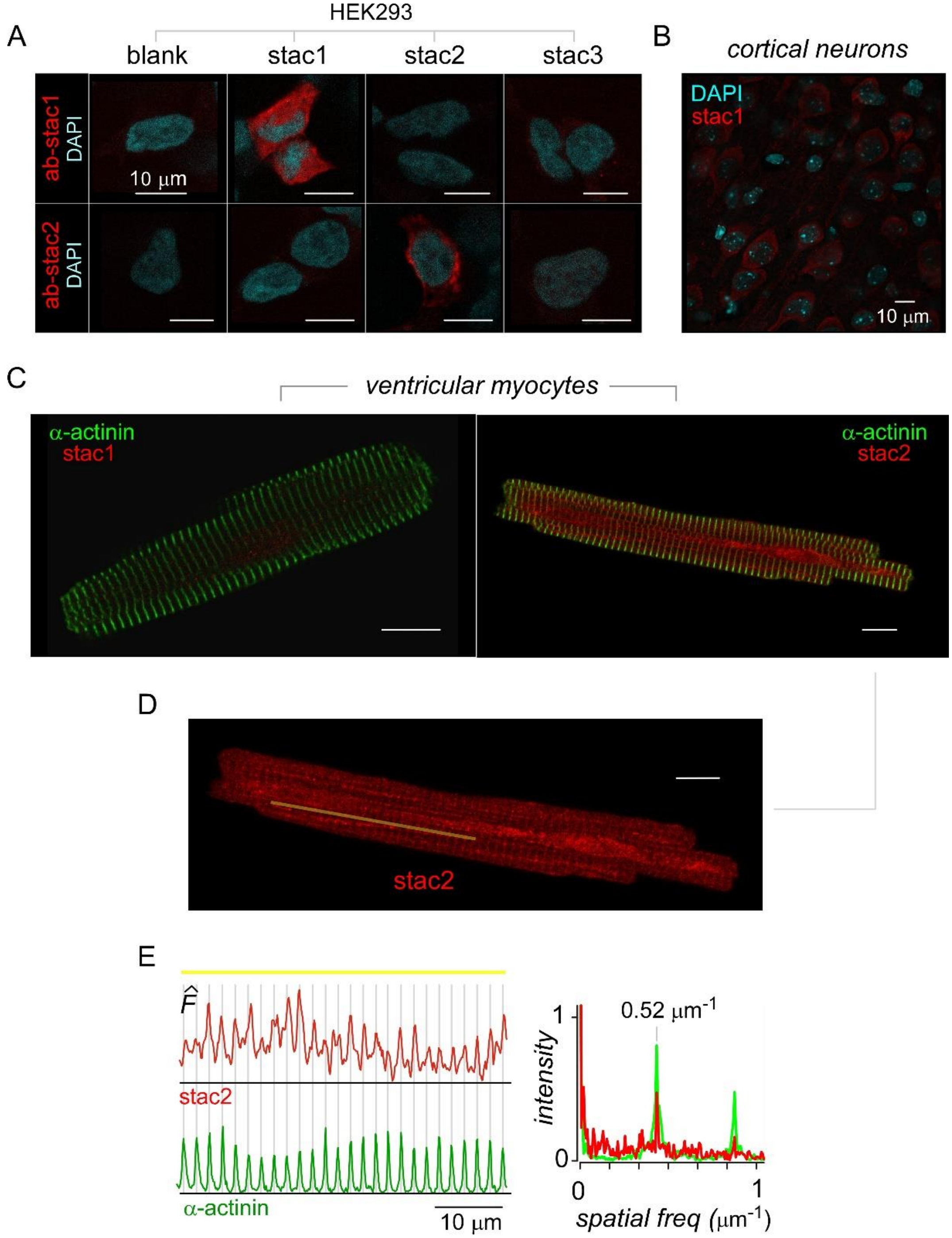

Figure 4.1. Stac2 is differentially expressed in cardiac myocytes and neurons.
(A) HEK293 transfected with stac1-3 (top) and immunostained with DAPI (cyan) and stac1 (red, top) or stac2 (red, bottom) antibodies confirm selectivity of stac antibodies. Images representative of 3 field of views.
(B) Coronal slices of mouse cortex immunostained with DAPI (cyan) and stac1 (red). Images representative of 5 field of views.
(C) Acutely dissociated aGPVM immunostained with α-actinin (green) and stac1 (red, left) and stac2 (red, right). Images representative of 3 field of views.

(D) Stac2 immunostaining reveals weak t-tubular localization in aGPVM. Image reproduced from panel C. Yellow line, line-scan used in panel E. Images representative of 7 field of views.
(E) Fluorescence intensity of stac2 (red, left) and α-actinin (green, left) across the line-scan shown in panel D from left to right. Vertical lines correspond to location of the peak fluorescence intensity for α-actinin. Right subpanel shows prominent spatial frequency of 0.52 μm^{-1} with both α-actinin (green) and stac2 (red).

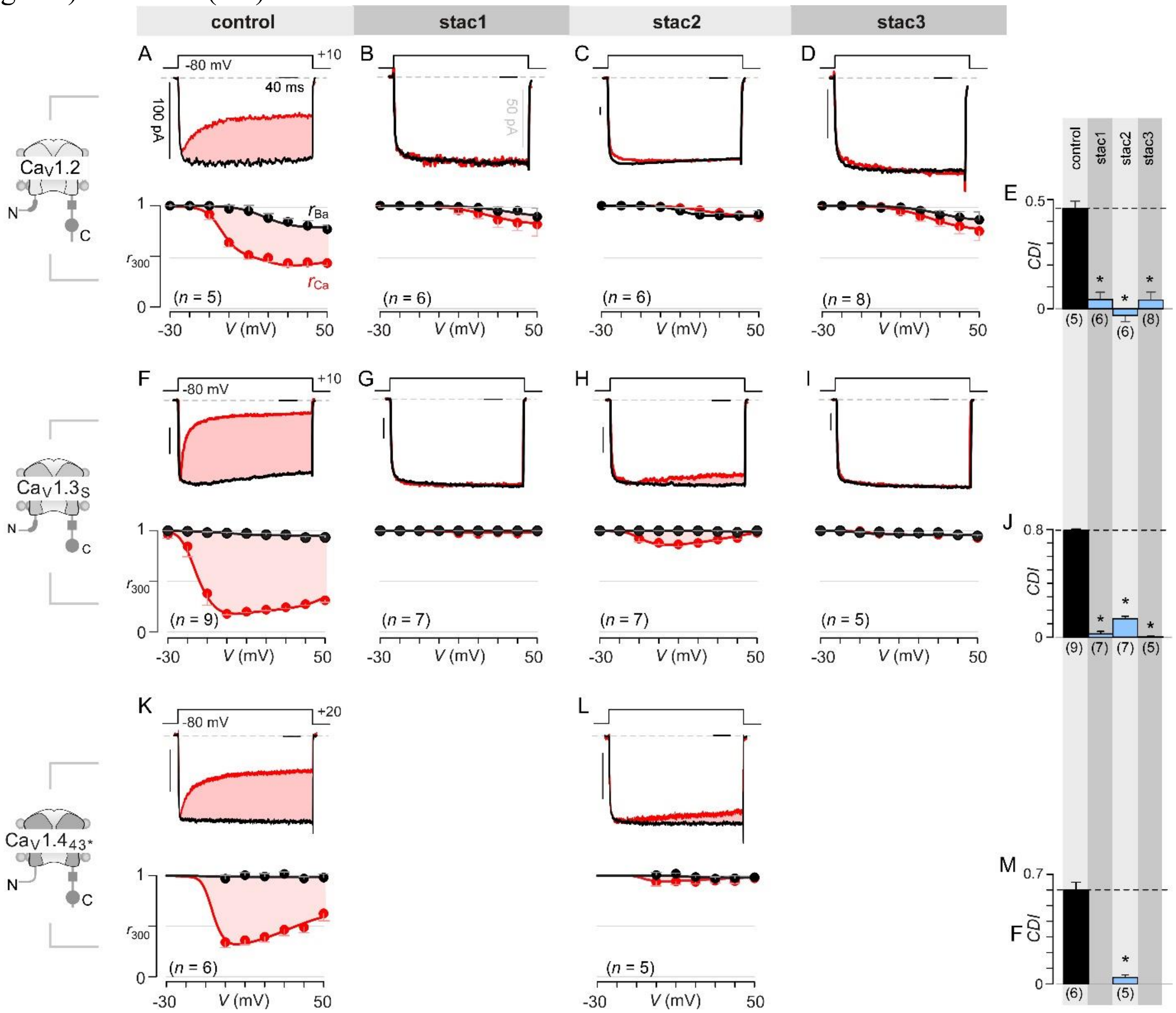

Figure 4.2. Stac abolishes Ca^{2+}/CaM-regulation in Ca$_V$1 channels.
Cartoon schematic of channel interrogated is shown in the left column.
(A) Ca$_V$1.2 expressed in HEK293. Top, exemplar current traces evoked in response to +10 mV voltage-step shows robust CDI (rose shaded area) evident as enhanced current decay with Ca^{2+} (red) versus Ba^{2+} (black) as the charge carrier. Bottom, population data for the extent of steady-state inactivation in Ca^{2+} (red) and Ba^{2+} (black), here, is estimated by the metric r_{300}, the ratio of current remaining at 300ms to peak current during a depolarizing pulse, plotted as a function of voltage. CDI is once again shaded in rose. Each symbol, mean ± SEM from specified number of cells (*n*).
(B) Stac1 abolishes CDI in Ca$_V$1.2. Format as in panel A.
(C) Similarly, stac2 eliminates CDI in Ca$_V$1.2. Format as in panel A.

(D) Finally, stac3 also reduces CDI in Ca$_V$1.2. Format as in Panel A.
(E) Bar graph displays population data of CDI for Ca$_V$1.2 in the absence and in the presence of stac1, stac2, or stac3. Dashed line shows baseline CDI = 1 – r_{Ca} / r_{Ba} in the absence of stac for comparison. Each bar, mean ± S.E.M. obtained from specified number of cells (*n*).
(F-J) Stac isoforms also suppress CDI of Ca$_V$1.3$_S$, the canonical short variant, as confirmed by both exemplar traces (panel F-I) and population data (panel J). Format as in panels A-E.
(K-M) Stac2 abolishes CDI of Ca$_V$1.4$_{43*}$. Format as in panels A, C, and E respectively.

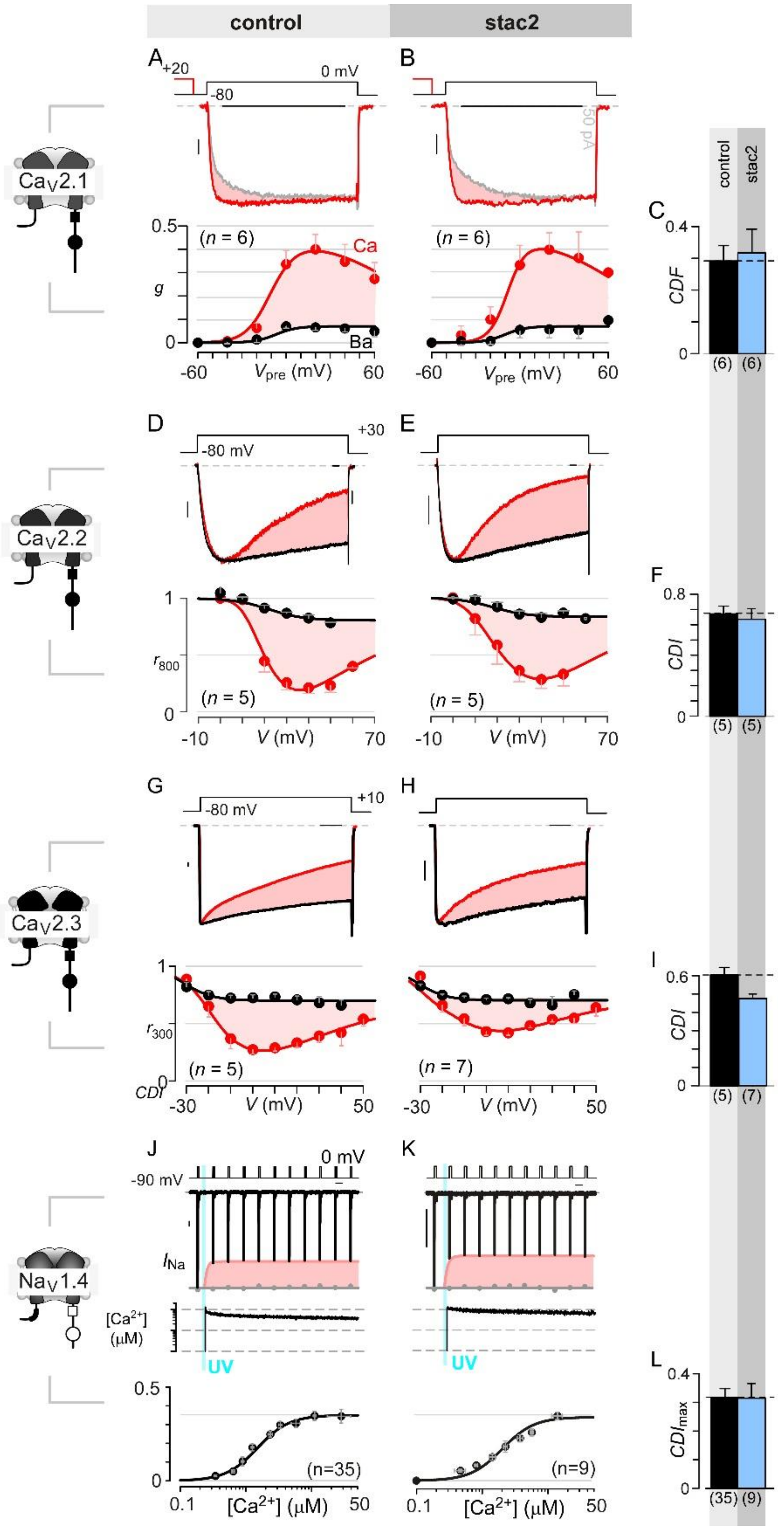

Figure 4.3. Stac does not affect Ca^{2+}/CaM-regulation in Ca_V2 channels or $Na_V1.4$.

(A) $Ca_V2.1$ exhibits robust CDF when evaluated using a prepulse protocol. Top, an isolated test pulse to 0 mV elicits Ca^{2+} currents with biphasic activation, containing rapid and slow components due to a superposition of voltage activation and CDF (gray). With a +20 mV prepulse, sufficient

Ca^{2+} enters to partially facilitate channels such that the subsequent step to 0 mV has a markedly blunted slow component (red). The area between the two current traces (ΔQ), divided by τ_{slow}, yields facilitation (g). Bottom, population data for g plotted as a function of prepulse potentials reveals a U-shaped dependence of Ca^{2+}-dependent facilitation. Each symbol, mean ± SEM from specified number of cells (n).

(B) Stac2 spares CDF of $Ca_V2.1$. Format as in panel A.

(C) Bar graph plots, population data for CDF = $g_{Ca} - g_{Ba}$. Each bar, mean ± S.E.M. obtained from specified number of cells.

(D-F) Stac2 spares CDI of $Ca_V2.2$ assessed in response to +30 mV test pulse. Format as in Figure 4.1A, C, and E respectively. Here, CDI is evaluated following 800 ms, to accommodate slow inactivation kinetics.

(G-I) Stac2 spares CDI of $Ca_V2.3$. Format as in Figure 4.1A, C, and E respectively.

(J-L) Stac2 spares CDI of $Na_V1.4$. Both in the absence and presence of stac, $Na_V1.4$ peak currents decline following a Ca^{2+} step (rose fit) (panel J, top). Gray dots, peak currents before uncaging. $CDI = 1$ – average peak I_{Na} of last 4 responses after Ca^{2+} uncaging / peak I_{Na} before uncaging. Bar graph plots maximal CDI observed with Ca^{2+} steps > 5 μM (panel L). Each bar, mean ± S.E.M. obtained from specified number of cells.

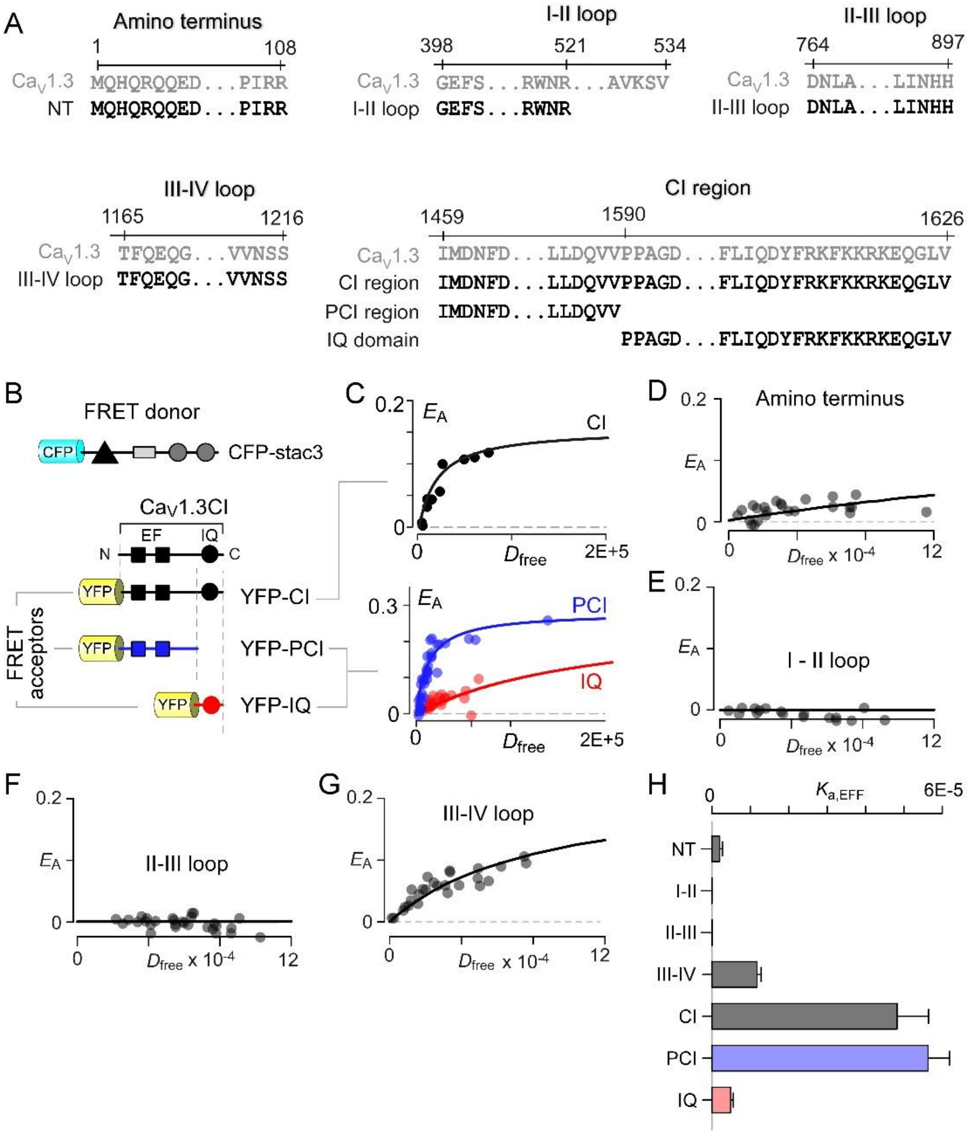

Figure 4.4. Systematic FRET 2-hybrid scan of major intracellular domains of $Ca_V1.3$ with stac.
(A) Schematic depicts design of YFP-tagged $Ca_V1.3$ intracellular loop constructs (NT, I-II loop, II-III loop, III-IV loop, CI region, PCI region, IQ domain). The exact sequence of the N- and C-termini of each peptide as well as locations on the $Ca_V1.3$ α subunit are denoted.
(B) Cartoon shows FRET pairs, CFP-stac3 with YFP-CI, YFP-PCI, and YFP-IQ of $Ca_V1.3$.
(C) FRET-binding curves show robust binding of stac3 to both the CI and PCI segment while binding to IQ is weaker.
(D-G) FRET 2-hybrid binding curves for stac3 interaction with various channel intracellular loops (black symbol and fit). Each symbol denotes FRET measurements from a single cell. Stac3 binds very weakly to the Amino terminal (NT) peptide (panel D) that includes the CaM-binding segment, *NSCaTE*. Both the I-II (panel E) and the II-III loop peptides (panel F) also showed little or no FRET binding. By contrast, the III-IV loop peptide bound appreciable to stac3 (panel G).
(H) Bar graph summarizes the relative association constant, $K_{a,EFF}$, of stac3 binding to major channel intracellular domains.

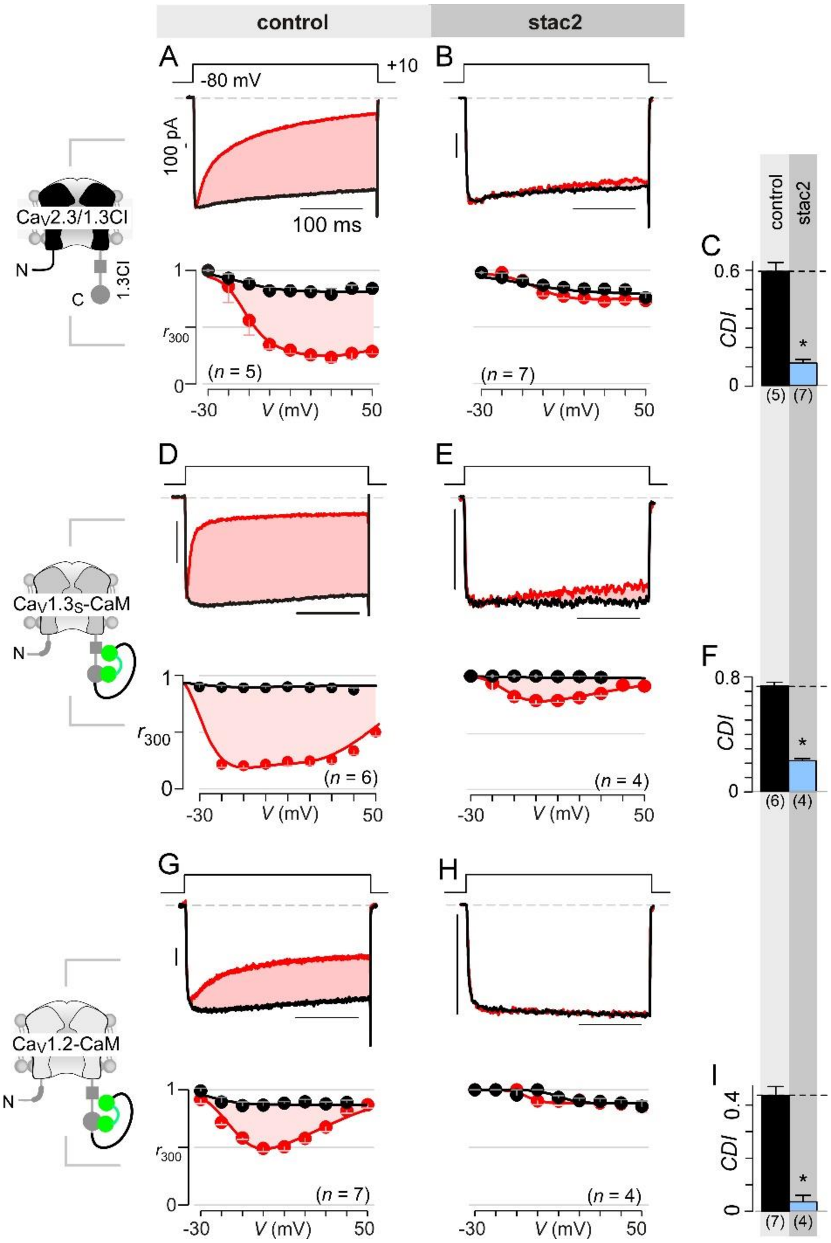

Figure 4.5. Allosteric regulation of stac by interaction with the channel carboxy-terminus.
(A-C) Transferring $Ca_V1.3_S$ CI to $Ca_V2.3$ ($Ca_V2.3/1.3CI$) unveils latent stac2 mediated suppression of CDI. Format as in Figure 4.1A, C, and E respectively.
(D-F) Stac2 suppresses CDI of $Ca_V1.3_S$ tethered to CaM. Fusion of CaM protects $Ca_V1.3_S$ from competitive inhibitors such as CaM_{1234}. Format as in Figure 4.1A, C, and E respectively.

(G-I) Stac2 suppresses CDI of Ca$_V$1.2 tethered to CaM. Format as in Figure 4.1A, C, and E respectively.

Figure 4.6. Dominant-negative CaM1234 competitively abolishes CDI.

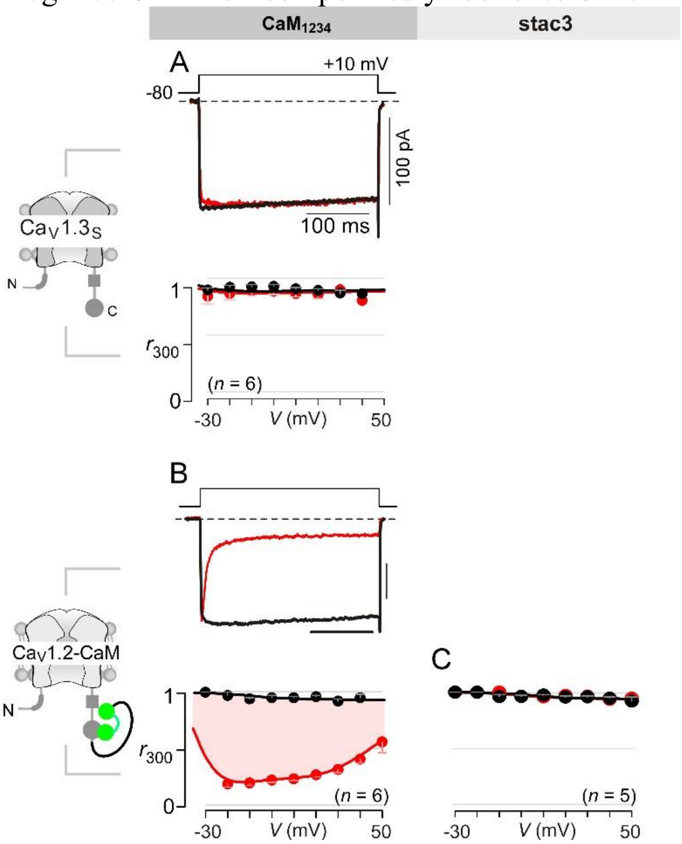

(A) CDI of Ca$_V$1.3$_S$ is absent in the presence of CaM$_{1234}$. Format as in Figure 4.1A.
(B) Fusion of CaM$_{WT}$ protects Ca$_V$1.3$_S$ from CaM$_{1234}$, a competitive inhibitor of *CDI*. Exemplar currents shows robust CDI of Ca$_V$1.3$_S$-CaM under both control conditions and in the presence of CaM$_{1234}$. These results demonstrate that CaM-fusion can protect Ca$_V$1.3 from competitive inhibition of CDI. Format as in Figure 4.1A.
(C) Population data of r_{300} confirms the abolition of Ca$_V$1.3$_S$-CaM CDI with stac3. Format as in bottom panel of Figure 4.1A.

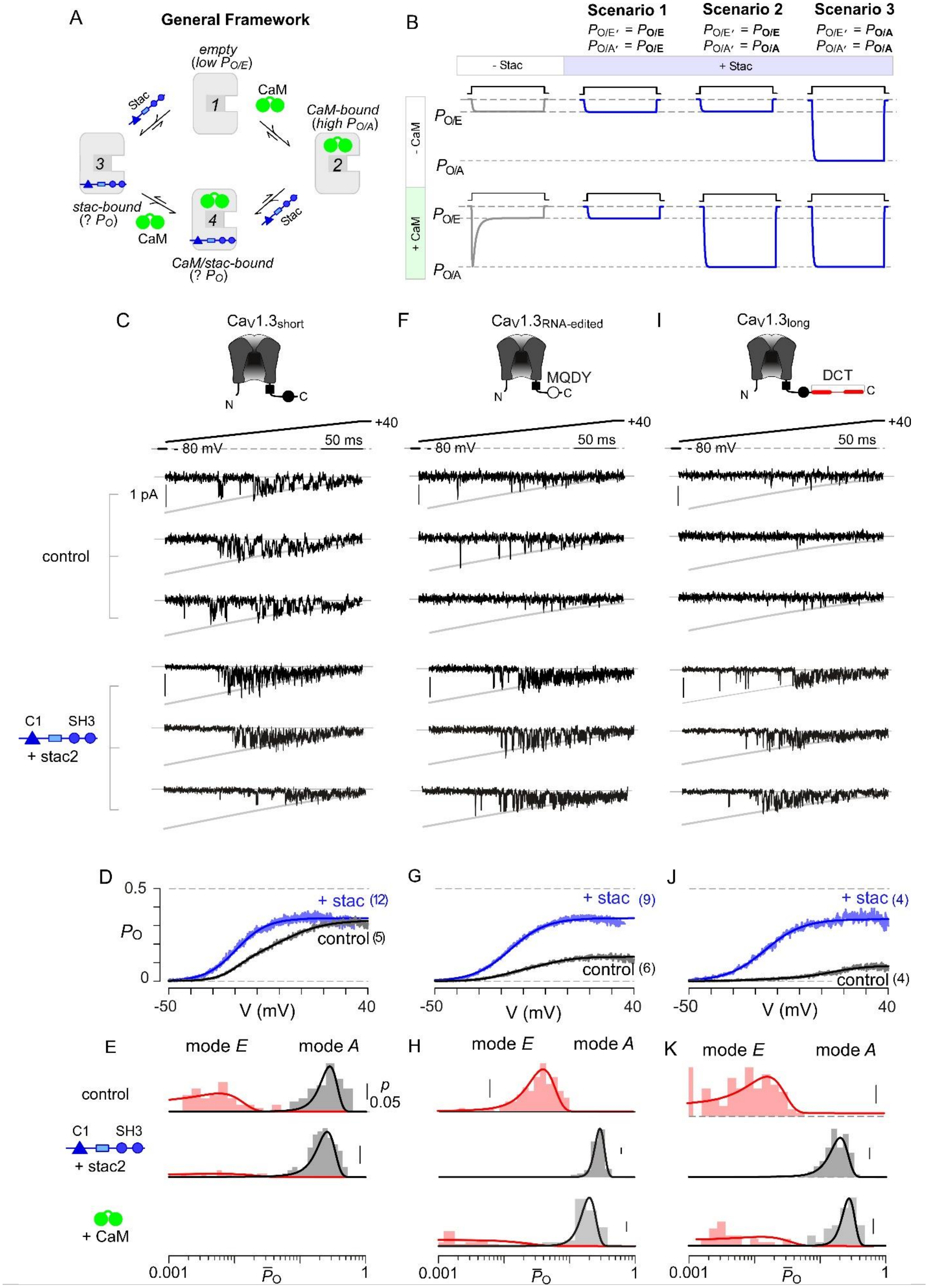
A
General Framework
empty
(low $P_{O/E}$)
1
CaM
CaM-bound
(high $P_{O/A}$)
2
Stac
3
stac-bound
(? P_O)
CaM
4
CaM/stac-bound
(? P_O)
Stac
B
Scenario 1
$P_{O/E'} = P_{O/E}$
$P_{O/A'} = P_{O/E}$
Scenario 2
$P_{O/E'} = P_{O/E}$
$P_{O/A'} = P_{O/A}$
Scenario 3
$P_{O/E'} = P_{O/A}$
$P_{O/A'} = P_{O/A}$
- Stac
+ Stac
- CaM
+ CaM
$P_{O/E}$
$P_{O/A}$
$P_{O/E}$
$P_{O/A}$
C
$Ca_V1.3_{short}$
N
C
F
$Ca_V1.3_{RNA\text{-}edited}$
MQDY
N
C
I
$Ca_V1.3_{long}$
DCT
N
C
+40
- 80 mV
50 ms
1 pA
control
C1
SH3
+ stac2
D
0.5
P_O
0
+ stac (12)
control (5)
-50
V (mV)
40
G
+ stac (9)
control (6)
-50
V (mV)
40
J
+ stac (4)
control (4)
-50
V (mV)
40
E
mode E
mode A
p
0.05
control
C1
SH3
+ stac2
+ CaM
0.001
$\bar{P}_O$
1
H
mode E
mode A
0.001
$\bar{P}_O$
1
K
mode E
mode A
0.001
$\bar{P}_O$
1

Figure 4.7. Stac enhances the P_O of Ca$_V$1.3.
(A) A general four-state scheme for stac and CaM modulation. (1) Ca$_V$1.3$_S$ devoid of CaM and stac possess a low baseline P_O ($P_{O/E}$) (2) Without stac, apoCaM binding to Ca$_V$1.3$_S$ upregulates baseline P_O ($P_{O/A}$). Baseline P_O of Ca$_V$1.3$_S$ bound to stac in the absence (configuration 3) and the presence of apoCaM (configuration 4) are unknown.
(B) Schematic outline three mechanistic possibilities for stac binding to Ca$_V$1 and their functional outcomes. Scenario 1, stac uniformly suppresses P_O of Ca$_V$1 ($P_{O/E}$) and abolishes CDI. Scenario 2, apoCaM tunes baseline P_O of Ca$_V$1 despite concurrent stac binding. Stac, nonetheless, abrogates CDI. Scenario 3, stac uniformly upregulates the baseline P_O of Ca$_V$1 and abolishes CDI ($P_{O/A}$).
(C) Cartoon shows the canonical Ca$_V$1.3$_S$ variant with a high apoCaM binding affinity. Single-channel analysis of recombinant Ca$_V$1.3$_S$ in the absence (left) and presence of stac (right). In both panels, the unitary Ba^{2+} currents during voltage-ramp shown between -50 mV and + 40 mV (slanted gray lines, GHK fit). Robust Ca$_V$1.3 openings are detected in the absence and presence of stac.
(D) Average single-channel P_O-voltage relationship for Ca$_V$1.3$_S$ obtained from multiple patches in the absence (gray) and presence of stac (blue). Error bars indicate ± SEM for specified number of patches and 100 – 150 stochastic records per patch.
(E) Histogram shows distribution of single-trial average P_O ($\bar{P}_O$) for the voltage-range $-30 \text{ mV} \leq V \leq +25 \text{ mV}$ under control (top), stac-bound (middle), and CaM-bound (bottom) conditions. Absent stac, $\bar{P}_O$-distribution is bimodal in the absence of stac corresponding to high P_O (gray) and low P_O (rose) gating modes. With Stac, $\bar{P}_O$-distribution largely restricted to the high P_O mode.
(F – H) Single-channel analysis of recombinant Ca$_V$1.3$_{\text{RNA-edited}}$ variant reveals a marked upregulation in the baseline P_O consistent in the presence of stac compared to control condition where apoCaM preassociation is weak. Absent stac or CaM, single-trail $\bar{P}_O$-distribution is restricted to the low P_O limits, In the presence of stac and CaM, the high PO gating mode re-emerges. Format as in panels C – E.
(I – K) Stac also upregulates the baseline P_O of Ca$_V$1.3$_L$ alternatively-spliced variant by stabilizing the high P_O gating configuration. Format as in panels C – E.

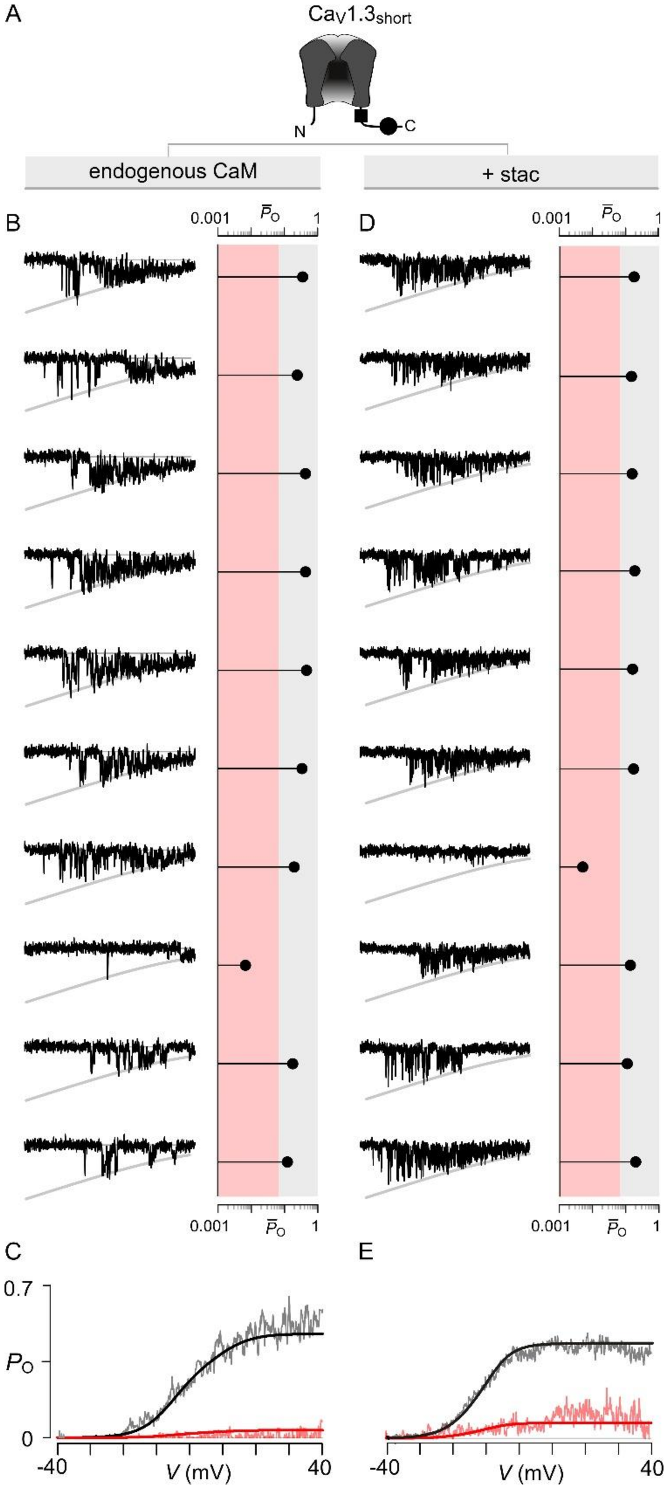

Figure 4.8. Stac2 preferentially biases a high P_O gating mode for Ca$_V$1.3.
(A) Cartoon schematizes Ca$_V$1.3$_S$.
(B) Left, ten sequential single-channel trials of Ca$_V$1.3$_S$ under endogenous levels of CaM illustrate high P_O gating mode with rare sojourns into a low P_O gating mode. Here, traces show Ba^{2+} currents elicited every 10 sec in response to a voltage ramp shown between -40 mV to +40 mV. Right,

Diary plot displays single trial average P_O computed for the voltage-range -30 mV ≤ V ≤ +25 mV ($\bar{P}_O$(-30 ≤ V ≤ 25)). Dashed line discriminates traces to low P_O (red shaded area) or high P_O (gray shaded area) categories as previously established.
(C) Average P_O at each voltage calculated for all traces within the high P_O range (gray region in panel B) and the low P_O range (red shaded region in panel B). These relationships estimate the P_O-V relationship for high P_O and low P_O gating modes.
(D – E) In the presence of stac2, $Ca_V1.3_S$ preferentially adopts the high P_O gating configuration. Format as in panels B – C.

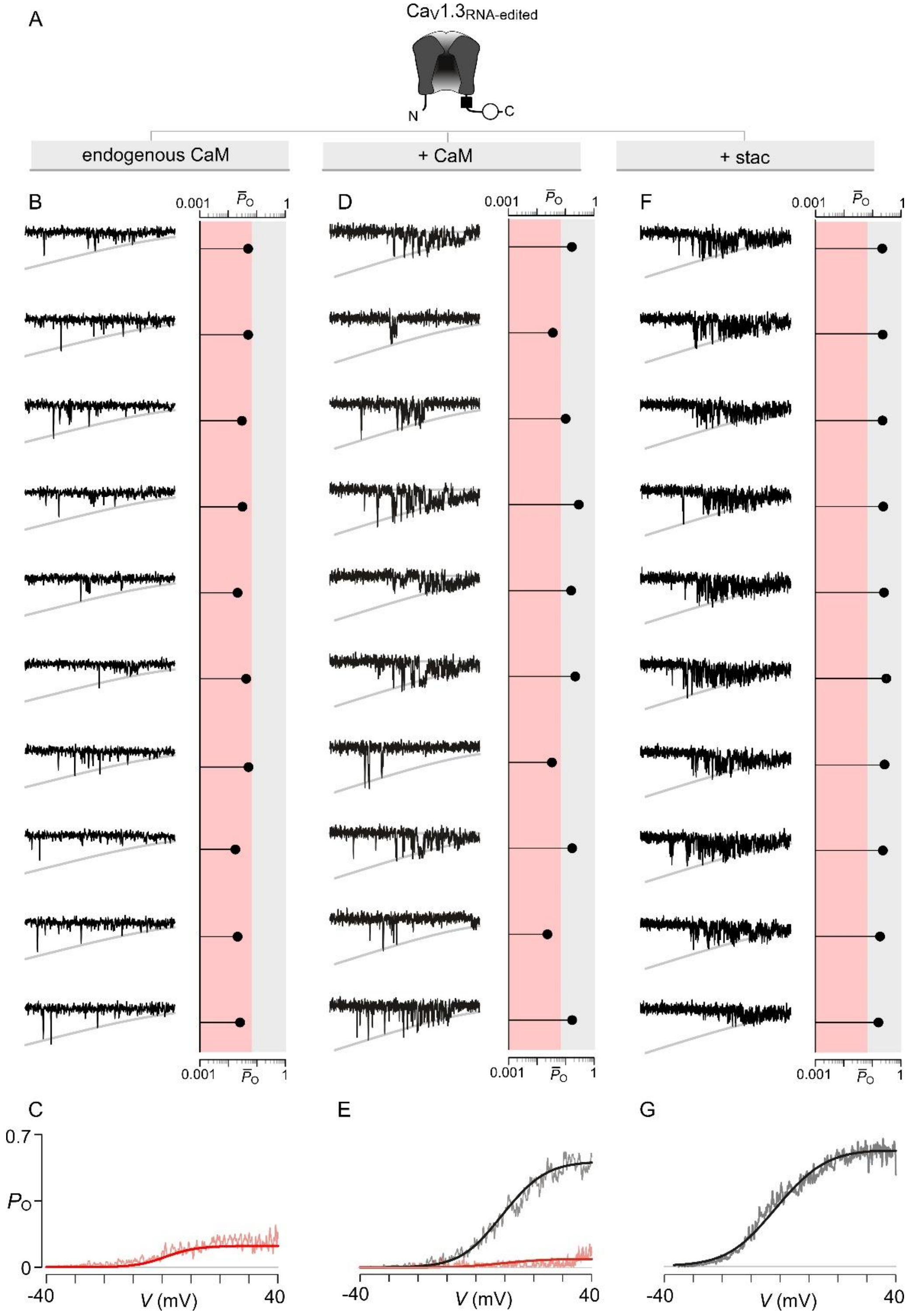

Figure 4.9. Stac2 and CaM enhances the P_O of Ca$_V$1.3$_{\text{RNA-edited}}$ variant via discreet transitions into a high P_O gating mode.

(A) Cartoon schematizes Ca$_V$1.3$_{\text{RNA-edited}}$. RNA-editing results in a methionine substitution of the central isoleuicine residue, resulting in sharply diminished CaM binding. Functionally, CaM binding enhances the P_O of Ca$_V$1.3$_{\text{RNA-edited}}$.

(B – C) Under endogenous levels of CaM, $\mathrm{Ca_V1.3_{RNA\text{-}edited}}$ exhibits a uniformly low P_O as evident from individual trials. The average P_O – V relation is consistent with that for the low $\mathrm{P_O}$ gating mode. Format as in Figure 4.8B-C.

(D – E) CaM over-expression enhances the P_O of $\mathrm{Ca_V1.3_{RNA\text{-}edited}}$ variant. Format as in Figure 4.8B-C. Exemplar traces depict channels switching between discrete high and low P_O gating modes. P_O-V relationship for high P_O and low P_O gating modes are evident.

(F – G) Similar to CaM, stac2 over-expression also enhances the P_O of $\mathrm{Ca_V1.3_{RNA\text{-}edited}}$ variant by stabilizing the high P_O gating mode. Format as in Figure 4.8B-C. Exemplar traces depict channels largely adopting the high gating mode.

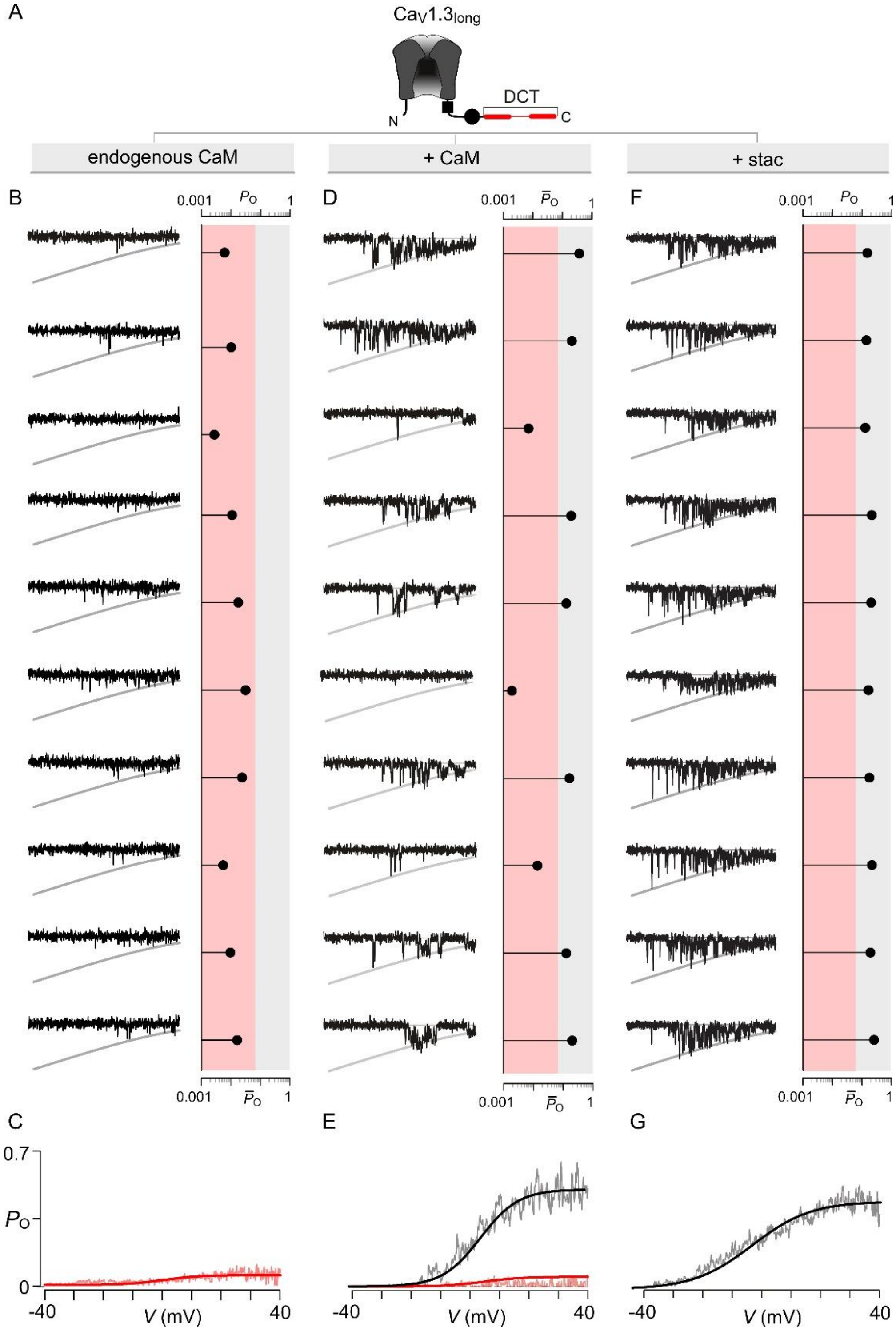

Figure 4.10. Stac2 and CaM enhances the P_O of $Ca_V1.3_L$ variant.
(A) Cartoon schematizes $Ca_V1.3_L$. The long-splice variant includes a distal carboxy-tail (DCT) that interacts with the IQ domain and competitively displaces CaM.

(B – C) Under endogenous levels of CaM, $\mathrm{Ca_V}1.3_\mathrm{L}$ exhibits a uniformly low P_O as evident from individual trials. Format as in Figure 4.8B-C. The average $P_\mathrm{O} - V$ relation is consistent with that for the low P_O gating mode.

(D – E) CaM over-expression enhances the P_O of $\mathrm{Ca_V}1.3_\mathrm{L}$ variant. Format as in Figure 4.8B-C. Exemplar traces depict channels switching between discrete high and low P_O gating modes.

(F – G) Similar to CaM, stac2 over-expression also enhances the P_O of $\mathrm{Ca_V}1.3_\mathrm{L}$ variant by stabilizing the high P_O gating mode. Format as in Figure 4.8B-C. Exemplar traces depict channels largely adopting the high gating mode.

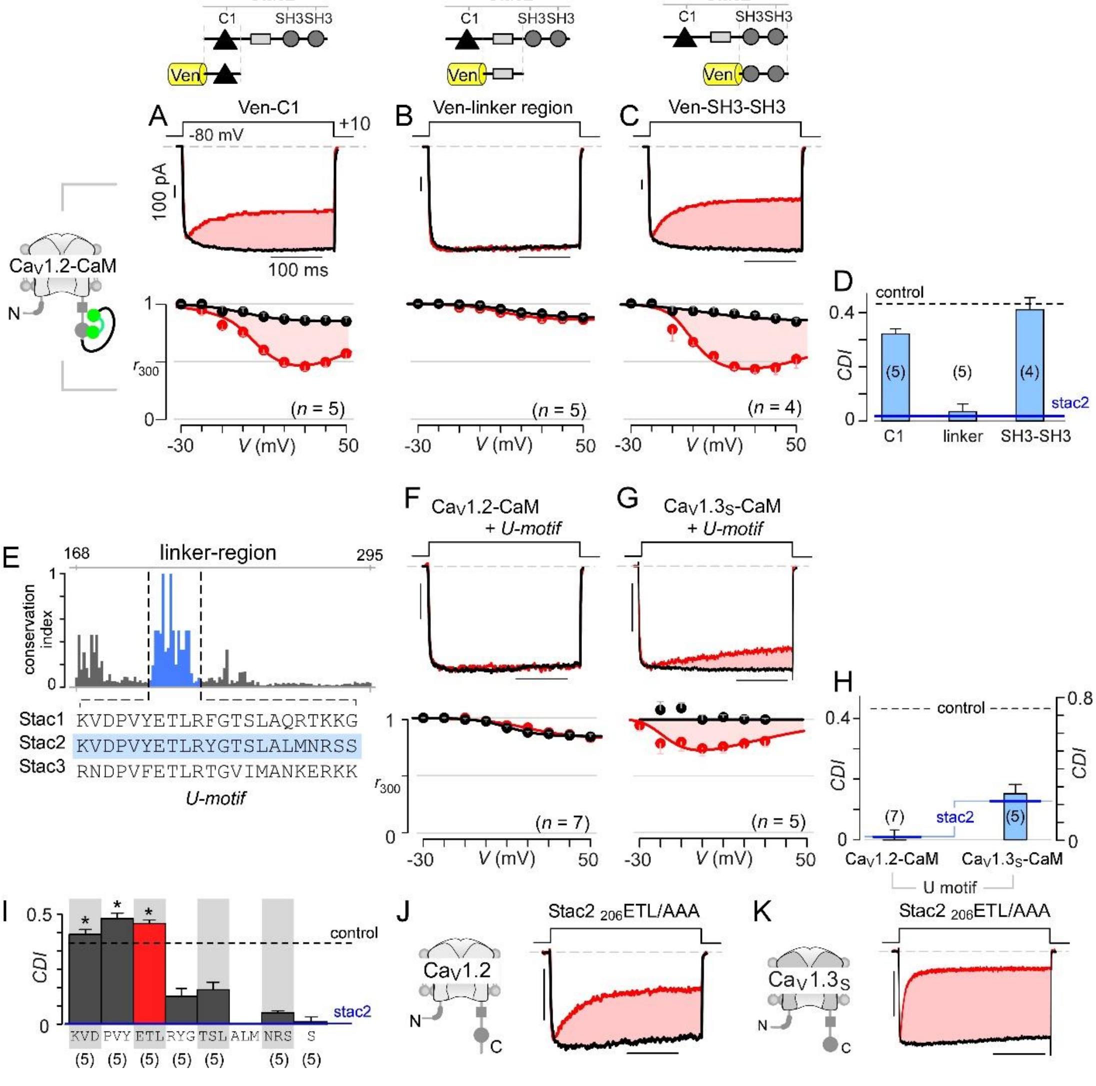

Figure 4.11. Stac U-domain is a minimal effect domain for suppression of $\mathrm{Ca_V}1$ CDI.

(A – C) To localize an effector motif for stac2, CDI of $\mathrm{Ca_V}1.2$-CaM was quantified in the presence of three stac subdomains: (1) C1, (2) linker region, and (3) SH3-SH3. Exemplar traces in response to a +10 mV voltage-step depolarization show robust CDI of $\mathrm{Ca_V}1.2$-CaM in the presence of C1 (panel A), and SH3-SH3 (panel C) domains. Coexpression of the linker-region is sufficient to suppress CDI of $\mathrm{Ca_V}1.2$.-CaM (panel B). Format as in Figure 4.2A-C.

(D) Bar graph summarizes population data for $\mathrm{Ca_V}1.2$-CaM CDI in the presence of the three stac subdomains. Each bar, mean ± s.e.m of CDI_{300} at +10 mV from specified number of cells. CDI levels in the presence (solid blue line) and absence (dashed grey line) of full length stac2 is reproduced for comparison.

(E) Bar graph shows degree of conservation for the linker region across 750 orthologs of stac2. A well conserved subsegment termed U-domain is shaded blue.

(F–G) Co-expression of U-domain is sufficient to abolish CDI of $\mathrm{Ca_V}$1.2-CaM (panel F) and $\mathrm{Ca_V}$1.3-CaM (panel G). Format as in Figure 4.2A.

(H) Bar graph displays population data for CDI of $\mathrm{Ca_V}$1.2-CaM and $\mathrm{Ca_V}$1.3-CaM in the presence of U-domain. Each bar, mean ± s.e.m of CDI_{300} at +10 mV from specified number of cells. Dashed line, baseline CDI for both channels in the absence of stac2. Blue line, CDI of both channels in the presence of full length stac2.

(I) Systematic alanine scanning mutagenesis of the U-domain reveals critical determinants for stac mediated suppression of $\mathrm{Ca_V}$1.2 CDI. For comparison, $\mathrm{Ca_V}$1.2 CDI in the presence (blue line) and absence (black dashed line) of stac2 are shown. Stac2 mutants $_{200}$KVD/AAA, $_{203}$PVY/AAA, $_{206}$ETL/AAA fully abolish stac2-mediated CDI suppression.

(J) Exemplar currents show that stac2 mutant $_{206}$ETL/AAA eliminates stac's ability to suppress $\mathrm{Ca_V}$1.2 CDI. Format as in Figure 4.2A.

(K) Stac2 $_{206}$ETL/AAA also fails to inhibit CDI of $\mathrm{Ca_V}1.3_S$. Format as in Figure 4.2A.

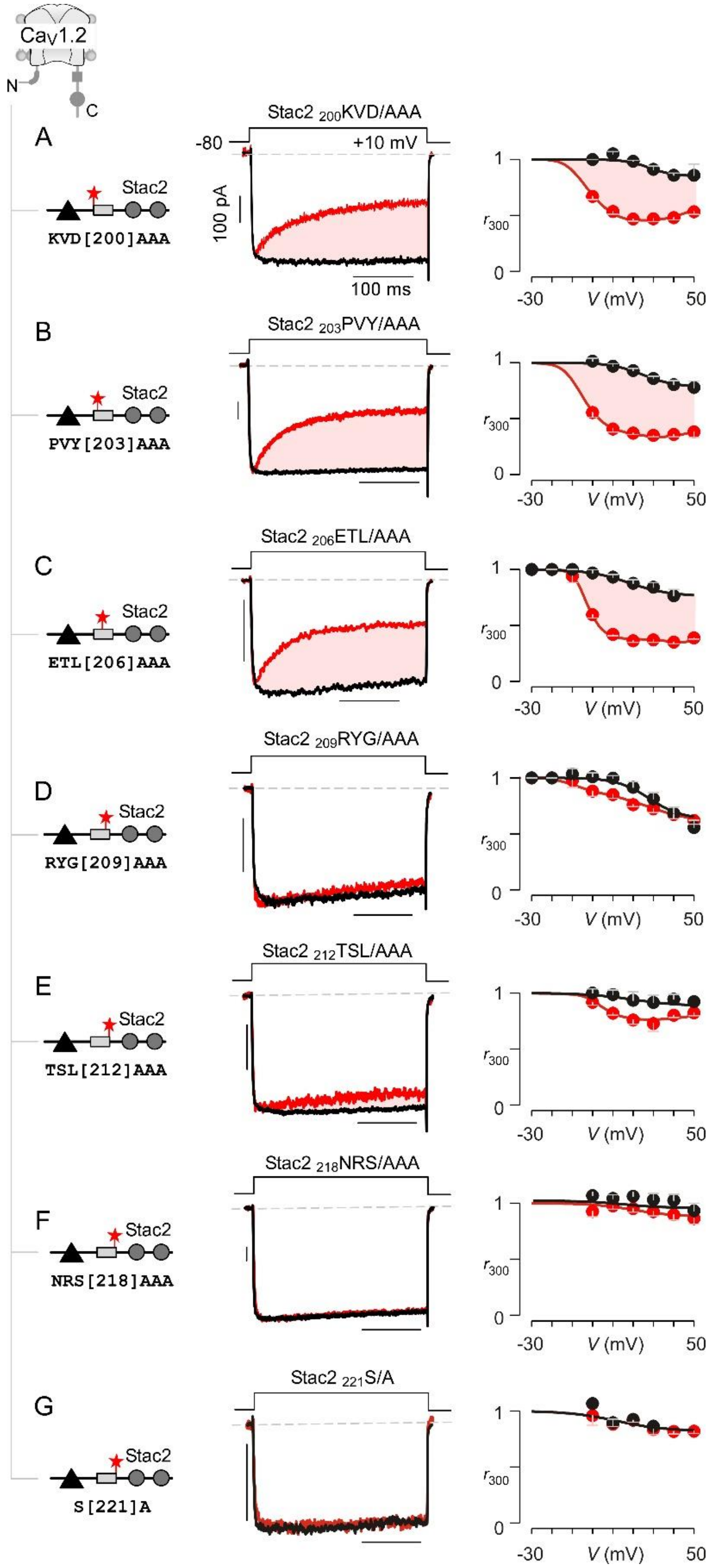

Figure 4.12. Systematic alanine scanning mutagenesis of minimal U-motif reveals structural determinants for stac modulation of Ca_V1.

(A) Triple alanine substitution of residues $_{200}$KVD$_{202}$ abolishes stac modulation of Ca$_V$1.2. In comparison to stac2 that fully suppresses CDI of Ca$_V$1.2, co-expression of stac2 $_{200}$KVD/AAA spares strong CDI of Ca$_V$1.2 suggesting that residues $_{200}$KVD$_{202}$ is critical for stac modulation. Left, cartoon schematizes the location of $_{200}$KVD/AAA mutation on full length stac2. Middle, exemplar current traces show robust CDI of Ca$_V$1.2 in the presence of stac2 $_{200}$KVD/AAA. Right, population data showing r_{300} values as a function of voltage for Ca^{2+} (red) and Ba^{2+} currents (black). Each symbol, mean ± SEM from 5 cells.

(B – C) Triple alanine substitution of stac2 residues $_{203}$PVY$_{205}$ and $_{206}$ETL$_{208}$ abolishes stac modulation of Ca$_V$1.2 as evident from strong CDI present despite overexpression of mutant stac. Format as in panel A.

(D – G) Ca$_V$1.2 CDI is suppressed by stac2 despite alanine substitution of residues, $_{209}$RYG$_{211}$ (panel D), $_{212}$TSL$_{214}$ (panel E), $_{218}$NRS$_{220}$ (panel F), and $_{221}$S (panel G) suggesting that these residues are not necessary for stac modulation of Ca$_V$1 channels. Format as in panel A.

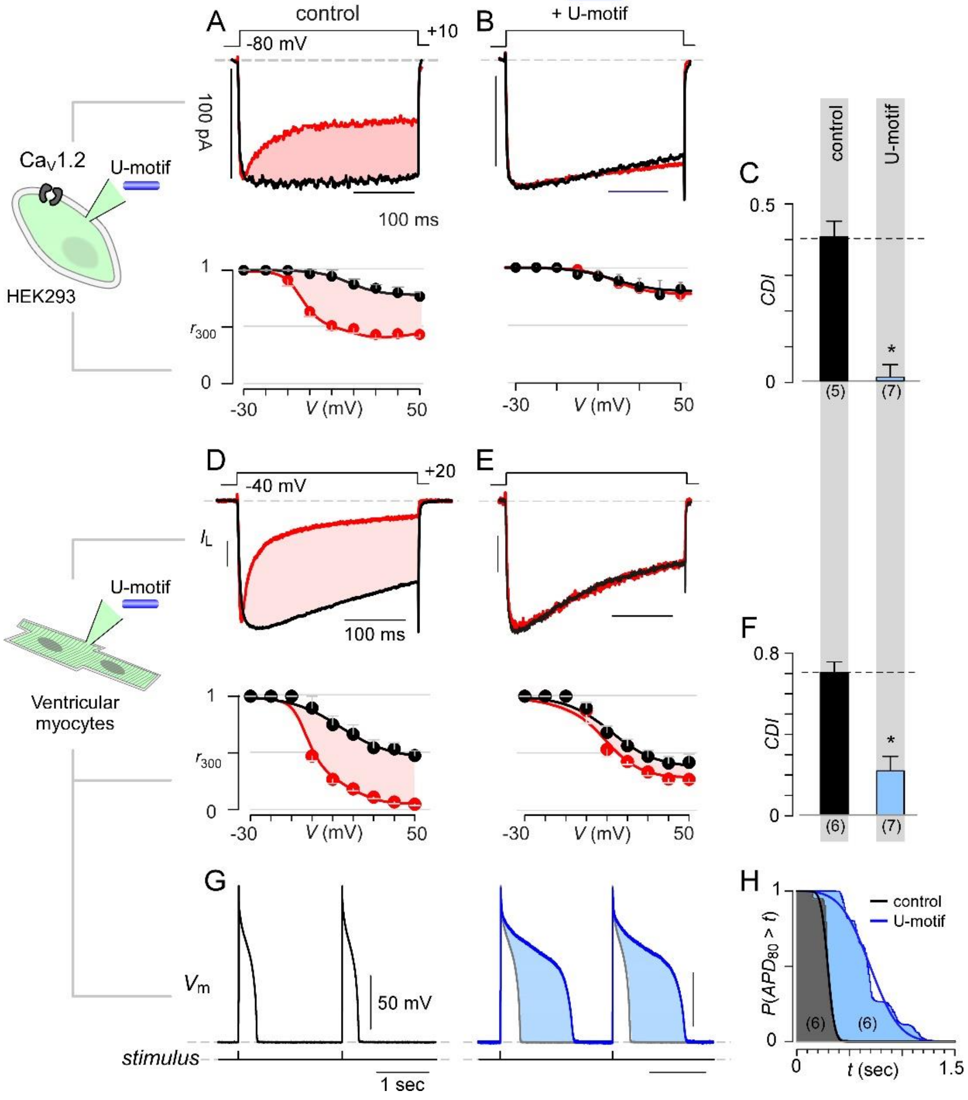

Figure 4.13. Synthetic U-domain peptide is sufficient for physiological perturbations.

(A) Schematic illustrates pipet dialysis of custom synthesized U-domain peptide in $Ca_V1.2$ heterologously expressed in HEK293 cells, a strategy that emulates acute elevation of cytosolic stac2 levels.

(B – C) Exemplar traces and population data confirms that pipet dialysis of U-domain suppresses CDI of recombinant $Ca_V1.2$ in HEK293 cells. Format as in Figure 2A and 2B.

(D – F) Pipet dialysis of U-domain abolishes CDI of endogenous L-type current in freshly dissociated ventricular myocytes from adult guinea pigs as evident from exemplar traces and bar graph summary of population data. To eliminate T-type current, the cells were depolarized to -40 mV for a period of 100 ms. Format as in Figures 2A and 2B.

(G) Exemplar action potential traces of aGPVMs paced at 0.5 Hz with (blue) and without (black) 0.5 μM U-domain in the internal solution. In the presence of U-domain, the action potentials are markedly prolonged (blue shaded area) consistent with a loss of CDI of native L-type current.

(H) Complement of cumulative distribution ($P(APD_{80} > t)$ of action potential durations (APD_{80}) obtained in the presence (blue) and absence (black) of U-domain in the internal solution.

CHAPTER 5

Conclusions

In the previous chapters, we presented a new understanding of stac proteins in regulating trafficking and gating of L-type Ca^{2+} channels. More specifically, we explained multiple missing puzzle pieces for understanding $Ca_V1.1$ and show that it is not as different from other members of the Ca_V1 family as originally perceived. In particular, we show that CaM and stac act independently to increase channel trafficking as well as P_O while exploring treatments for stac-associated congenital myopathies. Additionally, we expanded the understanding of Ca_V1 regulation by stac proteins and may now add a new class of auxiliary proteins to our general knowledge of ion channels known as selective allosteric regulators.

The prodigal child returns home – Although $Ca_V1.1$ was one of the first voltage-gated Ca^{2+} channels cloned from the genome (Tanabe et al., 1987), it was still viewed as "different" because many were unable to interrogate its biophysical properties reliably in heterologous systems. While general assumptions held this to be a result of a decrease in trafficking, it was difficult to determine the validity of this postulation as there are no dependable antibodies for visualizing these channels on the cell membrane. Similarly, CaM regulation of $Ca_V1.1$ evaded consensus for many decades as there was no easy method to probe this phenomenom. While exogenously expressed CaM localizes to the skeletal muscle triad (Rodney and Schneider, 2003), CaM interaction with $Ca_V1.1$ has been controversial in biochemical studies. Some report weak to no binding (Ohrtman et al., 2008), while *in vitro* surface plasmon resonance measurements and crystallographic analysis suggest a high-affinity interaction with the channel carboxy-tail (CT) in the presence of Ca^{2+} (Black et al., 2005; Halling et al., 2009; Sencer et al., 2001). Similarly, functional analysis of Ca$_V$1.1 in skeletal myotubes revealed ultra-slow and variable extent of CDI casting doubt as to whether CaM is relevant for Ca$_V$1.1 function (Ohrtman et al., 2008; Stroffekova, 2008; Tanabe et al., 1990b) while mutations of the CaM binding interface in the Ca$_V$1.1 CT strongly reduce EC-coupling despite the presence of gating charge movements (Stroffekova, 2011).

Using external-epitope labeling, it is possible to see that Ca$_V$1.1 does indeed traffic to the plasma membrane though at a slower rate (Figure 3.2I-J). It is also possible to collect electrophysiological data from these channels when channel trafficking appears to plateau on the second day (Figure 3.4A). While stac does enhance channel trafficking by four- to five-fold (Figure 3.2J), it also enhances gating by approximately five-fold (Figure 3.4O). This enhancement in gating makes electrophysiology much easier while channel trafficking is most likely more important for the physiological function of skeletal muscle contraction as the influx of Ca^{2+} is not necessary for muscle twitches (Armstrong et al., 1972; Dayal et al., 2017).

Furthermore, CaM regulation of Ca$_V$1.1 may not be as different as originally thought. For nearly all Ca$_V$1 and Ca$_V$2 channels, CaM confers a potent feedback mechanism (Ben-Johny et al., 2015; Halling et al., 2006; Minor and Findeisen, 2010). Our analysis shows that local enrichment of CaM to Ca$_V$1.1 also results in a 5-fold increase in maximal P_O (Figure 3.4K). As potentiation in gating occurs at high-voltages where channels convey minimal Ca^{2+}-influx, this effect likely depends on apoCaM interaction. Excitingly, these results are evocative of recent findings that apoCaM binding augments the baseline P_O of Ca$_V$1.3 variants (Adams et al., 2014) hinting at a conserved mechanism across the Ca$_V$ superfamily (Ben-Johny et al., 2015). Of note, effects on channel gating and trafficking were both elicited by CaM fused to β-subunit. As β-subunits have a 1:1 stoichiometry with the α-subunit (Dalton et al., 2005; Wu et al., 2016), a single CaM mediates both functional effects. Thus, CaM signaling may be bifurcated whereby the apo-form enhances channel gating while the Ca^{2+}-bound form enriches channels at the plasma membrane.

Other studies on an embryonic splice variant have also shown that due to the long linker between the S3-S4 transmembrane segments of domain IV, $Ca_V1.1$ currents are much smaller and possess slower activation kinetics (Tuluc and Flucher, 2011; Tuluc et al., 2009). Intriguingly, chimeras of $Ca_V1.3$ with $Ca_V1.1$ CI ($Ca_V1.3$-$Ca_V1.1$ CI) display robust CDI while the addition of stac abolishes this CDI (Figure 5.1). Altogether, these results suggest that CaM does interact with $Ca_V1.1$ in a fashion similar to other Ca_V channels. Instead, the observed differences in biophysical properties may be a result of an evolutionary lack of need for Ca^{2+} signaling to RyR1 and an emphasis on fine-tuning channel conformational changes propagated to RyR1 in response to neuronal firing.

Towards pathophysiology and treatment of myopathy-associated stac mutants – While stac3 is implicated in the biophysical properties of $Ca_V1.1$, it has been pathophysiologically identified as a vital genetic locus for a debilitating congenital myopathy that encompasses an expanding list of mutations. Patients exhibit a plethora of myopathy associated symptoms including facial weakness with ptosis, hypotonia, small stature, scoliosis, cleft palate, and susceptibility to malignant hyperthermia (Grzybowski et al., 2017; Stamm et al., 2008; Telegrafi et al., 2017; Zaharieva et al., 2014). Current treatment strategies focus on early diagnosis and symptom management particularly anticipatory management of malignant hyperthermia. Novel small molecule agents that reverse pathogenesis are highly desired.

Our analysis reveals that disease-associated stac3 variants weaken binding to the CT resulting in variably diminished $Ca_V1.1$ surface-membrane trafficking, highlighting potential pathogenic mechanisms. Indeed, reconstitution of myopathy-associated mutant stac3 (W[284]S) in stac3$^{-/-}$ knockout zebrafish and mouse models led to diminished trafficking, triadic organization, and activity of $Ca_V1.1$ resulting in marked loss of EC coupling (Linsley et al., 2017a; Linsley et al., 2017b; Polster et al., 2016). As patients are either homozygous or compound heterozygous for stac mutations, it is likely that the weakened affinity of stac3 for $Ca_V1.1$ CT results in incomplete saturation of $Ca_V1.1$ by this regulatory protein. Our findings point to three distinct avenues for developing effective pharmacological strategies. First, given that CaM can both partially rescue reduced $Ca_V1.1$ trafficking and can enhance $Ca_V1.1$ activation gating, local enrichment of CaM may be an effective strategy for reversing the pathophysiology of stac3-associated myopathies. In this regard, a CRISPR-interference approach was recently developed to selectively manipulate CaM expression for a subset of cardiac arrhythmogenic long-QT syndrome (Limpitikul et al., 2017). Second, as we identify $Ca_V1.1$ CT as the primary effector interface for stac3, FRET 2-hybrid binding assay may be repurposed to devise high-throughput screens for small-molecule modulators that enhance this interaction and tune skeletal muscle function (Janzen, 2014). Third, more tangibly, our findings demonstrate that certain Ca_V channel antagonists such as diltiazem and verapamil may partially rescue these trafficking defects although this effect is contingent upon continual exposure to the drug. Diltiazem and verapamil are clinically prescribed for various diseases and symptoms including hypertension, arrhythmias, angina, and cluster headaches. Side-effects observed include headaches, hypotension, gingival hyperplasia, constipation, and edema. Consequently, we show that low therapeutic plasma concentration is sufficient for strikingly enhanced surface-membrane trafficking of $Ca_V1.1$ and gating charge movement remains unimpaired. Fortunately, as EC coupling in skeletal muscle does not depend on freely-diffusing Ca^{2+} ions, blockade of Ca^{2+}-influx resulting from Ca_V antagonists may not significantly alter the strength of EC coupling (Dayal et al., 2017). In fact, recent studies have shown that verapamil can paradoxically potentiate contractions in mouse skeletal muscle (Dayal et al., 2017). Accordingly, verapamil, diltiazem, or related small-molecules may hold therapeutic potential and our quantitative flow-cytometric assay promises to aid the discovery of such trafficking modulators. Indeed, similar pharmacological chaperones have emerged as a potential therapeutic avenue for rescue of trafficking deficits associated with cystic fibrosis (Hanrahan et al., 2013), congenital hyperinsulinism of infancy (Martin et al., 2013), and Brugada syndrome (Moreau et al., 2012; Valdivia et al., 2004).

Advent of selective allosteric regulators – After we demonstrated stac's ability to increase P_O of Ca$_V$1.1, we found that stac exerts the same effect on all members of the Ca$_V$1 family. Remarkably, stac is able to selectively distinguish between Ca$_V$1 and Ca$_V$2 members as well as Na$_V$1.4, which share much sequence homology in their CI regions. As it turns out, hints of this idea of allosterically regulating ion channels may have begun many years ago. We mentioned previous work on CABPs and their mixed allostery model (Yang et al., 2014b). Similar to stac, CABPs bind to the upstream preIQ region of the CI and selectively suppress CDI of Ca$_V$1 compared to Ca$_V$2. In fact, another structurally unrelated protein, fibroblast growth factor homologous factors (fhf), interacts with the Na$_V$ CI module in close proximity to the CaM binding interface suggesting interplay between these modulatory agents (Wang et al., 2012; Wang et al., 2011). Like stac and Ca$_V$1, fhf may override CaM-dependent changes to Na$_V$. Indeed, we have found that while fhf abolishes CDI of Na$_V$1.4, it does not perturb CDI of Ca$_V$1 (data not shown).

Given these similarities in mechanism, we can now harness the parallel nature of allosteric regulation of Na$_V$1.4 by fhf and Ca$_V$1 by stac to glean a structural understanding. Crystal structures show that CaM undergoes a profound Ca^{2+}-dependent rearrangement even when fhf binds to the CI of Na$_V$1.4 (Wang et al., 2012; Wang et al., 2014) suggesting that fhf does not explicitly prevent either Ca^{2+} binding to CaM or Ca^{2+}/CaM interaction with effector interfaces (Gabelli et al., 2014; Wang et al., 2012) (Figure 5.2A). In addition, as both structures of the preIQ region are available for Ca$_V$1.1 and Na$_V$1.4, we can overlay them to reveal structural differences. Fascinatingly, it becomes apparent that the preIQ region of Ca$_V$1.1 is dramatically different from Na$_V$1.4 and is sterically incompatible for fhf docking (Figure 5.2B-D). This allosteric mechanism may constitute an orthogonal dimension by selectively abolishing Ca^{2+}-feedback to ion channels (Figure 5.3).

Beyond natural mechanisms that tune CaM signaling, these results also hint at the possibility of engineering synthetic regulatory pathways that specifically shunt Ca^{2+}-signaling. With these distinct structural binding interfaces, emerging protein engineering methods may be used to attain synthetic modulation of related ion channel families especially in segments possessing less sequence homology. Indeed, we have found that custom allosteric sites may be engineered into preIQ segments (data not shown). Thus, a specialized library of synthetic regulators may be developed to combinatorially modify kinetic properties of Ca$_V$1 and Ca$_V$2 channels with spatiotemporal specificity.

In all, this work unveils stac as a novel regulator of Ca$_V$1 CaM feedback and proposes that generalizing this allosteric mechanism to other targets may lead to the development of new tools that ultimately rewire the signaling networks which decode and interpret complex Ca^{2+} signals.

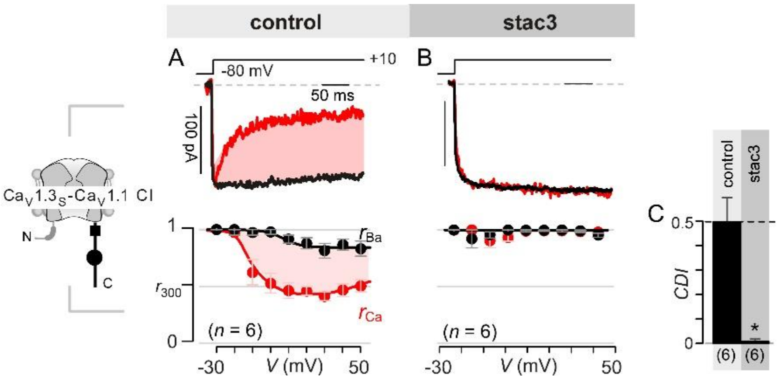

Figure 5.1. Ca^{2+}-CaM and stac regulation is preserved in $Ca_V1.1$ CI.
(A-C) Stac3 abolishes CDI of $Ca_V1.3_S$-$Ca_V1.1$ CI chimera. Format as in Figure 4.1A, C, and E respectively.

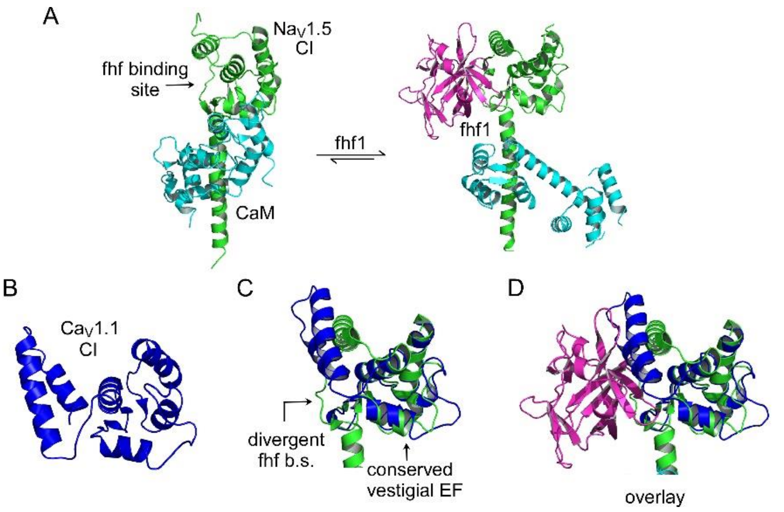

Figure 5.2. Structure insights on specificity of allosteric mechanism to abrogate Ca^{2+}-feedback.
(A) Structural comparison of $Na_V1.5$ CI (green) in the presence of CaM alone (cyan, left) or both CaM (cyan) and fhf1b (purple). Fhf binding changes baseline conformation of CaM on Na_V1 CI.
(B) Structure of $Ca_V1.1$ upstream CI elements (blue) composed of dual vestigial EF hands and preIQ segments isolated from cryo-EM structure of $Ca_V1.1$ (PDBID, 5GJV). This domain is primary interface for stac interaction in the Ca_V1 CI.
(C) Structural overlay of upstream CI elements of $Ca_V1.1$ (PDBID, 5GJV) and $Na_V1.5$ (PDBID, 4DCK) shows a highly conserved dual vestigial EF hand segments while the fhf binding site is structurally divergent.
(D) The divergence in the fhf binding interface in $Ca_V1.1$ in comparison to $Na_V1.5$ would introduce a steric clash that prohibits fhf binding to Ca_V channels.

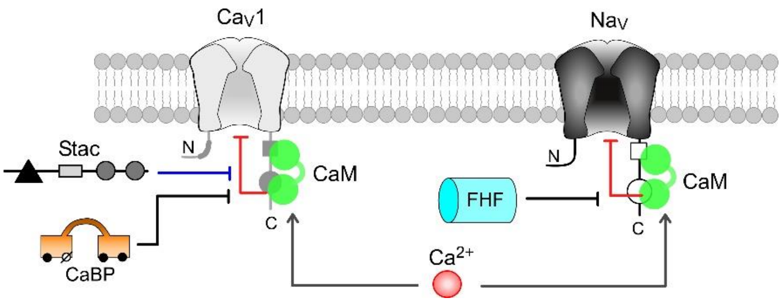

Figure 5.3. Cartoon summarizes selective modulation of Ca^{2+}/CaM signaling to Ca_V1, and Na_V1 channels with CaM, stac, and fhf.

Adams, P.J., Ben-Johny, M., Dick, I.E., Inoue, T., and Yue, D.T. (2014). Apocalmodulin itself promotes ion channel opening and ca(2+) regulation. Cell *159*, 608-622.

Adams, P.J., Rungta, R.L., Garcia, E., van den Maagdenberg, A.M., MacVicar, B.A., and Snutch, T.P. (2010). Contribution of calcium-dependent facilitation to synaptic plasticity revealed by migraine mutations in the P/Q-type calcium channel. Proc Natl Acad Sci U S A *107*, 18694-18699.

Adams, P.J., and Snutch, T.P. (2007). Calcium channelopathies: voltage-gated calcium channels. Subcell Biochem *45*, 215-251.

Akiyama, K., Liang, Y.Q., Isono, M., and Kato, N. (2015). Investigation of Functional Genes at Homologous Loci Identified Based on Genome-wide Association Studies of Blood Lipids via High-fat Diet Intervention in Rats using an in vivo Approach. Journal of atherosclerosis and thrombosis *22*, 455-480.

Alseikhan, B.A., DeMaria, C.D., Colecraft, H.M., and Yue, D.T. (2002). Engineered calmodulins reveal the unexpected eminence of Ca^{2+} channel inactivation in controlling heart excitation. Proc Natl Acad Sci U S A *99*, 17185-17190.

Anderson, A.A., Altafaj, X., Zheng, Z., Wang, Z.M., Delbono, O., Ronjat, M., Treves, S., and Zorzato, F. (2006). The junctional SR protein JP-45 affects the functional expression of the voltage-dependent Ca2+ channel Cav1.1. J Cell Sci *119*, 2145-2155.

Armstrong, C.M., Bezanilla, F.M., and Horowicz, P. (1972). Twitches in the presence of ethylene glycol bis(-aminoethyl ether)-N,N'-tetracetic acid. Biochim Biophys Acta *267*, 605-608.

Avila, G., and Dirksen, R.T. (2000). Functional impact of the ryanodine receptor on the skeletal muscle L-type Ca(2+) channel. J Gen Physiol *115*, 467-480.

Babitch, J. (1990). Channel hands. Nature *346*, 321-322.

Bannister, R.A., and Beam, K.G. (2013). Ca(V)1.1: The atypical prototypical voltage-gated Ca(2)(+) channel. Biochim Biophys Acta *1828*, 1587-1597.

Bannister, R.A., Sheridan, D.C., and Beam, K.G. (2016). Distinct Components of Retrograde Ca(V)1.1-RyR1 Coupling Revealed by a Lethal Mutation in RyR1. Biophys J *110*, 912-921.

Bazzazi, H., Ben-Johny, M., Adams, P.J., Soong, T.W., and Yue, D.T. (2013). Continuously tunable Ca(2+) regulation of RNA-edited CaV1.3 channels. Cell Rep *5*, 367-377.

Beerepoot, P., Nazari, R., and Salahpour, A. (2017). Pharmacological chaperone approaches for rescuing GPCR mutants: Current state, challenges, and screening strategies. Pharmacol Res *117*, 242-251.

Ben-Johny, M., Dick, I.E., Sang, L., Limpitikul, W.B., Kang, P.W., Niu, J., Banerjee, R., Yang, W., Babich, J.S., Issa, J.B., *et al.* (2015). Towards a Unified Theory of Calmodulin Regulation

(Calmodulation) of Voltage-Gated Calcium and Sodium Channels. Curr Mol Pharmacol *8*, 188-205.

Ben-Johny, M., Yang, P.S., Niu, J., Yang, W., Joshi-Mukherjee, R., and Yue, D.T. (2014). Conservation of Ca2+/calmodulin regulation across Na and Ca2+ channels. Cell *157*, 1657-1670.

Ben Johny, M., Yang, P.S., Bazzazi, H., and Yue, D.T. (2013). Dynamic switching of calmodulin interactions underlies Ca2+ regulation of CaV1.3 channels. Nat Commun *4*, 1717.

Berridge, M.J., Lipp, P., and Bootman, M.D. (2000). The versatility and universality of calcium signalling. Nat Rev Mol Cell Biol *1*, 11-21.

Black, D.J., Halling, D.B., Mandich, D.V., Pedersen, S.E., Altschuld, R.A., and Hamilton, S.L. (2005). Calmodulin interactions with IQ peptides from voltage-dependent calcium channels. Am J Physiol Cell Physiol *288*, C669-676.

Bock, G., Gebhart, M., Scharinger, A., Jangsangthong, W., Busquet, P., Poggiani, C., Sartori, S., Mangoni, M.E., Sinnegger-Brauns, M.J., Herzig, S., *et al.* (2011). Functional properties of a newly identified C-terminal splice variant of Cav1.3 L-type Ca2+ channels. J Biol Chem *286*, 42736-42748.

Buraei, Z., and Yang, J. (2010). The ss subunit of voltage-gated Ca2+ channels. Physiol Rev *90*, 1461-1506.

Cai, T., Jen, H.I., Kang, H., Klisch, T.J., Zoghbi, H.Y., and Groves, A.K. (2015). Characterization of the transcriptome of nascent hair cells and identification of direct targets of the Atoh1 transcription factor. J Neurosci *35*, 5870-5883.

Campiglio, M., and Flucher, B.E. (2017). STAC3 stably interacts through its C1 domain with CaV1.1 in skeletal muscle triads. Sci Rep *7*, 41003.

Cannon, S.C. (2015). Channelopathies of skeletal muscle excitability. Compr Physiol *5*, 761-790.

Carafoli, E., and Krebs, J. (2016). Why Calcium? How Calcium Became the Best Communicator. J Biol Chem *291*, 20849-20857.

Catterall, W.A. (2000). Structure and regulation of voltage-gated Ca2+ channels. Annu Rev Cell Dev Biol *16*, 521-555.

Catterall, W.A., Wisedchaisri, G., and Zheng, N. (2017). The chemical basis for electrical signaling. Nat Chem Biol *13*, 455-463.

Chan, C.S., Guzman, J.N., Ilijic, E., Mercer, J.N., Rick, C., Tkatch, T., Meredith, G.E., and Surmeier, D.J. (2007). 'Rejuvenation' protects neurons in mouse models of Parkinson's disease. Nature *447*, 1081-1086.

Clapham, D.E. (2007). Calcium signaling. Cell *131*, 1047-1058.

Cohen, G.B., Ren, R., and Baltimore, D. (1995). Modular binding domains in signal transduction proteins. Cell *80*, 237-248.

Colon-Gonzalez, F., and Kazanietz, M.G. (2006). C1 domains exposed: from diacylglycerol binding to protein-protein interactions. Biochim Biophys Acta *1761*, 827-837.

Dalton, S., Takahashi, S.X., Miriyala, J., and Colecraft, H.M. (2005). A single CaVbeta can reconstitute both trafficking and macroscopic conductance of voltage-dependent calcium channels. J Physiol *567*, 757-769.

Dascal, N., Lotan, I., Karni, E., and Gigi, A. (1992). Calcium channel currents in Xenopus oocytes injected with rat skeletal muscle RNA. J Physiol *450*, 469-490.

Dayal, A., Schrotter, K., Pan, Y., Fohr, K., Melzer, W., and Grabner, M. (2017). The Ca(2+) influx through the mammalian skeletal muscle dihydropyridine receptor is irrelevant for muscle performance. Nat Commun *8*, 475.

DeMaria, C.D., Soong, T.W., Alseikhan, B.A., Alvania, R.S., and Yue, D.T. (2001). Calmodulin bifurcates the local Ca2+ signal that modulates P/Q-type Ca2+ channels. Nature *411*, 484-489.

di Salvo, T.G., Yang, K.C., Brittain, E., Absi, T., Maltais, S., and Hemnes, A. (2015). Right ventricular myocardial biomarkers in human heart failure. Journal of cardiac failure *21*, 398-411.

Dolphin, A.C. (2003). Beta subunits of voltage-gated calcium channels. J Bioenerg Biomembr *35*, 599-620.

Dunlap, K. (2007). Calcium channels are models of self-control. J Gen Physiol *129*, 379-383.

Edgar, R.C. (2004). MUSCLE: a multiple sequence alignment method with reduced time and space complexity. BMC Bioinformatics *5*, 113.

Erickson, M.G., Alseikhan, B.A., Peterson, B.Z., and Yue, D.T. (2001). Preassociation of calmodulin with voltage-gated Ca(2+) channels revealed by FRET in single living cells. Neuron *31*, 973-985.

Fang, K., and Colecraft, H.M. (2011). Mechanism of auxiliary beta-subunit-mediated membrane targeting of L-type (Ca(V)1.2) channels. J Physiol *589*, 4437-4455.

Findeisen, F., and Minor, D.L., Jr. (2010). Structural basis for the differential effects of CaBP1 and calmodulin on Ca(V)1.2 calcium-dependent inactivation. Structure *18*, 1617-1631.

Flucher, B.E., Kasielke, N., and Grabner, M. (2000). The triad targeting signal of the skeletal muscle calcium channel is localized in the COOH terminus of the alpha(1S) subunit. J Cell Biol *151*, 467-478.

Flynn, R., and Altier, C. (2013). A macromolecular trafficking complex composed of beta(2)-adrenergic receptors, A-Kinase Anchoring Proteins and L-type calcium channels. J Recept Signal Transduct Res *33*, 172-176.

Franzini-Armstrong, C., and Jorgensen, A.O. (1994). Structure and development of E-C coupling units in skeletal muscle. Annual review of physiology *56*, 509-534.

Freise, D., Held, B., Wissenbach, U., Pfeifer, A., Trost, C., Himmerkus, N., Schweig, U., Freichel, M., Biel, M., Hofmann, F., *et al.* (2000). Absence of the gamma subunit of the skeletal muscle dihydropyridine receptor increases L-type Ca2+ currents and alters channel inactivation properties. J Biol Chem *275*, 14476-14481.

Gabelli, S.B., Boto, A., Kuhns, V.H., Bianchet, M.A., Farinelli, F., Aripirala, S., Yoder, J., Jakoncic, J., Tomaselli, G.F., and Amzel, L.M. (2014). Regulation of the NaV1.5 cytoplasmic domain by calmodulin. Nat Commun *5*, 5126.

Giorgi, C., Danese, A., Missiroli, S., Patergnani, S., and Pinton, P. (2018). Calcium Dynamics as a Machine for Decoding Signals. Trends in cell biology.

Golini, L., Chouabe, C., Berthier, C., Cusimano, V., Fornaro, M., Bonvallet, R., Formoso, L., Giacomello, E., Jacquemond, V., and Sorrentino, V. (2011). Junctophilin 1 and 2 proteins interact with the L-type Ca2+ channel dihydropyridine receptors (DHPRs) in skeletal muscle. J Biol Chem *286*, 43717-43725.

Grzybowski, M., Schanzer, A., Pepler, A., Heller, C., Neubauer, B.A., and Hahn, A. (2017). Novel STAC3 Mutations in the First Non-Amerindian Patient with Native American Myopathy. Neuropediatrics.

Guzman, J.N., Sanchez-Padilla, J., Chan, C.S., and Surmeier, D.J. (2009). Robust pacemaking in substantia nigra dopaminergic neurons. J Neurosci *29*, 11011-11019.

Haeseleer, F., Sokal, I., Verlinde, C.L., Erdjument-Bromage, H., Tempst, P., Pronin, A.N., Benovic, J.L., Fariss, R.N., and Palczewski, K. (2000). Five members of a novel Ca(2+)-binding protein (CABP) subfamily with similarity to calmodulin. J Biol Chem *275*, 1247-1260.

Hall, D.D., Dai, S., Tseng, P.Y., Malik, Z., Nguyen, M., Matt, L., Schnizler, K., Shephard, A., Mohapatra, D.P., Tsuruta, F.*, et al.* (2013). Competition between alpha-actinin and Ca(2)(+)-calmodulin controls surface retention of the L-type Ca(2)(+) channel Ca(V)1.2. Neuron *78*, 483-497.

Halling, D.B., Aracena-Parks, P., and Hamilton, S.L. (2006). Regulation of voltage-gated Ca2+ channels by calmodulin. Sci STKE *2006*, er1.

Halling, D.B., Georgiou, D.K., Black, D.J., Yang, G., Fallon, J.L., Quiocho, F.A., Pedersen, S.E., and Hamilton, S.L. (2009). Determinants in CaV1 channels that regulate the Ca2+ sensitivity of bound calmodulin. J Biol Chem *284*, 20041-20051.

Hanrahan, J.W., Sampson, H.M., and Thomas, D.Y. (2013). Novel pharmacological strategies to treat cystic fibrosis. Trends Pharmacol Sci *34*, 119-125.

Hardy, K., Mansfield, L., Mackay, A., Benvenuti, S., Ismail, S., Arora, P., O'Hare, M.J., and Jat, P.S. (2005). Transcriptional networks and cellular senescence in human mammary fibroblasts. Mol Biol Cell *16*, 943-953.

Horstick, E.J., Linsley, J.W., Dowling, J.J., Hauser, M.A., McDonald, K.K., Ashley-Koch, A., Saint-Amant, L., Satish, A., Cui, W.W., Zhou, W.*, et al.* (2013). Stac3 is a component of the excitation-contraction coupling machinery and mutated in Native American myopathy. Nat Commun *4*, 1952.

Hsieh, Y.T., Liu, N.M., Ohmori, E., Yokota, T., Kajimura, I., Akaike, T., Ohshima, T., Goda, N., and Minamisawa, S. (2014). Transcription profiles of the ductus arteriosus in Brown-Norway rats with irregular elastic fiber formation. Circ J *78*, 1224-1233.

Huang, H., Tan, B.Z., Shen, Y., Tao, J., Jiang, F., Sung, Y.Y., Ng, C.K., Raidar, M., Kohr, G., Higuchi, M*., et al.* (2012). RNA editing of the IQ domain of $Ca_V1.3$ channels modulates their Ca^{2+}-dependent inactivation. Neuron *73*, 304-316.

Huttlin, E.L., Jedrychowski, M.P., Elias, J.E., Goswami, T., Rad, R., Beausoleil, S.A., Villen, J., Haas, W., Sowa, M.E., and Gygi, S.P. (2010). A tissue-specific atlas of mouse protein phosphorylation and expression. Cell *143*, 1174-1189.

Jackman, S.L., and Regehr, W.G. (2017). The Mechanisms and Functions of Synaptic Facilitation. Neuron *94*, 447-464.

Janzen, W.P. (2014). Screening technologies for small molecule discovery: the state of the art. Chem Biol *21*, 1162-1170.

Johnson, B.D., Brousal, J.P., Peterson, B.Z., Gallombardo, P.A., Hockerman, G.H., Lai, Y., Scheuer, T., and Catterall, W.A. (1997). Modulation of the cloned skeletal muscle L-type Ca2+ channel by anchored cAMP-dependent protein kinase. J Neurosci *17*, 1243-1255.

Joiner, M.L., and Lee, A. (2015). Voltage-Gated Cav1 Channels in Disorders of Vision and Hearing. Curr Mol Pharmacol *8*, 143-148.

Jones, L.P., DeMaria, C.D., and Yue, D.T. (1999). N-type calcium channel inactivation probed by gating-current analysis. Biophys J *76*, 2530-2552.

Joshi-Mukherjee, R., Dick, I.E., Liu, T., O'Rourke, B., Yue, D.T., and Tung, L. (2013). Structural and functional plasticity in long-term cultures of adult ventricular myocytes. J Mol Cell Cardiol *65*, 76-87.

Lacinova, L. (2005). Voltage-dependent calcium channels. Gen Physiol Biophys *24 Suppl 1*, 1-78.

Lamb, G.D. (2000). Excitation-contraction coupling in skeletal muscle: comparisons with cardiac muscle. Clin Exp Pharmacol Physiol *27*, 216-224.

Lambert, R.C., Maulet, Y., Dupont, J.L., Mykita, S., Craig, P., Volsen, S., and Feltz, A. (1996). Polyethylenimine-mediated DNA transfection of peripheral and central neurons in primary culture: probing Ca2+ channel structure and function with antisense oligonucleotides. Mol Cell Neurosci *7*, 239-246.

Lee, A., Scheuer, T., and Catterall, W.A. (2000). Ca2+/calmodulin-dependent facilitation and inactivation of P/Q-type Ca2+ channels. J Neurosci *20*, 6830-6838.

Lee, A., Westenbroek, R.E., Haeseleer, F., Palczewski, K., Scheuer, T., and Catterall, W.A. (2002). Differential modulation of Ca(v)2.1 channels by calmodulin and Ca2+-binding protein 1. Nat Neurosci *5*, 210-217.

Lee, S.R., Adams, P.J., and Yue, D.T. (2015). Large Ca(2)(+)-dependent facilitation of Ca(V)2.1 channels revealed by Ca(2)(+) photo-uncaging. J Physiol *593*, 2753-2778.

Lee, S.R., Sang, L., and Yue, D.T. (2016). Uncovering Aberrant Mutant PKA Function with Flow Cytometric FRET. Cell Rep *14*, 3019-3029.

Legha, W., Gaillard, S., Gascon, E., Malapert, P., Hocine, M., Alonso, S., and Moqrich, A. (2010). stac1 and stac2 genes define discrete and distinct subsets of dorsal root ganglia neurons. Gene Expr Patterns *10*, 368-375.

Liang, H., DeMaria, C.D., Erickson, M.G., Mori, M.X., Alseikhan, B.A., and Yue, D.T. (2003). Unified mechanisms of Ca^{2+} regulation across the Ca^{2+} channel family. Neuron *39*, 951-960.

Limpitikul, W.B., Dick, I.E., Joshi-Mukherjee, R., Overgaard, M.T., George, A.L., Jr., and Yue, D.T. (2014). Calmodulin mutations associated with long QT syndrome prevent inactivation of cardiac L-type Ca(2+) currents and promote proarrhythmic behavior in ventricular myocytes. J Mol Cell Cardiol *74*, 115-124.

Limpitikul, W.B., Dick, I.E., Tester, D.J., Boczek, N.J., Limphong, P., Yang, W., Choi, M.H., Babich, J., DiSilvestre, D., Kanter, R.J.*, et al.* (2017). A Precision Medicine Approach to the Rescue of Function on Malignant Calmodulinopathic Long-QT Syndrome. Circ Res *120*, 39-48.

Linse, S., and Forsen, S. (1995). Determinants that govern high-affinity calcium binding. Advances in Second Messenger Phosphoprotein Research *30*, 89-151.

Linsley, J.W., Hsu, I.U., Groom, L., Yarotskyy, V., Lavorato, M., Horstick, E.J., Linsley, D., Wang, W., Franzini-Armstrong, C., Dirksen, R.T.*, et al.* (2017a). Congenital myopathy results from misregulation of a muscle Ca2+ channel by mutant Stac3. Proc Natl Acad Sci U S A *114*, E228-E236.

Linsley, J.W., Hsu, I.U., Wang, W., and Kuwada, J.Y. (2017b). Transport of the alpha subunit of the L-type calcium channel through the sarcoplasmic reticulum occurs prior to localization to triads and requires the beta subunit but not Stac3 in skeletal muscles. Traffic.

Liu, X., Yang, P.S., Yang, W., and Yue, D.T. (2010). Enzyme-inhibitor-like tuning of Ca^{2+} channel connectivity with calmodulin. Nature *463*, 968-972.

Maciukiewicz, M., Marshe, V.S., Tiwari, A.K., Fonseka, T.M., Freeman, N., Kennedy, J.L., Rotzinger, S., Foster, J.A., Kennedy, S.H., and Muller, D.J. (2017). Genome-wide association studies of placebo and duloxetine response in major depressive disorder. The pharmacogenomics journal.

Mahajan, A., Sato, D., Shiferaw, Y., Baher, A., Xie, L.H., Peralta, R., Olcese, R., Garfinkel, A., Qu, Z., and Weiss, J.N. (2008). Modifying L-type calcium current kinetics: consequences for cardiac excitation and arrhythmia dynamics. Biophys J *94*, 411-423.

Maier, L.S., and Bers, D.M. (2002). Calcium, calmodulin, and calcium-calmodulin kinase II: heartbeat to heartbeat and beyond. J Mol Cell Cardiol *34*, 919-939.

Marshall, C.B., Nishikawa, T., Osawa, M., Stathopulos, P.B., and Ikura, M. (2015). Calmodulin and STIM proteins: Two major calcium sensors in the cytoplasm and endoplasmic reticulum. Biochem Biophys Res Commun *460*, 5-21.

Marshall, M.R., Clark, J.P., 3rd, Westenbroek, R., Yu, F.H., Scheuer, T., and Catterall, W.A. (2011). Functional roles of a C-terminal signaling complex of CaV1 channels and A-kinase anchoring protein 15 in brain neurons. J Biol Chem *286*, 12627-12639.

Martin, G.M., Chen, P.C., Devaraneni, P., and Shyng, S.L. (2013). Pharmacological rescue of trafficking-impaired ATP-sensitive potassium channels. Front Physiol *4*, 386.

McRory, J.E., Hamid, J., Doering, C.J., Garcia, E., Parker, R., Hamming, K., Chen, L., Hildebrand, M., Beedle, A.M., Feldcamp, L.*, et al.* (2004). The CACNA1F gene encodes an L-type calcium channel with unique biophysical properties and tissue distribution. J Neurosci *24*, 1707-1718.

Mikami, A., Imoto, K., Tanabe, T., Niidome, T., Mori, Y., Takeshima, H., Narumiya, S., and Numa, S. (1989). Primary structure and functional expression of the cardiac dihydropyridine-sensitive calcium channel. Nature *340*, 230-233.

Minor, D.L., Jr., and Findeisen, F. (2010). Progress in the structural understanding of voltage-gated calcium channel (CaV) function and modulation. Channels (Austin) *4*, 459-474.

Mintz, I.M., Sabatini, B.L., and Regehr, W.G. (1995). Calcium control of transmitter release at a cerebellar synapse. Neuron *15*, 675-688.

Mitra, S., Mazumder Indra, D., Bhattacharya, N., Singh, R.K., Basu, P.S., Mondal, R.K., Roy, A., Zabarovsky, E.R., Roychoudhury, S., and Panda, C.K. (2010). RBSP3 is frequently altered in premalignant cervical lesions: clinical and prognostic significance. Genes Chromosomes Cancer *49*, 155-170.

Mizuno, N., Niitani, M., Shiba, H., Iwata, T., Hayashi, I., Kawaguchi, H., and Kurihara, H. (2011). Proteome analysis of proteins related to aggressive periodontitis combined with neutrophil chemotaxis dysfunction. J Clin Periodontol *38*, 310-317.

Mochca, J.M., Pate, P., Zhang, J.Z., and Hamilton, S.L. (2001). Interaction of carboxy-terminal of the alpha 1 subunit of the skeletal muscle DHPR with the calmodulin binding site on RyR1 (abstr.). Biophysical Journal *80*, 379a.

Moreau, A., Keller, D.I., Huang, H., Fressart, V., Schmied, C., Timour, Q., and Chahine, M. (2012). Mexiletine differentially restores the trafficking defects caused by two brugada syndrome mutations. Front Pharmacol *3*, 62.

Mori, M.X., Erickson, M.G., and Yue, D.T. (2004). Functional stoichiometry and local enrichment of calmodulin interacting with Ca2+ channels. Science *304*, 432-435.

Mori, M.X., Vander Kooi, C.W., Leahy, D.J., and Yue, D.T. (2008). Crystal structure of the Ca$_V$2 IQ domain in complex with Ca^{2+}/calmodulin: high-resolution mechanistic implications for channel regulation by Ca^{2+}. Structure *16*, 607-620.

Nakai, J., Dirksen, R.T., Nguyen, H.T., Pessah, I.N., Beam, K.G., and Allen, P.D. (1996). Enhanced dihydropyridine receptor channel activity in the presence of ryanodine receptor. Nature *380*, 72-75.

Nanou, E., Sullivan, J.M., Scheuer, T., and Catterall, W.A. (2016). Calcium sensor regulation of the CaV2.1 Ca2+ channel contributes to short-term synaptic plasticity in hippocampal neurons. Proc Natl Acad Sci U S A *113*, 1062-1067.

Nelson, B.R., Wu, F., Liu, Y., Anderson, D.M., McAnally, J., Lin, W., Cannon, S.C., Bassel-Duby, R., and Olson, E.N. (2013). Skeletal muscle-specific T-tubule protein STAC3 mediates voltage-induced Ca2+ release and contractility. Proc Natl Acad Sci U S A *110*, 11881-11886.

Obermair, G.J., Kugler, G., Baumgartner, S., Tuluc, P., Grabner, M., and Flucher, B.E. (2005). The Ca2+ channel alpha2delta-1 subunit determines Ca2+ current kinetics in skeletal muscle but not targeting of alpha1S or excitation-contraction coupling. J Biol Chem *280*, 2229-2237.

Obermair, G.J., Tuluc, P., and Flucher, B.E. (2008). Auxiliary Ca(2+) channel subunits: lessons learned from muscle. Curr Opin Pharmacol *8*, 311-318.

Ohrtman, J., Ritter, B., Polster, A., Beam, K.G., and Papadopoulos, S. (2008). Sequence differences in the IQ motifs of CaV1.1 and CaV1.2 strongly impact calmodulin binding and calcium-dependent inactivation. J Biol Chem *283*, 29301-29311.

Oliveria, S.F., Dittmer, P.J., Youn, D.H., Dell'Acqua, M.L., and Sather, W.A. (2012). Localized calcineurin confers Ca2+-dependent inactivation on neuronal L-type Ca2+ channels. J Neurosci *32*, 15328-15337.

Oz, S., Benmocha, A., Sasson, Y., Sachyani, D., Almagor, L., Lee, A., Hirsch, J.A., and Dascal, N. (2013). Competitive and non-competitive regulation of calcium-dependent inactivation in $Ca_V1.2$ L-type Ca^{2+} channels by calmodulin and Ca^{2+}-binding protein 1. J Biol Chem.

Park, C.Y., Shcheglovitov, A., and Dolmetsch, R. (2010). The CRAC channel activator STIM1 binds and inhibits L-type voltage-gated calcium channels. Science *330*, 101-105.

Perez-Reyes, E., Castellano, A., Kim, H.S., Bertrand, P., Baggstrom, E., Lacerda, A.E., Wei, X.Y., and Birnbaumer, L. (1992). Cloning and expression of a cardiac/brain beta subunit of the L- type calcium channel. JBiolChem *267*, 1792-1797.

Perez-Reyes, E., Kim, H.S., Lacerda, A.E., Horne, W., Wei, X.Y., Rampe, D., Campbell, K.P., Brown, A.M., and Birnbaumer, L. (1989). Induction of calcium currents by the expression of the alpha 1-subunit of the dihydropyridine receptor from skeletal muscle. Nature *340*, 233-236.

Perni, S., Lavorato, M., and Beam, K.G. (2017). De novo reconstitution reveals the proteins required for skeletal muscle voltage-induced Ca(2+) release. Proc Natl Acad Sci U S A *114*, 13822-13827.

Persechini, A., and Stemmer, P.M. (2002). Calmodulin is a limiting factor in the cell. Trends Cardiovasc Med *12*, 32-37.

Peterson, B.Z., DeMaria, C.D., Adelman, J.P., and Yue, D.T. (1999). Calmodulin is the Ca^{2+} sensor for Ca2+ -dependent inactivation of L- type calcium channels. Neuron *22*, 549-558.

Pitt, G.S., Zuhlke, R.D., Hudmon, A., Schulman, H., Reuter, H., and Tsien, R.W. (2001). Molecular basis of calmodulin tethering and Ca2+-dependent inactivation of L-type Ca2+ channels. J Biol Chem *276*, 30794-30802.

Polster, A., Nelson, B.R., Olson, E.N., and Beam, K.G. (2016). Stac3 has a direct role in skeletal muscle-type excitation-contraction coupling that is disrupted by a myopathy-causing mutation. Proc Natl Acad Sci U S A *113*, 10986-10991.

Polster, A., Perni, S., Bichraoui, H., and Beam, K.G. (2015). Stac adaptor proteins regulate trafficking and function of muscle and neuronal L-type Ca2+ channels. Proc Natl Acad Sci U S A *112*, 602-606.

Powell, J.A., Petherbridge, L., and Flucher, B.E. (1996). Formation of triads without the dihydropyridine receptor alpha subunits in cell lines from dysgenic skeletal muscle. J Cell Biol *134*, 375-387.

Qin, N., Olcese, R., Bransby, M., Lin, T., and Birnbaumer, L. (1999). Ca2+-induced inhibition of the cardiac Ca2+ channel depends on calmodulin. Proc Natl Acad Sci U S A *96*, 2435-2438.

Ringer, S. (1882). Concerning the Influence exerted by each of the Constituents of the Blood on the Contraction of the Ventricle. J Physiol *3*, 380-393.

Rios, E., Pizarro, G., and Stefani, E. (1992). Charge movement and the nature of signal transduction in skeletal muscle excitation-contraction coupling. Annual review of physiology *54*, 109-133.

Rodney, G.G., and Schneider, M.F. (2003). Calmodulin modulates initiation but not termination of spontaneous Ca2+ sparks in frog skeletal muscle. Biophys J *85*, 921-932.

Rzhepetskyy, Y., Lazniewska, J., Proft, J., Campiglio, M., Flucher, B.E., and Weiss, N. (2016). A Cav3.2/Stac1 molecular complex controls T-type channel expression at the plasma membrane. Channels (Austin) *10*, 346-354.

Saimi, Y., and Kung, C. (2002). Calmodulin as an ion channel subunit. Annual review of physiology *64*, 289-311.

Sang, L., Dick, I.E., and Yue, D.T. (2016). Protein kinase A modulation of CaV1.4 calcium channels. Nat Commun *7*, 12239.

Satoh, J., Nanri, Y., and Yamamura, T. (2006). Rapid identification of 14-3-3-binding proteins by protein microarray analysis. J Neurosci Methods *152*, 278-288.

Scharinger, A., Eckrich, S., Vandael, D.H., Schonig, K., Koschak, A., Hecker, D., Kaur, G., Lee, A., Sah, A., Bartsch, D.*, et al.* (2015). Cell-type-specific tuning of Cav1.3 Ca(2+)-channels by a C-terminal automodulatory domain. Frontiers in cellular neuroscience *9*, 309.

Schneider, M.F., and Chandler, W.K. (1973). Voltage dependent charge movement of skeletal muscle: a possible step in excitation-contraction coupling. Nature *242*, 244-246.

Schredelseker, J., Dayal, A., Schwerte, T., Franzini-Armstrong, C., and Grabner, M. (2009). Proper restoration of excitation-contraction coupling in the dihydropyridine receptor beta1-null zebrafish relaxed is an exclusive function of the beta1a subunit. J Biol Chem *284*, 1242-1251.

Schredelseker, J., Di Biase, V., Obermair, G.J., Felder, E.T., Flucher, B.E., Franzini-Armstrong, C., and Grabner, M. (2005). The beta 1a subunit is essential for the assembly of dihydropyridine-receptor arrays in skeletal muscle. Proc Natl Acad Sci U S A *102*, 17219-17224.

Sekine-Aizawa, Y., and Huganir, R.L. (2004). Imaging of receptor trafficking by using alpha-bungarotoxin-binding-site-tagged receptors. Proc Natl Acad Sci U S A *101*, 17114-17119.

Sencer, S., Papineni, R.V., Halling, D.B., Pate, P., Krol, J., Zhang, J.Z., and Hamilton, S.L. (2001). Coupling of RYR1 and L-type calcium channels via calmodulin binding domains. J Biol Chem *276*, 38237-38241.

Singh, A., Gebhart, M., Fritsch, R., Sinnegger-Brauns, M.J., Poggiani, C., Hoda, J.C., Engel, J., Romanin, C., Striessnig, J., and Koschak, A. (2008). Modulation of voltage- and Ca^{2+}-dependent gating of $Ca_V1.3$ L-type calcium channels by alternative splicing of a C-terminal regulatory domain. J Biol Chem *283*, 20733-20744.

Singh, A., Hamedinger, D., Hoda, J.C., Gebhart, M., Koschak, A., Romanin, C., and Striessnig, J. (2006). C-terminal modulator controls Ca^{2+}-dependent gating of $Ca_V1.4$ L-type Ca^{2+} channels. Nat Neurosci *9*, 1108-1116.

Soong, T.W., DeMaria, C.D., Alvania, R.S., Zweifel, L.S., Liang, M.C., Mittman, S., Agnew, W.S., and Yue, D.T. (2002). Systematic identification of splice variants in human P/Q-type channel alpha1(2.1) subunits: implications for current density and Ca2+-dependent inactivation. J Neurosci *22*, 10142-10152.

Stamm, D.S., Aylsworth, A.S., Stajich, J.M., Kahler, S.G., Thorne, L.B., Speer, M.C., and Powell, C.M. (2008). Native American myopathy: congenital myopathy with cleft palate, skeletal anomalies, and susceptibility to malignant hyperthermia. American journal of medical genetics Part A *146A*, 1832-1841.

Striessnig, J., Bolz, H.J., and Koschak, A. (2010). Channelopathies in Cav1.1, Cav1.3, and Cav1.4 voltage-gated L-type Ca2+ channels. Pflugers Arch *460*, 361-374.

Stroffekova, K. (2008). Ca2+/CaM-dependent inactivation of the skeletal muscle L-type Ca2+ channel (Cav1.1). Pflugers Arch *455*, 873-884.

Stroffekova, K. (2011). The IQ motif is crucial for Cav1.1 function. J Biomed Biotechnol *2011*, 504649.

Suzuki, H., Kawai, J., Taga, C., Yaoi, T., Hara, A., Hirose, K., Hayashizaki, Y., and Watanabe, S. (1996). Stac, a novel neuron-specific protein with cysteine-rich and SH3 domains. Biochem Biophys Res Commun *229*, 902-909.

Tan, B.Z., Jiang, F., Tan, M.Y., Yu, D., Huang, H., Shen, Y., and Soong, T.W. (2011). Functional characterization of alternative splicing in the C terminus of L-type CaV1.3 channels. J Biol Chem *286*, 42725-42735.

Tan, G.M., Yu, D., Wang, J., and Soong, T.W. (2012). Alternative splicing at C terminus of Ca(V)1.4 calcium channel modulates calcium-dependent inactivation, activation potential, and current density. J Biol Chem *287*, 832-847.

Tanabe, T., Beam, K.G., Adams, B.A., Niidome, T., and Numa, S. (1990a). Regions of the skeletal muscle dihydropyridine receptor critical for excitation-contraction coupling. Nature *346*, 567-569.

Tanabe, T., Mikami, A., Numa, S., and Beam, K.G. (1990b). Cardiac-type excitation-contraction coupling in dysgenic skeletal muscle injected with cardiac dihydropyridine receptor cDNA. Nature *344*, 451-453.

Tanabe, T., Takeshima, H., Mikami, A., Flockerzi, V., Takahashi, H., Kangawa, K., Kojima, M., Matsuo, H., Hirose, T., and Numa, S. (1987). Primary structure of the receptor for calcium channel blockers from skeletal muscle. Nature *328*, 313-318.

Tay, L.H., Dick, I.E., Yang, W., Mank, M., Griesbeck, O., and Yue, D.T. (2012). Nanodomain Ca(2)(+) of Ca(2)(+) channels detected by a tethered genetically encoded Ca(2)(+) sensor. Nat Commun *3*, 778.

Telegrafi, A., Webb, B.D., Robbins, S.M., Speck-Martins, C.E., FitzPatrick, D., Fleming, L., Redett, R., Dufke, A., Houge, G., van Harssel, J.J.T.*, et al.* (2017). Identification of STAC3 variants in non-Native American families with overlapping features of Carey-Fineman-Ziter syndrome and Moebius syndrome. American journal of medical genetics Part A *173*, 2763-2771.

Thomas, J.R., and Lee, A. (2016). Measuring Ca2+-Dependent Modulation of Voltage-Gated Ca2+ Channels in HEK-293T Cells. Cold Spring Harb Protoc *2016*, pdb prot087213.

Tomlinson, W.J., Stea, A., Bourinet, E., Charnet, P., Nargeot, J., and Snutch, T.P. (1993). Functional properties of a neuronal class C L-type calcium channel. Neuropharmacology *32*, 1117-1126.

Trimmer, J.S., Cooperman, S.S., Agnew, W.S., and Mandel, G. (1990). Regulation of muscle sodium channel transcripts during development and in response to denervation. Dev Biol *142*, 360-367.

Troiani, S., Lupi, R., Perego, R., Depaolini, S.R., Thieffine, S., Bosotti, R., and Rusconi, L. (2011). Identification of candidate substrates for poly(ADP-ribose) polymerase-2 (PARP2) in the absence of DNA damage using high-density protein microarrays. FEBS J *278*, 3676-3687.

Tseng, P.Y., Henderson, P.B., Hergarden, A.C., Patriarchi, T., Coleman, A.M., Lillya, M.W., Montagut-Bordas, C., Lee, B., Hell, J.W., and Horne, M.C. (2017). alpha-Actinin Promotes Surface Localization and Current Density of the Ca2+ Channel CaV1.2 by Binding to the IQ Region of the alpha1 Subunit. Biochemistry *56*, 3669-3681.

Tuluc, P., and Flucher, B.E. (2011). Divergent biophysical properties, gating mechanisms, and possible functions of the two skeletal muscle Ca(V)1.1 calcium channel splice variants. J Muscle Res Cell Motil *32*, 249-256.

Tuluc, P., Molenda, N., Schlick, B., Obermair, G.J., Flucher, B.E., and Jurkat-Rott, K. (2009). A CaV1.1 Ca2+ channel splice variant with high conductance and voltage-sensitivity alters EC coupling in developing skeletal muscle. Biophys J *96*, 35-44.

Valdivia, C.R., Tester, D.J., Rok, B.A., Porter, C.B., Munger, T.M., Jahangir, A., Makielski, J.C., and Ackerman, M.J. (2004). A trafficking defective, Brugada syndrome-causing SCN5A mutation rescued by drugs. Cardiovasc Res *62*, 53-62.

Vandael, D.H., Marcantoni, A., Mahapatra, S., Caro, A., Ruth, P., Zuccotti, A., Knipper, M., and Carbone, E. (2010). Ca(v)1.3 and BK channels for timing and regulating cell firing. Molecular neurobiology *42*, 185-198.

Venetucci, L., Denegri, M., Napolitano, C., and Priori, S.G. (2012). Inherited calcium channelopathies in the pathophysiology of arrhythmias. Nature reviews Cardiology *9*, 561-575.

Wang, C., Chung, B.C., Yan, H., Lee, S.Y., and Pitt, G.S. (2012). Crystal Structure of the Ternary Complex of a NaV C-Terminal Domain, a Fibroblast Growth Factor Homologous Factor, and Calmodulin. Structure *20*, 1167-1176.

Wang, C., Chung, B.C., Yan, H., Wang, H.G., Lee, S.Y., and Pitt, G.S. (2014). Structural analyses of Ca(2)(+)/CaM interaction with NaV channel C-termini reveal mechanisms of calcium-dependent regulation. Nat Commun *5*, 4896.

Wang, C., Wang, C., Hoch, E.G., and Pitt, G.S. (2011). Identification of novel interaction sites that determine specificity between fibroblast growth factor homologous factors and voltage-gated sodium channels. J Biol Chem *286*, 24253-24263.

Wang, H.G., George, M.S., Kim, J., Wang, C., and Pitt, G.S. (2007). Ca2+/calmodulin regulates trafficking of Ca(V)1.2 Ca2+ channels in cultured hippocampal neurons. J Neurosci *27*, 9086-9093.

Wang, Y., Deng, X., Mancarella, S., Hendron, E., Eguchi, S., Soboloff, J., Tang, X.D., and Gill, D.L. (2010). The calcium store sensor, STIM1, reciprocally controls Orai and CaV1.2 channels. Science *330*, 105-109.

Wei, X.Y., Perez-Reyes, E., Lacerda, A.E., Schuster, G., Brown, A.M., and Birnbaumer, L. (1991). Heterologous regulation of the cardiac Ca2+ channel alpha 1 subunit by skeletal muscle beta and gamma subunits. Implications for the structure of cardiac L-type Ca2+ channels. JBiolChem *266*, 21943-21947.

Weiss, N., and Zamponi, G.W. (2017). Trafficking of neuronal calcium channels. Neuronal Signaling.

Wilhelm, M., Schlegl, J., Hahne, H., Gholami, A.M., Lieberenz, M., Savitski, M.M., Ziegler, E., Butzmann, L., Gessulat, S., Marx, H*., et al.* (2014). Mass-spectrometry-based draft of the human proteome. Nature *509*, 582-587.

Wong King Yuen, S.M., Campiglio, M., Tung, C.C., Flucher, B.E., and Van Petegem, F. (2017). Structural insights into binding of STAC proteins to voltage-gated calcium channels. Proc Natl Acad Sci U S A *114*, E9520-E9528.

Wu, J., Yan, Z., Li, Z., Qian, X., Lu, S., Dong, M., Zhou, Q., and Yan, N. (2016). Structure of the voltage-gated calcium channel Ca(v)1.1 at 3.6 A resolution. Nature *537*, 191-196.

Xiong, L.W., Newman, R.A., Rodney, G.G., Thomas, O., Zhang, J.Z., Persechini, A., Shea, M.A., and Hamilton, S.L. (2002). Lobe-dependent regulation of ryanodine receptor type 1 by calmodulin. J Biol Chem *277*, 40862-40870.

Xu, W., and Lipscombe, D. (2001). Neuronal Ca(V)1.3alpha(1) L-type channels activate at relatively hyperpolarized membrane potentials and are incompletely inhibited by dihydropyridines. J Neurosci *21*, 5944-5951.

Yang, P.S., Alseikhan, B.A., Hiel, H., Grant, L., Mori, M.X., Yang, W., Fuchs, P.A., and Yue, D.T. (2006). Switching of Ca^{2+}-dependent inactivation of Cav1.3 channels by calcium binding proteins of auditory hair cells. J Neurosci *26*, 10677-10689.

Yang, P.S., Ben-Johny, M., and Yue, D.T. (2014a). Allostery in Ca^{2+} channel modulation by calcium binding proteins. Nature Chemical Biology *in press*.

Yang, P.S., Johny, M.B., and Yue, D.T. (2014b). Allostery in Ca(2)(+) channel modulation by calcium-binding proteins. Nat Chem Biol *10*, 231-238.

Yang, T., Xu, X., Kernan, T., Wu, V., and Colecraft, H.M. (2010). Rem, a member of the RGK GTPases, inhibits recombinant CaV1.2 channels using multiple mechanisms that require distinct conformations of the GTPase. J Physiol *588*, 1665-1681.

Zaharieva, I.T., Colombo, I., Sframeli, M., Sigurosson, J.H., Feng, L., Phadke, R., Sewry, C.A., Morgan, J.E., and Muntoni, F. (2014). G.P.261: Whole exome sequencing in patients with congenital myopathies. Nueuromuscular Disorders *24*, 895.

Zamponi, G.W. (2016). Targeting voltage-gated calcium channels in neurological and psychiatric diseases. Nat Rev Drug Discov *15*, 19-34.

Zamponi, G.W., Striessnig, J., Koschak, A., and Dolphin, A.C. (2015). The Physiology, Pathology, and Pharmacology of Voltage-Gated Calcium Channels and Their Future Therapeutic Potential. Pharmacological reviews *67*, 821-870.

Zhou, H., Yu, K., McCoy, K.L., and Lee, A. (2005). Molecular mechanism for divergent regulation of Cav1.2 Ca2+ channels by calmodulin and Ca2+-binding protein-1. J Biol Chem *280*, 29612-29619.

Zimmer, T., and Surber, R. (2008). SCN5A channelopathies--an update on mutations and mechanisms. Progress in biophysics and molecular biology *98*, 120-136.

Zuhlke, R.D., Pitt, G.S., Deisseroth, K., Tsien, R.W., and Reuter, H. (1999). Calmodulin supports both inactivation and facilitation of L-type calcium channels. Nature *399*, 159-162.

CURRICULUM VITAE

The Johns Hopkins University School of Medicine

Jacqueline Niu March 9th, 2018

Educational History

Ph.D. expected	2018	Program in Biomedical Engineering Mentors: Takanari Inoue, PhD; Manu Ben-Johny, PhD; David T. Yue, PhD MD	Johns Hopkins School of Medicine
B.S.	2012	Biomedical Engineering	University of Virginia

Other Professional Experience

Research rotation	2012-2013	Lab of Alexander S. Popel	Johns Hopkins School of Medicine
VGEM	2011-2012	UVA iGEM Team	University of Virginia
Summer research	2010-2012	Lab of Richard J. Price	University of Virginia

Scholarships, fellowships, or other external funding

NSF GRFP	2013-2018	$34,000 + $10,400; Stipend and research support

Academic and other honors

2014	Head of Family of the Month	Thread (previously known as Incentive Mentoring Program)
2012	Benjamin Zweifach Graduate Student Travel Award	
2011	Silver Medal	America regional iGEM competition
2008-2012	Dean's List	University of Virginia
2010	Intermediate Honors	University of Virginia

Publications

Niu, J., Dick, I. E., Yang, W., Yue D. T., Tomaselli, G. F., Inoue, T., Ben-Johny, M. Allosteric regulators selectively tune the gain of CaM-feedback to CaV and NaV channels. (under review)

Niu, J., Yang, W., Yue D. T., Inoue, T., Ben-Johny, M. Duplex signaling by CaM and Stac3 enhances CaV 1.1 function and unveils pharmacological insights for congenital myopathy. (under review)

Niu, J., Johny, M. B., Dick, I. E., Inoue, T. (2016). Following optogenetic dimerizers and quantitative prospects. Biophysical Journal, 111, 1132-1140.

Dick, I. E. et al. (2016). A rendezvous with the queen of ion channels: Three decades of ion channel research by David T. Yue and his Calcium Signals Laboratory. Channels, 10, 20-32.

Ben-Johny, M. et al. (2015). Towards a Unified Theory of Calmodulin Regulation (Calmodulation) of Voltage-Gated Calcium and Sodium Channels. Curr. Mol. Pharmacol. 8, 188-205.

Ben Johny, M., Yang, P.S., **Niu, J.**, Yang, W., Joshi-Mukhurjee, R., Yue, D.T. (2014). Conservation of Ca2+/calmodulin regulation across Na and Ca2+ channels. Cell, 157, 1657-1670.

Meisner, J. K., **Niu, J.**, Sumer, S., Price, R. J. (2013). Trans-illuminated laser speckle imaging of collateral artery blood flow in ischemic mouse hindlimb. Journal of biomedical optics, 18, 096011.

Posters, abstracts, etc.

Niu, J., Ben-Johny, M., Yue, D. T., Inoue, T. Calmodulin and Stac3 enhance functional expression of CaV1.1 Biophysical Journal (2017).

Niu, J., Ben-Johny, M., Adams, P. J., Yue, D. T. Calmodulation of voltage-gated calcium channels by blue light. Biophysical Journal (2015).

Ben Johny, M., Yang, P.S., **Niu, J.**, Yang, W., Joshi-Mukhurjee, R., and Yue, D.T. Conservation of calmodulin regulation across voltage-gated sodium and calcium channels. Biophysical Journal (2014).

Niu, J., Sumer, S., Meisner, J. K., Price, R. J. Collateral artery blood flow measurements made in the mouse ischemic hindlimb model using deep laser speckle imaging. The FASEB Journal (2012).

Meisner, J. K., Sumer, S., **Niu, J.**, Price, R. J. Accelerated arteriogenesis In collateral arterial segments exposed to flow reversal after femoral arterial ligation. The FASEB Journal (2012).

Service and leadership

2016	Scientific Computing in BME using Python and MATLAB – graduate teaching assistant – held weekly office hours, and graded homework and exams
2015	Systems Bioengineering I – graduate teaching assistant – led two weekly recitations and held weekly office hours on ion channels and muscle physiology
2012-2015	Head of Family at Thread – tutored two high school students in inner city Baltimore
2013	Secretary of BME EDGE – assisted with establishing the center for externships